# Bulletin of Materials Science

Volume 21, No. 3, June 1998

## CONTENTS

---

Cover: Microstructure of unhardened zone of oil-hardened nonshrinking steel. For details, see p. 248.

---

Material Synthesis

Preparation of aluminosilicate precursor by mechanochemical method from gibbsite-fumed silica mixtures
**J Temuujin, T S Jadambaa, K Okada and K J D Mackenzie** 185

Synthesis, characterization and application of a derivatized acid salt of tetravalent metal: *o*-chlorophenol anchored onto zirconium tungstate **Beena Pandit and Uma Chudasama** 189

Mechanism and control of formation of porous silicon on *p*-type Si
**H Saha, S K Dutta, S M Hossain, S Chakraborty and A Saha** 195

Thermal Properties

Phase diagram and thermochemical properties of organic eutectic in a monotectic system
**U S Rai and R N Rai** 203

Thermally stimulated current and electrical conduction in metal (1)–ethyl cellulose–metal (1)/(2) systems
**P K Khare, Ashish Verma and Sunil K Paliwal** 207

Electrical Properties

Electrical properties of zirconium diselenide single crystals grown by iodine transport method
**S G Patel, M K Agarwal, N M Batra and D Lakshminarayana** 213

Dielectric properties and electrical conduction in yttrium iron garnet (YIG) **Lalitha Sirdeshmukh, K Krishna Kumar, S Bal Laxman, A Rama Krishna and G Sathaiah** 219

Optical Materials

Optical and mechanical characteristics of zinc sulphide–thorium fluoride mixed composition thin films for use in the near infrared region (1–10 μm) **A Basu, B S Verma, T K Bhattacharyya, M Kar and R Bhattacharyya** 227

Magnetic Materials

Magnetic ordering in $Mg_{1+x}Mn_xFe_{2-2x}O_4$ system **N N Jani, B S Trivedi, H H Joshi, G K Bichile and R G Kulkarni** 233

Mechanical Properties

Fracture toughness correlation with microstructure and other mechanical properties in near-eutectoid steel
**K V Sudhakar and G S Murty** 241

Surfaces of Materials

Surface hardening of oil-hardened nonshrinking steel using ruby laser
**A Ramalingam, B J Kalaiselvi, S Sridharan, P K Palanisamy and V Masilamani** 247

# Bulletin of
# Materials Science

Volume 21 Number 3 June 1998

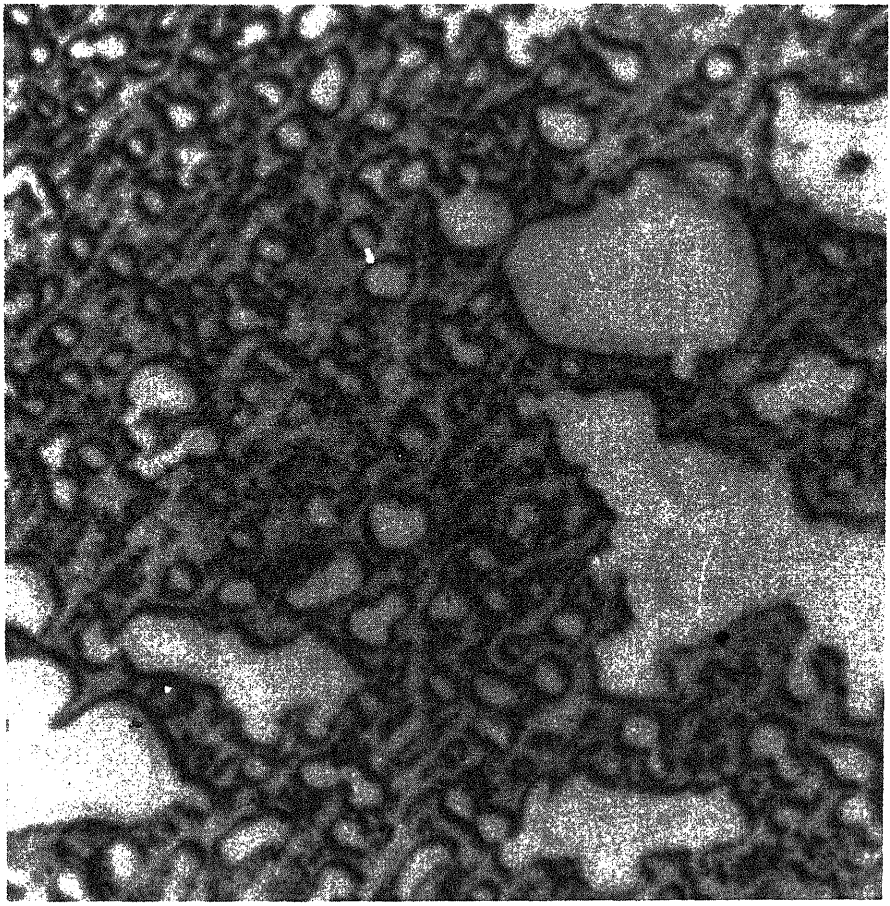

*Published by*
**INDIAN ACADEMY OF SCIENCES**
*in collaboration with*
MATERIALS RESEARCH SOCIETY OF INDIA and
INDIAN NATIONAL SCIENCE ACADEMY

**Instrumentation**

An experimental setup for dynamic measurement of magnetoelectric effect **M Mahesh Kumar, A Srinivas, S V Suryanarayana, G S Kumar and T Bhimasankaram**

Density of micro-quantity liquids by the method of rise of drops in immiscible liquids **G J Srinivasan, G Thirunavukkarasu and P Satyanarayana**

Indexed in
- CURRENT CONTENTS
- CHEMICAL ABSTRACTS
- METALS ABSTRACTS
- INSPEC/PHYSICS ABSTRACTS
- FIZ KARLSRUHE
- CAMBRIDGE SCIENTIFIC ABSTRACTS

ISSN 0250-

Edited and published by N Mukunda for the Indian Academy of Sciences, Bangalore 560 080.
Typeset at R D Typesetters, Bangalore (Ph: 3405672) and printed by Lotus Printers, Bangalore (Ph: 3380167).

# Preparation of aluminosilicate precursor by mechanochemical method from gibbsite-fumed silica mixtures

J TEMUUJIN*, T S JADAMBAA†, K OKADA†† and K J D MACKENZIE†††
Institute of Chemistry and Chemical Technology, Mongolian Academy of Sciences, Ulaanbaatar 51, Mongolia
†Department of Chemical Technology, Mongolian Technical University, Ulaanbaatar 46, Mongolia
††Department of Inorganic Materials, Tokyo Institute of Technology, 2-12-1 O-okayama, Meguro-ku, Tokyo 152, Japan
†††New Zealand Institute for Industrial Research and Development, P.O. Box 31-310, Lower Hutt, New Zealand

MS received 28 January 1998

**Abstract. Aluminosilicate (mullite) precursor was prepared by mechanochemical treatment of gibbsite and fumed silica mixtures. The effect of grinding on its structure and thermal behaviour was examined by $^{27}$Al and $^{29}$Si MAS NMR, XRD, DTA–TG and FTIR. Thermal treatment of this precursor led to the crystallization of mullite at about 1200°C via a spinel-phase. $^{27}$Al and $^{29}$Si MAS NMR spectroscopies show lowering of mullitization temperature, which is associated with increased homogeneity of the precursor. Mechanochemical treatment of gibbsite and fumed silica mixtures resulted in the formation of a more homogeneous aluminosilicate precursor.**

**Keywords. Mullite; mechanochemistry; NMR.**

## 1. Introduction

The homogeneity of aluminosilicate (mullite) precursors depends largely on the processing method, i.e. how to mix, precipitate, hydrolyse or react $SiO_2$ and $Al_2O_3$ components (Schneider *et al* 1994). As part of work to evaluate the mechanochemical effect for the preparation of aluminosilicate precursors, various alumina–silica mixtures have been milled in a planetary pot mill (Temuujin *et al* 1997a–d). The homogeneity of these mixtures depends on water and hydroxyl content of the starting materials (Temuujin *et al* 1997b,c) and it was noted that the hydroxyls must be associated with the alumina starting material but not necessarily with the initial silica.

Silica gel, fused silica and silicic acid were used as silica source, and found that the homogeneity of resulting precursors depended on the siliceous starting materials. In the present work, aluminosilicate (mullite) precursor was synthesized by mechanochemical activation of gibbsite and fumed silica mixtures and the product compared with those previously obtained under identical conditions using silica gel, fused silica and silicic acid (Temuujin *et al* 1997b,d).

## 2. Experimental

The starting materials used in the investigation were gibbsite (Showa Denko Co. Ltd., Japan) and fumed silica (Aerosil 200, Aerosil Co. Ltd). The composition of the mixture was 75 ± 1 wt% alumina/25 ± 1 wt% silica, ground for 20 h in a planetary pot mill (La-PO.1, ITOH Co. Ltd) at room temperature. The rotation speed of planetary pot mill was 400 rpm and milling media and pot were made from silicon nitride. The weight ratio of milling media to powder was 20 : 1.

After grinding, samples were characterized by XRD (RIGAKU, Geigerflex with monochromatized CuK$\alpha$ radiation), FTIR (SHIMADZU, FTIR 8200 PC with the samples suspended in KBr discs) and DTA–TG (RIGAKU, Thermoplus TG 8120). $^{29}$Si and $^{27}$Al MAS-NMR spectra were obtained at 11·7 T using a Varian Unity 500 spectrometer and Doty probe spun at 10–12 kHz. The $^{29}$Si spectra were acquired using a 90° pulse of 6 µs and recycle time of 100 s, and were referenced to tetramethylsilane (TMS). The $^{27}$Al spectra were acquired using a 15° pulse of 1 µs and a recycle time of 1 s and were referenced to $Al(H_2O)_6^{3+}$.

## 3. Results and discussion

The DTA–TG measurements (not shown here), indicate that the intensity of the endothermic effect at 260°C due to dehydration of gibbsite decreases with grinding but does not disappear. A new exothermic peak which appears at about 960°C is related to the homogeneity of the resulting precursor, as previously described by

---

*Author for correspondence

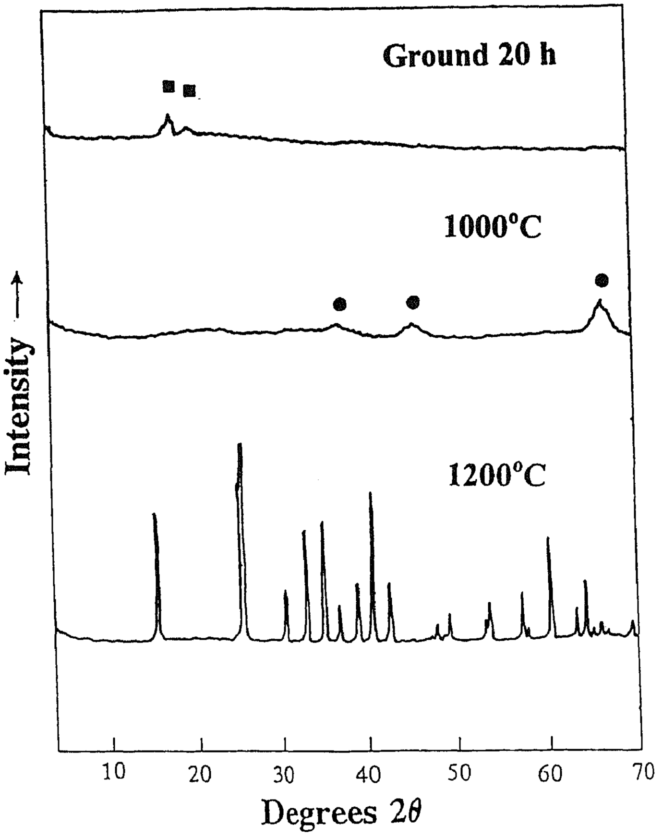

**Figure 1.** XRD pattern of ground mixtures and after calcining at different temperatures (■, gibbsite; ●, spinel phase; unmarked peaks, mullite).

Temuujin *et al* (1997a,b). Figure 1 shows XRD patterns of the mixtures ground for 20 h and calcined at different temperatures. In contrast with silica gel and silicic acid, the XRD intensities of the gibbsite reflections decrease with grinding and almost disappear. In the X-ray powder diffraction patterns of the samples, calcined for 2 h at 1000°C, broad reflections of $\gamma$-Al$_2$O$_3$ or spinel-phase are observed. In our previous experiments we have shown that the DTA exothermic effect at about 980°C is related to the formation of spinel-phase into which is incorporated a small amount of silica from the aluminosilicate precursor (Temuujin *et al* 1997c). In the present precursor, mullite crystallizes at 1200°C without any other minor phases and its XRD intensity increases with subsequent heat treatments. The thermal behaviour of this precursor can be correlated with the structural changes introduced by grinding.

Grinding for 20 h causes several OH stretching vibrations at 3500 cm$^{-1}$ to merge into a single broad band and OH bending vibrations around 1020 cm$^{-1}$ to disappear. Also the absorption band at 1100 cm$^{-1}$ due to the tetrahedral Si–O vibration shifts to 1020 cm$^{-1}$. This shift to lower wave number can be explained by incorporation of Al$^{3+}$ into the Si$^{4+}$ sites (Temuujin *et al* 1997a,b; Okada and Otsuka 1986). The absorption band at 800 cm$^{-1}$, arising from three-dimensionally bonded SiO$_4$ (Liao and Senna 1993), also disappears on grinding.

Figure 2 shows the $^{27}$Al and $^{29}$Si MAS NMR spectra of gibbsite, fumed silica and the ground mixture.

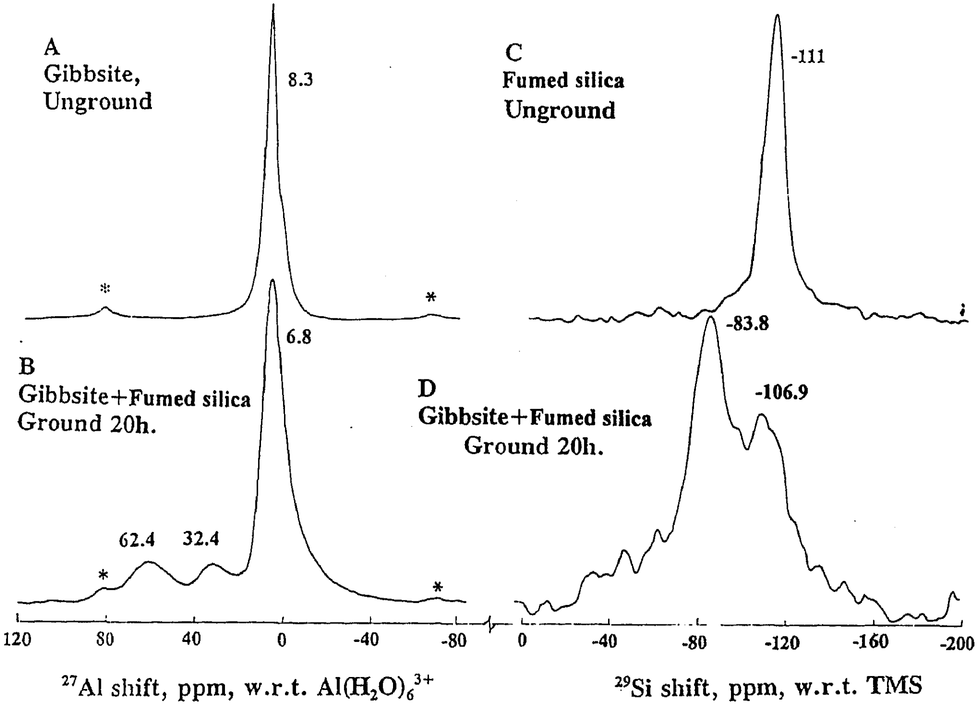

**Figure 2.** 11·7 T $^{29}$Si and $^{27}$Al MAS–NMR spectra of starting materials and ground samples. Asterisks denote spinning side bands.

Unground gibbsite shows the octahedral $^{27}$Al resonance at 8·3 ppm, and unground fumed silica shows $^{29}$Si resonance in the $SiO_2$ region (– 111 ppm). In contrast with silica gel and silicic acid (Temuujin *et al* 1997a,d), fumed silica almost contains no hydrated Si–O units. Grinding of mixture introduces new $^{27}$Al resonances at 62·4 and about 32·4 ppm. The latter has been ascribed to pentacoordinated Al, or to distorted 4-coordinated Al associated with tricluster units which occur in mullite (Schmucker and Schneider 1996). The $^{29}$Si spectrum of ground mixture shows the appearance of a new strong peak at about – 83 ppm which reflects the presence of a significant proportion of the Si associated with aluminosilicate units (Temuujin *et al* 1997c). The $^{27}$Al and $^{29}$Si MAS NMR spectra of the ground mixture suggest that grinding for 20 h produces homogeneous structures in which the Si and Al are intimately combined, consistent with the crystallization behaviour of this precursor.

These experiments suggest that fumed silica is more reactive to mechanochemical activation than silica gel, silicic acid and fused silica. Fumed silica, like fused silica, contains few hydroxyl groups, but the homogeneity of fumed silica + gibbsite mixtures as reflected by NMR measurements is much greater than fused silica + gibbsite mixtures (Temuujin *et al* 1997b). The present results suggest that the mechanochemical formation of amorphous aluminosilicate does not require the silica component to contain large concentration of hydroxyl groups. A more important factor may be the fineness and dispersion of the starting siliceous component (BET specific surface area of fumed silica is 200 $m^2/g$ and fused silica is 4·3 $m^2/g$), which can beneficially influence the preparation of aluminosilicate precursors by the mechanochemical method.

## 4. Conclusions

Mullite precursors were prepared by a mechanochemical method using gibbsite and fumed silica as starting materials. Judging by the homogeneity of the precursors, fumed silica is more reactive than silica gel, silicic acid and fused silica. These differences are attributed to the high degree of dispersion of the fumed silica (particle size less than several tens of nanometers), which is more completely adsorbed on the active sites of ground gibbsite, facilitating the formation of amorphous aluminosilicate.

## Acknowledgements

The authors wish to thank A Shimai, Tokyo Institute of Technology, for performing FTIR measurements. One of the authors (JT) would like to thank UNESCO/MONBUSHO for the award of a research fellowship.

## References

Liao J and Senna M 1993 *Solid State Ionics* **66** 313
Okada K and Otsuka N 1986 *J. Am. Ceram. Soc.* **69** 652
Schneider H, Okada K and Pask J 1994 *Mullite and mullite ceramics* (Chichester: Wiley) p. 105
Schmucker M and Schneider H 1996 *Ber. Bunsenges Phys. Chem.* **100** 1550
Temuujin J, Okada K and MacKenzie K 1997a *J. Mater. Res.* (in press)
Temuujin J, Okada K and MacKenzie K 1997b *J. Eur. Ceram. Soc.* (submitted)
Temuujin J, Okada K and MacKenzie K 1997c *Ceram. Int.* (in press)
Temuujin J, Okada K and MacKenzie K 1997d *Mater. Lett.* (submitted)

Bull. Mater. Sci., Vol. 21, No. 3, June 1998, pp. 189–193. © Indian Academy of Sciences.

# Synthesis, characterization and application of a derivatized acid salt of tetravalent metal: *o*-chlorophenol anchored onto zirconium tungstate

**BEENA PANDIT and UMA CHUDASAMA***
Department of Applied Chemistry, M.S. University of Baroda, Vadodara 390 001, India

MS received 2 February 1998; revised 23 April 1998

**Abstract.** **Tetravalent metal acid (TMA) salt zirconium tungstate (ZW) has been synthesized, followed by its derivatization using ortho chlorophenol (ZWoCP). ZWoCP has been characterized for elemental analysis, spectral analysis (FTIR) and thermal analysis (TGA). Its chemical stability has been assessed in various acidic, basic and organic media. Ion exchange capacity (IEC) has been determined and distribution behaviour towards several metal ions in different electrolyte concentrations studied and a few binary separations achieved.**

**Keywords.** **Tetravalent metal acid salts; derivatized TMA salts.**

## 1. Introduction

Tetravalent metal acid salts are obtained as amorphous and crystalline materials (Clearfield and Stynes 1964). These compounds have the general formula M(IV) $(HXO_4)_2 \cdot nH_2O$, where M(IV) = Zr, Ti, Th, Ce, Sn, etc and X = P, Mo, W, Sb, As, etc. The protons of the OH group can be exchanged for several metal ions and thus these materials are termed as inorganic ion exchangers.

TMA salts can be derivatized by organic moieties bearing ionogenic groups such as –OH, –COOH, $-SO_3H$, etc which also act as ion exchangers. These compounds are known as inorgano–organic ion exchangers or derivatized tetravalent metal acid (DTMA) salts (Alberti *et al* 1978, 1980, 1982; Kornyei 1982).

Interest in DTMA salts stems from the fact that the inorganic backbone provides a stable and relatively inert anchor for the organic moiety. DTMA salts have the added advantage of both their counterparts in terms of thermal and chemical stability and ion exchange capacity. Derivatization of the inorganic ion exchangers by organic molecules depends on the nature of the inorganic matrix.

In layered materials the organic molecules are incorporated within the layers (Maya and Danis 1980; Costantino *et al* 1986), whereas in non layered materials the organic molecules get either anchored, sorbed on the surface or get encapsulated within the pores of the matrix. Preparation of organic derivatives of inorganic TMA salts has been studied (Alberti *et al* 1978, 1980, 1982; Kornyei 1982) by intercalation of polar organic molecules such as alcohols, glycols, acetone, urea and its derivatives or molecules of biopharmaceutical interest such as amino acids, heterocyclic bases, etc (Behrendt *et al* 1976; Costantino 1979; Maya and Danis 1980; Szirtes *et al* 1988) within the layers of crystalline $\alpha$-zirconium phosphate ($\alpha$ZrP).

Three oxygens of each phosphate group are bonded to three different zirconium atoms while the fourth oxygen bears the exchangeable proton that can be easily replaced by other cations. Compounds in which the ≡P–R or ≡P–OR groups (R = organic alkyl/aryl radicals such as $H_2O_3P \cdot CH_2OH/H_2O_3P \cdot C_6H_5$) are reported (Alberti *et al* 1985: Alberti and Costantino 1991).

Apart from the fundamental aspects, there is an increasing interest in the potential applications of inorgano–organic ion exchangers. According to the nature of R group, different applications in the field of chromatographic separation (Alberti *et al* 1989), catalysis (Alberti *et al* 1993a), photochemistry (Vermeulen and Thompson 1992), protonic conduction (Casciola *et al* 1990; Alberti *et al* 1993b; Alberti and Casciola 1997) and radiochemical studies (Tomita Isao 1996), are possible. Organic derivatives are used as supports in gas chromatography, thin layer chromatography and molecular sieves (Alberti *et al* 1993a). The loading potential of the inorganic backbone is as high as two alkyl groups per zirconium atom, which is a distinct advantage over commercial reverse phase chromatography supports. Besides, inorgano–organic materials are known to have a large selectivity for mono and multivalent cations (Costantino 1979).

Organic derivatives of layered $\alpha$ZrP can be termed as intercalation compounds or lamellar compounds. In case of $\gamma$ZrP however, derivatization takes place through a topotactic reaction which consists of the substitution of $O_3POH$ tetrahedra in a preformed layered phosphate by $O_3PR$ tetrahedra, whilst retaining the original layered structure (Alberti 1990; Alberti *et al* 1992, 1993b). Using this method, substitution of the OH by R groups (Alberti *et al* 1994) takes place as follows

---

*Author for correspondence

$$\mathrm{M(IV)\,(HPO_4)_2 + 2RPO_3H_2 \rightleftharpoons M(IV)\,(RPO_3)_2 + 2H_3PO_4}.$$

In the present endeavour, an attempt has been made to synthesize an inorgano–organic ion exchanger ZWoCP by treating an inorganic ion exchanger zirconium tungstate (ZW) reported by us earlier (Kale *et al* 1994) with an organic moiety *ortho*-chlorophenol (*o*CP).

ZWoCP has been characterized for elemental analysis, spectral analysis (FTIR) and thermal analysis (TGA). Ion exchange capacity (IEC) has been determined and the effect of heating on IEC studied. Distribution behaviour for several metal ions has been studied in various electrolyte concentrations, on the basis of which metal ion separations have been carried out. Binary separation of Co(II) from Cu(II), Zn(II) and Pb(II) has been achieved.

## 2. Experimental

### 2.1 *Preparation of zirconium tungstate (ZW)*

ZW has been prepared by adding an aqueous solution of sodium tungstate to an aqueous solution of zirconium oxychloride till complete precipitation. The pH was adjusted to ~ 8 using very dilute ammonia followed by washing with conductivity water till the washings were chloride free. The precipitates were dried at ~ 40°C and sieved to the desired particle size (30–60 mesh). The sample was then converted to the hydrogen form by immersion in 1 M HCl, the acid being replaced intermittently. It was then washed repeatedly with conductivity water till free of chloride ion and finally dried at 40°C.

### 2.2 *Preparation of organic derivative (ZWoCP)*

ZWoCP was prepared by heating under reflux 1 g of the acid treated ZW with 20 ml of pure distilled *o*-chlorophenol. The excess of the organic reagent was decanted. This was followed by washing the sample with alcohol and finally drying it at ~ 40°C. The amount of *o*CP anchored onto ZW was estimated as the difference between the initial and final concentration by the bromination method (Vogel 1989).

### 2.3 *Characterization*

Zirconium and tungsten in ZW and ZWoCP were estimated gravimetrically as zirconium oxide by cupferron method (Elving and Olson 1955) and as barium tungstate (Vogel 1978), respectively. Carbon and hydrogen in ZWoCP were determined using a Coleman analyser model 33. Thermograms (TGA) were recorded on a Shimadzu DT-30 thermal analyser at a heating rate of 10°C min$^{-1}$. FTIR spectra were recorded on a Perkin Elmer model 1720X equipped with Epson Hi 80 printer/plotter. Sample preparation was done using KBr as reference with 1% sample concentration.

Chemical stability of ZWoCP was checked in several mineral acids such as HCl, $HNO_3$ and $H_2SO_4$; bases such as NaOH and KOH; and organic solvents such as alcohol, acetone and diethyl ether. 500 mg each of ZWoCP was taken in 50 ml of different solvents and kept for 24 h and the changes in colour, nature and weight of the sample were noted.

The ion exchange capacity (IEC) was determined by the column method (Nabi and Rao 1981) and the effect of heating on IEC was studied by heating the exchangers at various temperatures in the range 100°–500°C for 2 h each in a muffle furnace.

### 2.4 *Distribution studies*

Ion exchange behaviour for several metal ions such as transition metals ($Zn^{2+}$, $Cu^{2+}$, $Ni^{2+}$, $Mn^{2+}$, $Co^{2+}$); heavy metals ($Pb^{2+}$, $Bi^{3+}$, $Hg^{2+}$) and rare earths ($La^{3+}$, $Ce^{4+}$, $Th^{4+}$) was studied and their distribution coefficient ($K_d$) determined. $K_d$ is defined as

$$K_d = \frac{I-F}{F} \times \frac{V}{W}\ (\mathrm{ml\ g^{-1}}),$$

where, $I$ is the initial amount of the metal ion in solution, $F$ the final amount of the metal ion in solution, $V$ the volume of the metal ion solution taken for analysis (ml) and $W$ the weight of the exchanger taken for analysis (g).

The ion exchanger (0·1 g) was equilibrated with a 0·001 M (20 ml) solution of the metal ion at room temperature for 24 h with intermittent shaking. The uptake of the metal ion was determined as a difference in the initial and the residual concentrations of the metal ion using EDTA as a titrant. Distribution studies were also carried out for all the above mentioned metal ions in different electrolyte media such as 0·001 M, 0·1 M, 0·4 M $HNO_3$ and 0·05 M, 0·5 M and 1 M $NH_4NO_3$ solutions.

### 2.5 *Metal ion separations*

For binary separations, 5 g of the ion exchanger in $H^+$ form was taken in a glass column (30 cm × 1·1 cm dia). The column was washed thoroughly with deionized water and the mixture to be separated was loaded on to it maintaining a flow rate of 0·5 ml min$^{-1}$. In all the separations, the cation concentration was maintained at 0·001M concentration and 5 ml of each metal ion solution was taken. The separation of Co(II) from Cu(II), Zn(II) and Pb(II) was achieved by passing a suitable eluant and the metal ion in the effluant was determined quantitatively by EDTA titrations.

## 3. Results and discussion

Chemical analysis indicates the composition of Zr : W to be 1 : 2. Based on this and the TGA data, the proposed formula for ZW is $ZrO_2 \cdot 2WO_4 \cdot 9H_2O$. The number of water molecules was determined using Alberti's formula (Alberti and Torracca 1972). In case of ZWoCP, elemental analysis indicates, % C = 4·908; % H = 2·488 (instrumental elemental analysis) and % C = 5·76; % H = 2·12 (bromination method).

ZWoCP, though stable in HCl (11·3 N) and $H_2SO_4$ (36 N), was stable in $HNO_3$ only up to 0·5 N concentration. ZWoCP was found to be stable in bases such as NaOH and KOH up to 2 M concentration, as evidenced by no change in colour, form or weight of the samples used. ZWoCP was also found stable in ethanol, acetone and diethyl ether.

FTIR spectra of ZW (figure 1a) shows broad bands in the ~ 3400 $cm^{-1}$ region characteristic of asymmetric and symmetric hydroxo-OH and aquo-OH stretching frequency. A sharp medium band at 1620 $cm^{-1}$ is attributed to (H–O–H) bending frequency. The FTIR spectrum of ZWoCP (figure 1b) shows additional bands in the ~ 1580–1460 $cm^{-1}$ region characteristic of the C=C skeletal inplane vibrations. Bands in the ~ 1390–1330 $cm^{-1}$ region are due to the interactions of the –OH bending and C–H stretching frequencies. Weak bands in the ~ 1410–1310 $cm^{-1}$ region and at 1200 $cm^{-1}$ are due to C–O stretching frequency.

The TGA of ZW indicates presence of hydrated water which is lost very slowly between 100°–180°C. TGA of ZWoCP indicates a weight loss at ~ 61°C due to traces of solvent used for washing the exchanger after refluxing. There is a gradual decrease in weight up to 500°C indicative of the dissociation and decomposition of the organic moiety from the support and the condensation of the structural hydroxyl groups.

The IEC of ZW at room temperature is 0·58 meq $g^{-1}$ whereas that of ZWoCP is 0·65 meq $g^{-1}$. A higher value of IEC in case of ZWoCP is due to the additional $H^+$ sites of the ionogenic –OH groups in the benzene ring of the *o*-chlorophenol, besides the electron withdrawing phenyl ring also makes the phenolic (–OH) proton more labile.

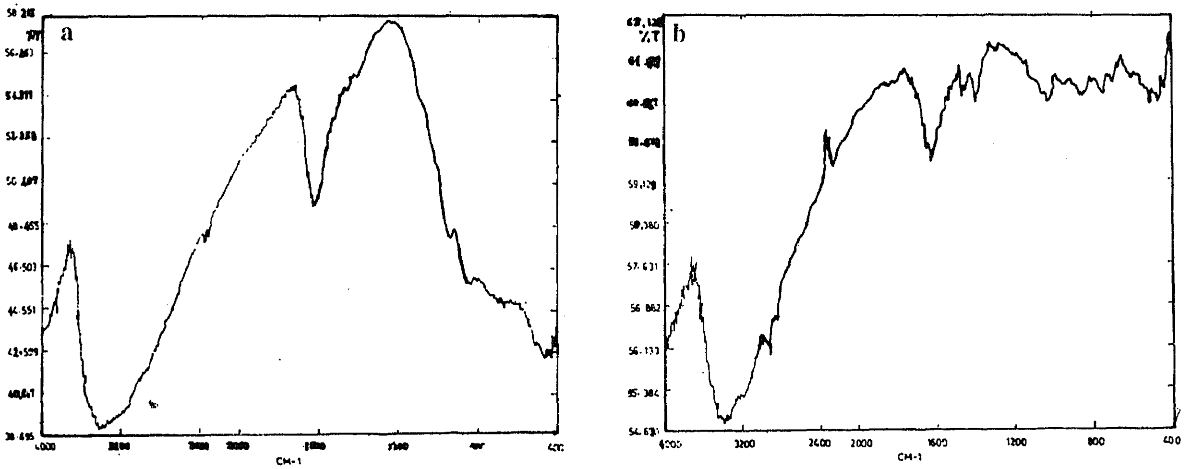

**Figure 1.** FTIR spectrum of **a.** ZW and **b.** ZWoCP.

**Table 1.** Effect of heating on IEC of ZW and ZWoCP.

| Temperature (°C) | Colour change | | Ion exchange capacity (meq · $g^{-1}$) | |
|---|---|---|---|---|
| | ZW | ZWoCP | ZW | ZWoCP |
| RT | White | Yellowish brown | 0·58 | 0·64 |
| 100 | Light brown | Brown | 0·40 | 0·37 |
| 200 | Light brown | Black | 0·36 | 0·21 |
| 300 | White | Black | 0·26 | 0·48 |
| 400 | White | Dark brown | 0·24 | 0·41 |
| 500 | White | White | 0·22 | 0·30 |

**Table 2.** Effect of the electrolyte concentration on the $K_d$ values of metal ions for ZWoCP.

| Metal ion | D.W. | 0·01 M $HNO_3$ | 0·1 M $HNO_3$ | 0·4 M $HNO_3$ | 0·05 M $NH_4NO_3$ | 0·5 M $NH_4NO_3$ | 1 M $NH_4NO_3$ |
|---|---|---|---|---|---|---|---|
| $Cu^{2+}$ | 83·89 | 6·78 | 6·78 | NS | 83·90 | 83·90 | 83·90 |
| $Zn^{2+}$ | 67·20 | NS | NS | NS | 7·29 | NS | NS |
| $Co^{2+}$ | 23·65 | NS | NS | NS | 10·22 | 6·78 | 5·04 |
| $Mn^{2+}$ | 78·92 | NS | NS | NS | 7·32 | 2·04 | NS |
| $Ni^{2+}$ | 16·88 | NS | NS | NS | 15·37 | 13·63 | NS |
| $Pb^{2+}$ | 99·21 | 8·55 | 6·78 | NS | 87·05 | 90·82 | 95·88 |
| $Hg^{2+}$ | 14·36 | 11·94 | 6·78 | NS | 13·76 | 17·84 | 20·81 |
| $Bi^{3+}$ | 1151·70 | 240·43 | 41·46 | NS | 64·00 | 53·84 | 27·59 |
| $La^{3+}$ | NS | NS | NS | NS | NS | NS | NS |
| $Ce^{4+}$ | NS | NS | NS | NS | NS | NS | NS |
| $Th^{4+}$ | 67·20 | 65·15 | 60·23 | 53·30 | 45·41 | 45·00 | 40·00 |

*NS, No sorption

**Table 3.** Metal ion separation for ZWoCP.

| Separation achieved | Eluants | Amount loaded (mg) | Amount eluted (mg) | % Efficiency |
|---|---|---|---|---|
| Co(II)–Cu(II) | 0·05 M $NH_4NO_3$ (Co) | 0·2829 | 0·2593 | 91·66 |
| | 0·01 M HCl (Cu) | 0·3433 | 0·1907 | 55·00 |
| Co(II)–Zn(II) | 0·01 M $HNO_3$ (Co) | 0·2829 | 0·2574 | 91·00 |
| | 0·05 M $NH_4NO_3$ (Zn) | 1·6077 | 1·3714 | 85·30 |
| Co(II)–Pb(II) | 0·05 M $NH_4NO_3$ (Co) | 0·2829 | 0·2652 | 93·00 |
| | 0·01 M $HNO_3$ (Pb) | 1·0774 | 1·0567 | 98·00 |

The results of the effect of heating on IEC are summarized in table 1. For ZW, the IEC decreases on heating. This is due to the condensation of the structural hydroxyl groups bearing the exchangeable protons, at higher temperatures. However in case of ZWoCP, the IEC decreases up to 200°C and then increases for the sample heated at 300°C. Again for the samples heated at 400° and 500°C, the IEC decreases. This may be due to the fact that on heating in the range 200°–300°C, the organic moiety decomposes leading to the formation of active carbon as evidenced by the change in colour of the sample to black. This is responsible for an increase in the IEC and is later lost as $CO_2$ as the heating temperature increases. This fact is also evident from the IR spectra of heated samples of ZW and ZWoCP.

The distribution coefficient ($K_d$) calculated for the metal ions in different electrolyte concentrations for ZWoCP are summarized in table 2. On the basis of the selective affinity for particular metal ions in the presence of electrolytes, the metal ion Co(II) has been separated from Cu(II), Zn(II), and Pb(II). Co(II) has been eluted using 0·05 M $NH_4NO_3$ in all the separations except for Co(II)–Zn(II) separation,,where it is eluted using 0·01 M $HNO_3$. Cu(II), Zn(II) and Pb(II) were eluted using 0·01 M HCl, 0·01 and 0·4 M $HNO_3$ solutions, respectively. The results of the separation study are summarized in table 3.

## 4. Conclusion

ZWoCP exhibits good ion exchange capacity and is stable up to a fairly high temperature, besides exhibiting stability in different acidic, basic and organic media. Its selectivity for particular metal ions enables it to act as an efficient ion exchanger for the separation of Co(II) from Cu(II), Zn(II) and Pb(II) with ~93% efficiency. The DTMA ZWoCP thus exhibits the characteristics of a promising ion exchanger.

## Acknowledgements

Thanks are due to the Head, Department of Applied Chemistry for providing the necessary laboratory facilities. One of the authors (BP) is also thankful to the M.S. University of Baroda, Vadodara for providing a fellowship.

## References

Alberti G 1990 *Pillared layered structures: Current trends and applications* (ed.) I V Mitchell (London: Elsevier) p. 119

Alberti G and Torracca E 1972 *J. Inorg. Nucl. Chem.* **34** 2643

Alberti G and Costantino U 1982 *Intercalation chemistry* (New York: Academic Press Inc.) p. 147

Alberti G and Costantino U 1991 *Intercalation of zirconium phosphates and phosphonates*, in *Inclusion compounds* (eds)

twood, J E D Davies and D D McNicol (London: University Press) **5** p. 136
and Casciola M 1997 *Solid State Ionics* **97** 177
, Costantino U, Allulli S and Tomassini N 1978 *J. Nucl. Chem.* **40** 1113
, Costantino U and Giovagnotti Luciani M L 1980 *J. Nucl. Chem.* **41** 643
, Costantino U, Kornyei J and Giovagnotti Luciani M 2 *Chim. Ind. (Milan)* **64** 115
, Costantino U, Kornyei J and Giovagnotti Luciani M 5 *React. Polym.* **5** 1
, Costantino U, Marmottini F and Perego G 1989 *Gaz. Ital.* **119** 191
, Costantino U, Vivani R and Biswas R K 1992 *React.* **17** 245
, Costantino U, Vivani R and Zappelli P 1993a *Angew. Int. Ed. Engl.* **32** 1357
, Vivani R, Biswas R K and Murcia Mascaros S 1993b *Polym.* **19** 1
, Marmottini F, Murcia Mascaros S and Vivani R 1994 . *Chem. Int. Ed. Engl.* **33** 1594
D, Beneke K and Lagaly G 1976 *Angew. Chem. Int. gl.* **15** 544
Casciola M, Chieli S and Costantino U 1990 *Proc. of the fifth int. conf. on solid state protonic conductors $B_4$* (Assissi, Italy: University of Perugia)
Clearfield A and Stynes J A 1964 *J. Inorg. Nucl. Chem.* **26** 117
Costantino U 1979 *J. Chem. Soc. Dalton Trans.* 402
Costantino U, Massucci M A, La Ginestra A, Tarola A M and Zampa L 1986 *J. Incl. Phenom.* **4** 147
Elving Ph J and Olson E C 1955 *Anal. Chem.* **27** 1817
Kale A, Pandit B, Beena B and Chudasama U 1994 *J.M.S.U.* **XLI** 25
Kornyei J 1982 *II Int. symp. on clatharate compounds and molecular inclusion phenomenon, Parma, Italy* p. 8
Maya L and Danis P O 1980 *J. Chromatogr.* **190** 145
Nabi S A and Rao R K 1981 *J. Indian Chem. Soc.* **11** 1030
Szirtes L, Kornyei J and Poko Z 1988 *React. Polym.* **7** 185
Tomita Isao 1996 *Nippon Ion Kokan Gakkaishi (Jpn)* **7** 174
Vermeulen L A and Thompson M E 1992 *Nature* **358** 656
Vogel A I 1978 *Textbook of quantitative inorganic analysis* (London: Longman Green) IV Ed.
Vogel A I 1989 *Elementary practical organic chemistry, Part III, Quantitative chemistry* (London: ELBS and Longman Group Ltd.)

# Mechanism and control of formation of porous silicon on *p*-type Si

**H SAHA*, S K DUTTA[†], S M HOSSAIN, S CHAKRABORTY and A SAHA**

Department of Electronics and Tele-communication Engineering, Jadavpur University, Calcutta 700 032, India
[†]Department of Physics, City College, Calcutta 700 009, India

MS received 18 August 1997; revised 7 March 1998

**Abstract. A simple extension of Beale's and Lehmann's models for the formation of porous silicon layer on *p*-type silicon is proposed with a view to explain the experimental conditions necessary for obtaining either uniform vertical pores or non-uniform pore branching, as desired. A uniformity parameter is defined and correlated with the measured porosity. The dependence of the porosity and the uniformity factor with the various formation parameters of porous layer are studied experimentally and explained qualitatively.**

**Keywords. Porous silicon; *p*-type Si.**

## 1. Introduction

The discovery of room-temperature photoluminescence (PL) of porous silicon has initiated an extensive research on both theoretical and experimental aspects especially because of its strong potential in its use in optoelectronic and photonic applications.

Porous silicon (PS) is formed by anodic etching of crystalline silicon in hydrofluoric acid. The specific structure of PS depends on various parameters like doping type and level of c–Si, HF concentration, formation current density, presence of illumination, surface morphology etc (Smith and Collins 1992). Depending upon the various parameters during formation, PS may be looked upon as either quantum wires or quantum sponges (Koshida *et al* 1992; Marusak *et al* 1993; Feng and Tsu 1994b; Jain *et al* 1994; Kocka *et al* 1996).

For optoelectronic applications, however, the near-vertical growth of pores and consequently that of the silicon pillars should be a pre-requisite to ensure reproducibility as well as isolation of the devices formed on a single wafer.

In this paper, we report a detailed study on *p*-type silicon to examine the growth of PS under various experimental conditions with a view to find out the favourable formation conditions for near-vertical growth of silicon pillars. The formation model proposed by Lehmann is extended in this paper introducing the concept of a uniformity parameter (Lehmann 1993).

## 2. Modelling of vertical PS growth

The basic prerequisites for electrochemical pore formation are passive state of pore walls and active state of pore tips (Feng and Tsu 1994a). Dissolution of silicon in HF occurs if holes are present in the surface. Thus, a surface depleted of holes is passivated. Hole depletion occurs if any hole reaching the solid–electrolyte interface is immediately consumed in the dissolution reaction. This is the case when the chemical reaction is not limited by the mass transfer in the electrolyte—a condition satisfied when the formation current density is below a critical current density value ($J < J_{\text{ps}}$).

However, when $J > J_{\text{ps}}$, the reaction is limited by mass transfer of ions in the electrolyte. The dissolution of Si is controlled by the supply of reactants through the diffusion layer in the electrolyte, leading to a build up of surface charge in silicon due to accumulation of holes and resulting into electropolishing (Turner 1958).

In equilibrium macropore formation, a steady-state condition is assumed at the pore tips, i.e. the charge transfer due to holes exactly balances the availability of ions in the electrolyte (John and Singh 1995). In such a case, all holes will be consumed at the pore tips itself so that the pores grow vertically downwards with a constant cross-section. This is characterized by critical current density $J_{\text{ps}}$.

Thus, if the localized current density, $J_{\text{tip}}$ at any place is greater than $J_{\text{ps}}$, then the steady-state condition for lateral electropolishing will be achieved when the cross-sectional area to $J_{\text{tip}}$ increases to a value $A_{\text{ps}}$ so that $J_{\text{tip}} = J_{\text{ps}}$. This concept is realized at the initial stage of formation of the porous structure. The initiation of PS structure probably occurs at the locations of random inhomogeneities in the path of current flow through the interface (Beale *et al* 1985).

In regions of the inhomogeneities where the local current density is initially high so that $J_{\text{tip}} > J_{\text{ps}}$, localized lateral electropolishing should occur until $J_{tip}$ becomes equal to $J_{ps}$.

---

*Author for correspondence

If the total number of inhomogeneities (nucleation centres) at the surface is $N_{ps}$, then the current flow ($J_{ps}$ per m$^2$) occurs through an effective area of $N_{ps}A_{ps}$ so that

$$(N_{ps}A_{ps})\,J_{ps}=JA, \tag{1}$$

$A$ is the total cross-sectional area of the same and $J$ the measured current density.

If the growth of pores were uniform, then the porous silicon thickness $h_u$ would be given by

$$(N_{ps}A_{ps})\,h_u\rho=\frac{(JA)\,t}{ne}\times m_s, \tag{2}$$

where $n$ is the number of atoms required for dissolution of each silicon atom and $\rho$ the Si density and $n$, reported to be of the order of 2 (Beale *et al* 1985).

The porosity of vertically grown PS (no branching) will therefore be given by

$$P_u=\frac{(N_{ps}A_{ps})\,h_u\rho}{A\,h_u\,\rho}=\frac{N_{ps}A_{ps}}{A}=\frac{J}{J_{ps}}. \tag{3}$$

It can be seen from (1)–(3) that

$$h_u=\frac{(J_{ps})\,tm_s}{ne\rho}, \tag{4}$$

and

$$P_uh_u=\frac{Jtm_s}{ne\rho}. \tag{5}$$

Thus, when PS growth is vertical, the porosity is a function of $J$ and $J_{ps}$ (in turn, dependent on HF concentration). However, the thickness of PS layer is independent of the current density and is only a function of $J_{ps}$. This happens because of the fact that $A_{ps}$ increases in proportion of $J$ for a constant $J_{ps}$.

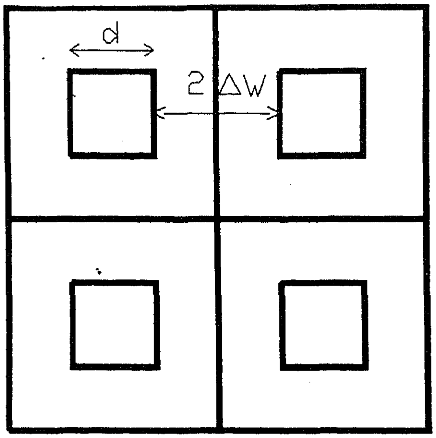

**Figure 1.** Schematic diagram of uniform pores where $d$ is pore diameter and $2\Delta W$ is the separation between two consecutive pores.

If, however, the number of nucleation centres ($N_{ps}$) is very large, then the maximum limit to pore wall thickness is set by the pinch-off effect (Lehmann 1993) due to overlap of adjacent depletion layers so that the porous column dimension is twice the depletion width ($\Delta W$) (figure 1).

Under these circumstances, we have

$$P_u=\left(\frac{d}{d+2\Delta W}\right)^2=\frac{J}{J_{ps}}, \tag{6}$$

and

$$N_{ps}=\frac{A}{(d+2\Delta W)^2},$$

since the number of pores per unit area is $1/(d+2\Delta W)^2$.

Thus, in this case, the porosity becomes a function of the pore diameter and the sample resistivity in the form given by

$$d=\frac{2\Delta W}{\left(\frac{1}{\sqrt{P_u}}-1\right)}, \tag{7}$$

and the formation of pores will be possible only if

$$N_{ps}\le\frac{A}{4\Delta W^2}\ \text{ i.e. }\ n_{ps}\le\frac{1}{4\Delta W^2}. \tag{8}$$

It is quite obvious that heavily doped $p$-type silicon will give rise to a large number of nucleation centres in the vicinity of doping impurities (Beale *et al* 1985), since current flow can occur in such samples by tunneling and a larger fraction of area is then always amenable to offer the path of current flow. Due to the depletion layer width overlap and pinch-off effect, the columnar growth of the pores is highly likely in the case (Beale *et al* 1985; Lehmann 1993).

Equation (7) is indeed obeyed in the case of heavily doped layers as can be seen by inserting the results of Beale *et al* (1985) into (7). The number of nucleation centres necessary for vertical pores is given by

$$N_{ps}\left[\left(\frac{A}{N_{ps}}\right)^{1/2}-2\Delta W\right]^2=\left(\frac{J}{J_{ps}}\right)A. \tag{9}$$

Thus, the number of nucleation centres per unit area ($n_{psc}$) for vertical PS growth (from (9) and (8)) is given by

$$n_{psc}=\frac{N_{ps}}{A}=\left[\frac{1-(J/J_{ps})^{1/2}}{2\Delta W}\right]^2, \tag{10}$$

and the pore dimension $d$ is given by

$$d=\frac{2(\Delta W)}{[(J_{\mathrm{ps}}/J)^{1/2}-1]}\,.$$

Thus the pore dimension is found to be strongly dependent on the doping concentration.

It is obvious that if $n_{\mathrm{ps}}$ is less than $n_{\mathrm{psc}}$, then the pore walls will not be passivated by the pinch-off effect and the branching of the pores will be a possible phenomenon.

The critical nucleation centre density ($n_{\mathrm{psc}}$) decreases and thus approaches towards the actual centre density ($n_{\mathrm{ps}}$) as $J$ approaches $J_{\mathrm{ps}}$ and '$\Delta W$' decreases (i.e for lower resistivity) as long as the actual $n_{\mathrm{ps}}$ is not dependent on either $J$ or $\Delta W$.

## 3. Pore branching and uniformity

The morphology of pores formed depends on a number of parameters such as the surface roughness, doping type and density, anodizing current and voltage, pH and concentration of HF solution etc (Feng and Tsu 1994c). Depending upon these parameters, the pores may have fir-tree-shaped structures with interconnected branches underneath or well-defined unbranched vertical wells. In general, unless the surface is very polished and intentionally patterned, doping density is high and the anodization potential, HF concentration are of right magnitude, the pores exhibit branching and non-uniformity (Lehmann 1993).

The measured porosity ($P_{\mathrm{m}}$) of PS will be different from that for uniform growth due to pore branching and can be expressed as

$$P_{\mathrm{m}}=\frac{\text{mass of silicon dissolved}}{\text{mass of the porous layer}}$$

$$=\frac{\left(\frac{JAt}{ne}\right)\times m_{\mathrm{s}}}{Ah_{\mathrm{m}}\rho}=\left(\frac{Jtm_{\mathrm{s}}}{ne\rho}\right)\times\frac{1}{h_{\mathrm{m}}},\qquad(11)$$

where $h_{\mathrm{m}}$ is the thickness of the porous layer in the direction of external current density. Combining (5) and (11), we have

$$\frac{h_{\mathrm{m}}}{h_{\mathrm{u}}}=\frac{P_{\mathrm{u}}}{P_{\mathrm{m}}}=u,$$

where $u$ is defined to be a measure of uniformity of the formed porous layer. In the case of a vertical pore growth, we have $h_{\mathrm{m}}=h_{\mathrm{u}}$ and $u=1$. The uniformity factor ($u$) can be estimated from the relation

$$u=\frac{P_{\mathrm{u}}}{P_{\mathrm{m}}}=\frac{J/J_{\mathrm{ps}}}{P_{\mathrm{m}}}\,.\qquad(12)$$

The measured porosity ($P_{\mathrm{m}}$) for a given $J$ will be higher due to pore branching than that for a uniform PS growth. At lower current density ($J<J_{\mathrm{ps}}$), holes are depleted from the silicon surface resulting into a preferential transport of holes from the bulk to the surface irregularities. This implies that higher current density will lead to lower non-uniformity (John and Singh 1995).

## 4. Experimental

Silicon wafers of $p$-type and (100) orientation and 7 cm$^2$ area, having resistivity of 1–2 Ω-cm were anodized in a cell specially developed for the purpose. The wafers were texturized by standard anisotropic etching process that leads to the formation of pyramidal structures with exposed (111) planes.

The wafer actually acts as a seal between the front and rear regions. The front region of the cell was filled with HF : $CH_3OH$, while the rear portion was immersed in KCl solution. The back contact metallization was done by screen printing of silver aluminium paste and its subsequent firing. The textured samples were anodized by a constant current supply (Bandopadhyay *et al* 1996).

The gravimetric method was employed to determine the porosity of the samples (Amato 1995). Samples, before and after anodization, were weighed by the micro balance model No ADN200W. Then, the porous layers were removed by dipping the samples in NaOH solution and the wafers were again weighed.

The porosity was then determined by using the relation

$$P_{\mathrm{m}}=\frac{m_1-m_2}{m_1-m_3},$$

where $m_1$ is the mass of the sample before anodization, $m_2$ the mass of the sample after anodization and $m_3$ the mass of the sample after complete dissolution of the porous layer.

SEM techniques have been used to provide some of the detailed direct information about the thickness of the porous layers and the branching of pores in these layers.

## 5. Results and discussion

### 5.1 *Role of formation current density*

Figure 2 shows the variation of measured porosity ($P_{\mathrm{m}}$) as a function of current density ($J$) for a fixed HF concentration (mixed in 1 : 1 proportion with $CH_3OH$) and fixed time of anodization. The porosity ($P_{\mathrm{m}}$) increases with increasing $J$.

The thickness ($h_{\mathrm{m}}$) of the porous layer has been estimated from the mass of the porous layer and is given by

$$h_{\mathrm{m}}=\frac{m_1-m_3}{A\rho}\,.$$

Figure 3 and table 1 show the variation of estimated $h_m$ with the current density ($J$). It is observed that $h_m$ increases with increase in $J$. Figures 4 and 5 show two typical scanning electron micrographs of porous silicon layers at 45° tilt angle. It is seen from these figures and table 1 that the thickness of porous layers as measured by SEM technique agree fairly well with those measured by gravimetric methods.

It has been seen from the simple model presented here that for a given passed charge ($JAt$) more branching will lead to a lower PS layer thickness and consequently higher porosity than that would be observed for uniform vertical pore growth. Thus, it appears from this study that as the fractional increase of $P_m$ ($\Delta P_m/P_m$) is much less than the fractional increase of $J$ ($\Delta J/J$) and since $h_m$ increases with increasing $J$, the average thickness ($h_m$) approaches towards the uniform growth thickness ($h_u$) with increasing $J$.

The degree of uniformity is examined by investigating the variation of the uniformity ($u$) with the formation current density ($J$). Figure 6 shows that with increasing $J$, $u$ is found to increase almost linearly with $J$. Table 1 shows the different values of $P_m$, $h_m$, $u$ and $h_u$ as functions of current density. It is seen from table 1 that $u$ lies in the range 0·04–0·17 for the current densities in the range of 10–70 mA/cm$^2$. This can be explained from the consideration that as the critical density of

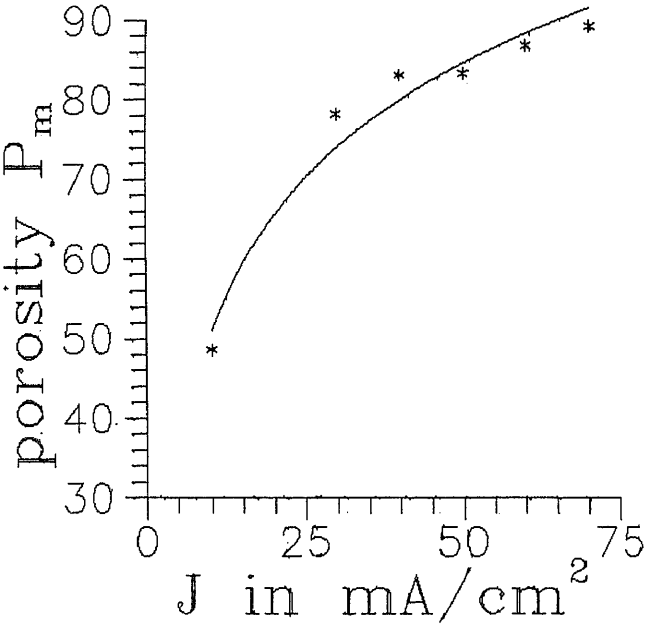

**Figure 2.** Variation of measured porosity ($P_m$%) with etching current density ($J$) when other etching parameters are constant.

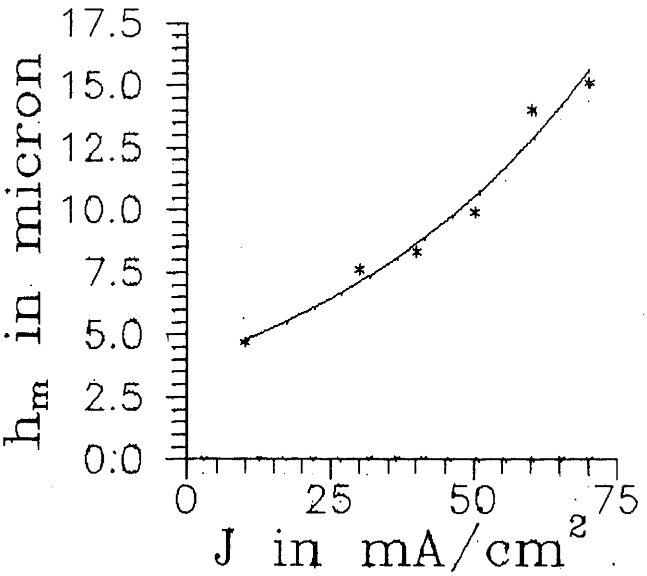

**Figure 3.** Variation of porous layer thickness ($h_m$) with etching current density.

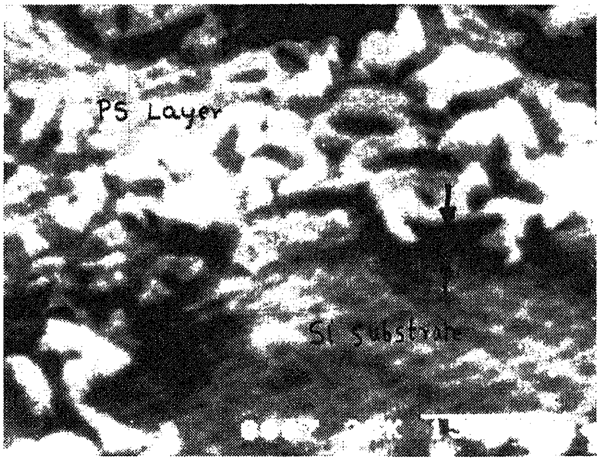

**Figure 4.** SEM of porous silicon formed under anodic etching by $J = 10$ mA/cm$^2$ in 48% HF for 5 min, estimated $h_m = 4{\cdot}25\ \mu$m.

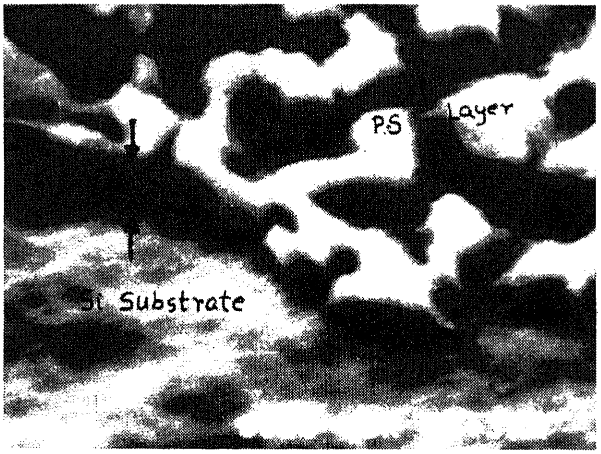

**Figure 5.** SEM of porous silicon formed under anodic etching by $J = 50$ mA/cm$^2$ in 48% HF for 5 min, estimated $h_m = 9{\cdot}6\ \mu$m.

**Table 1.** Values of measured porosity, PS layer thickness for non uniform ($h_m$) and 100% uniform ($h_u$) and uniformity ($u$) for different etching current densities.

| $J$ (mA/cm$^2$) | $P_m$ (%) | $h_m$ ($\mu$m) (from gravimetric method) | $h_m$ ($\mu$m) (by SEM tech.) | $u$ (%) | $h_u$ ($\mu$m) |
|---|---|---|---|---|---|
| 10 | 48·7 | 4·7 | 4·25 | 3·64 | 129 |
| 30 | 78·2 | 7·6 | 7·8 | 6·8 | 112 |
| 40 | 83·1 | 8·3 | 8·6 | 8·5 | 98 |
| 50 | 83·3 | 9·9 | 9·6 | 10·6 | 93 |
| 60 | 86·8 | 14·0 | – | 12·3 | 114 |
| 70 | 89·4 | 15·1 | – | 13·9 | 108 |

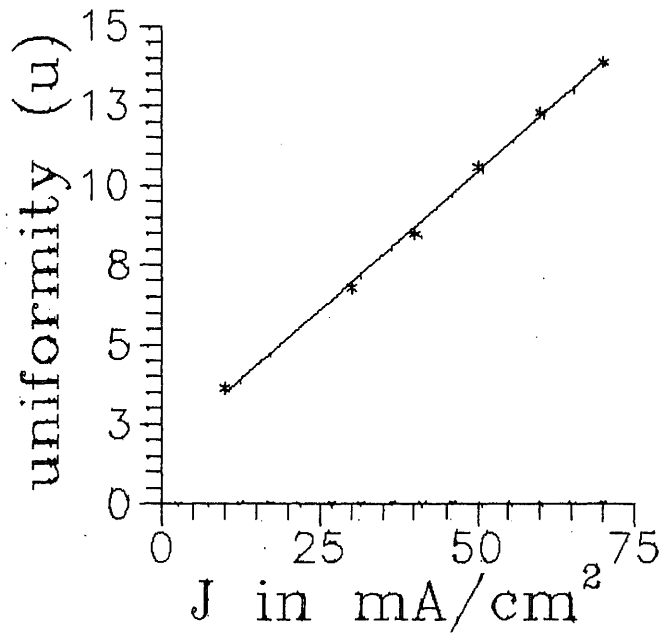

**Figure 6.** Variation of uniformity ($u$%) with etching current density.

nucleation centres ($n_{psc}$) decreases with $J$ almost linearly according to (10), an increase in $J$ will favour the vertical pore growth since the actual density of nucleation centres ($n_{ps}$) approaches $n_{psc}$ with increasing current density.

It is apparent from the present study that in the range of current densities considered here (10–70 mA/cm$^2$), the uniformity factor is not very high ($\leq 0{\cdot}17$). The uniformity factor is increased by increasing $J$, but it is likely that at high current density the pore tips lead to increased oxide formation (Feng and Tsu 1994c). Thus, it seems that it is preferable to either increase $n_{ps}$ by pattern formation on the surface and creating the required value of $n_{ps} \approx n_{psc}$ and/or lowering the value of $n_{psc}$ by increasing $\Delta W$ or in other words, decreasing the doping concentration of the sample.

The fact that the anodizing current mainly flows through the pores and not through the whole area ($A$) of the sample was examined by calculating the number of electrons required for the removal of every silicon atom estimated from the weight change of the wafer during anodization as follows:

**Table 2.** Number of electrons ($n$) required for dissolution of one silicon atom during electrochemical etching of $p$-type Si for different values of etching current density ($J$).

| $J$ (mA/cm$^2$) | $m_1$ (g) | $m_2$ (g) | $m_s$ (g) | $n$ |
|---|---|---|---|---|
| 10 | 1·0251 | 1·0214 | $4{\cdot}656 \times 10^{-23}$ | 1·7 |
| 30 | 0·9987 | 0·989 | | 1·9 |
| 40 | 1·1263 | 1·115 | | 2·2 |
| 50 | 1·0431 | 1·0296 | | 2·3 |
| 60 | 0·9769 | 0·9571 | | 1·9 |
| 70 | 1·081 | 1·059 | | 1·9 |

$$(m_1 - m_2) = \frac{JAt}{ne}\, m_s, \tag{13}$$

where $m_s$ = mass of each Si atom.

It is found that $n$ is of the order of 2 indicating that the flow is essentially through the pores and on an average, two electrons are required for each silicon atom removal. It was, however, observed (table 2) that $n$ increases in general with increasing $J$ and values of $n$ were found to lie in the range 1·7–2·3.

### 5.2 *Role of methanol content in HF electrolyte*

The role of methanol in the formation of PS layer has been examined by anodization of silicon in the same HF concentration with different proportions of methanol.

It is seen from table 3 and figures 7 and 8 that with increasing methanol proportions in HF, the average PS layer thickness and the uniformity factor ($u$) decreases for a given current density. This is possibly because of the fact that methanol acting as a wetting agent removes the hydrogen bubbles from the pore walls leading to the branching of pores.

The pore formation rate (average thickness per unit time) is found to follow the relation

$$r = 10^{[0{\cdot}89 \times \log_{10} J - 1{\cdot}2]}, \tag{14}$$

as suggested by Lehmann *et al* (Feng and Tsu 1994a) for 1 : 1 HF (48%)–methanol electrolyte.

### 5.3 *Role of HF concentration*

Figures 9 and 10 show the dependence of porosity and uniformity factor with increasing HF concentration. It is found that porosity increases linearly with HF concentration, whereas the uniformity factor decreases.

This can be explained with reference to the change in $n_{psc}$. As HF concentration increases, the value of $J_{ps}$ also increases leading to the increase of the critical nucleation centre density needed for near vertical growth. This leads to lower values of $n_{ps}/n_{psc}$ with increasing HF concentration and thus more pore branching. This observation is further corroborated by reflectance studies of PS (to be communicated separately).

The fact that increase of HF concentration leads to less uniformity and consequently more pore branching can be observed directly by examining the SEM micrographs taken from a direction perpendicular to the thickness of porous layer (figures 11 and 12). The black

**Table 3.** Values of measured porosity ($P_m$), PS layer thickness ($h_m$) and uniformity ($u$) for different methanol proportions in the electrolyte.

| $CH_3OH$ : HF | $P_m$ (%) | $h_m$ ($\mu$m) | $u$ (%) |
|---|---|---|---|
| 1 : 1 | 78·0 | 6·3 | 6·8 |
| 1 : 2 | 75·0 | 7·4 | 7·1 |
| 1 : 3 | 74·4 | 8·2 | 7·2 |
| 1 : 5 | 72·4 | 8·9 | 7·3 |
| 0 : 1 | 51·5 | 9·9 | 10·3 |

**Table 4.** Values of measured porosity ($P_m$), PS layer thickness ($h_m$) and uniformity ($u$) for different HF concentrations.

| C (wt%) | $P_m$ (%) | $h_m$ ($\mu$m) | $u$ (%) |
|---|---|---|---|
| 48 | 83 | 2·5 | 2·1 |
| 36 | 74 | 2·1 | 3·2 |
| 30 | 77 | 1·3 | 3·7 |
| 24 | 63 | 2·3 | 5·6 |
| 18 | 61 | 2·0 | 7·6 |

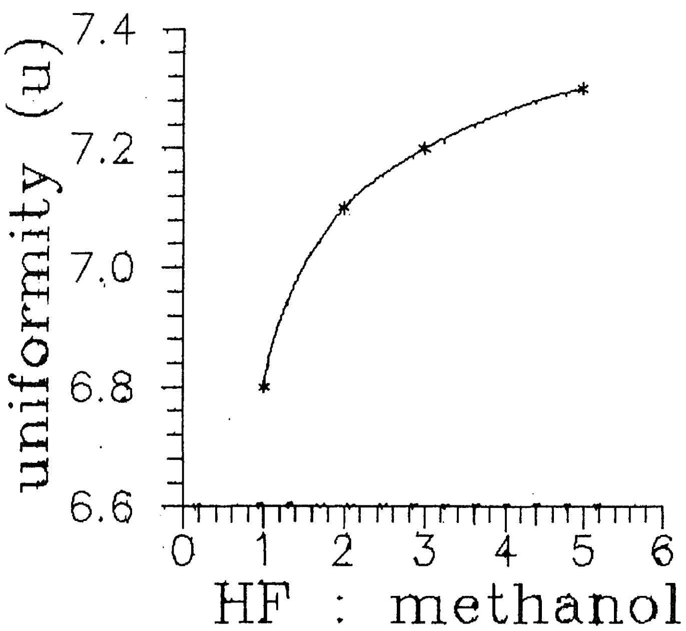

**Figure 8.** Variation of uniformity ($u$%) with HF, methanol ratio in the electrolyte.

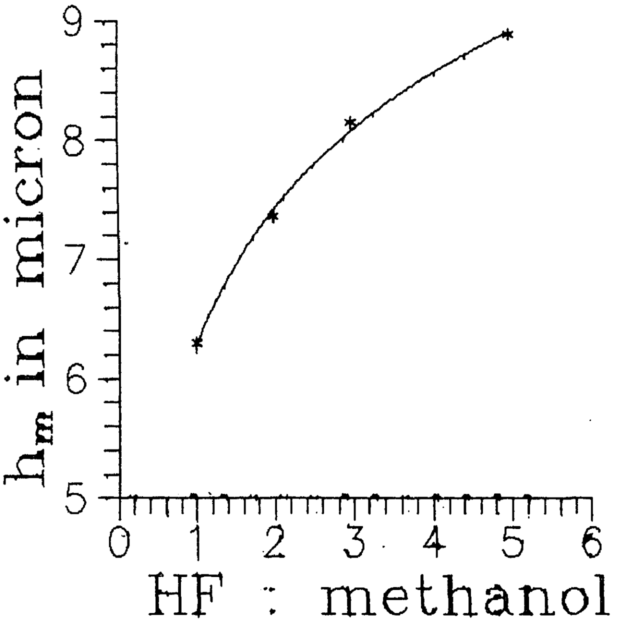

**Figure 7.** Variation of PS layer thickness ($h_m$) with HF, methanol ratio in the electrolyte.

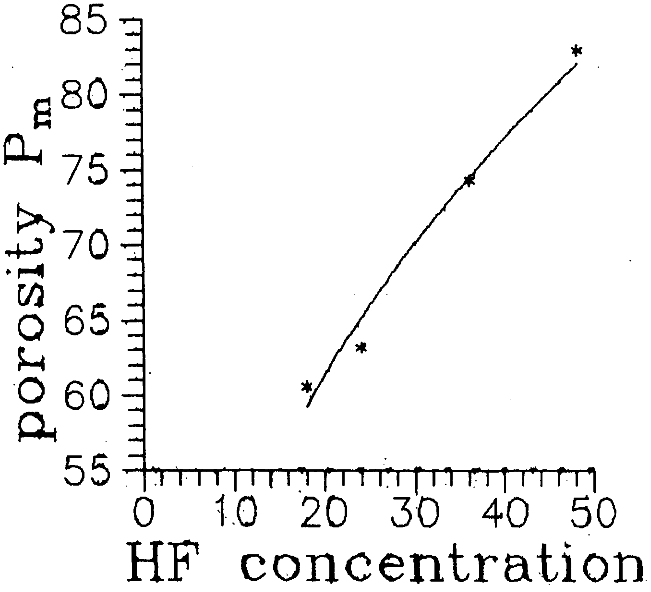

**Figure 9.** Variation of measured porosity ($P_m$%) with HF concentration (wt%).

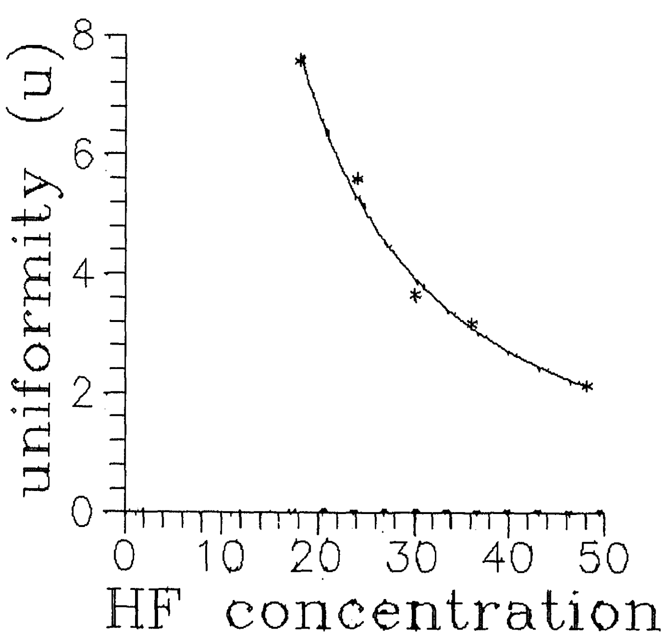

**Figure 10.** Variation of uniformity ($u$%) with HF concentration (wt%).

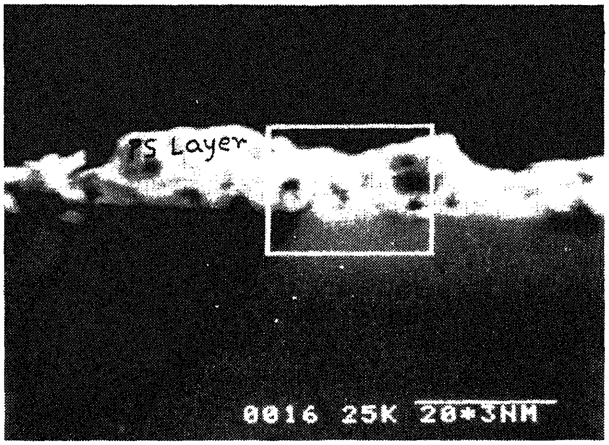

**Figure 11.** SEM micrograph of porous silicon (HF = 24%, $J = 10$ mA/cm$^2$) showing branching of pores.

holes in these micrographs show pores formed in the direction perpendicular to the thickness of porous layers and thus these indicate the branching of pores. Figures 11 and 12 clearly show that more branching occurs at higher HF concentration.

## 6. Conclusions

A simple model based on Beale's and Lehmann's ideas, for uniform porous layer formation on $p$-Si has been developed correlating the various growth parameters of vertical and uniform pores with the pore formation parameters. A concept of non-uniformity has been introduced to characterize the quality of PS layer in respect of pore-branching and near-vertical growth of pores. A factor called 'uniformity factor' has been defined and its dependence on experimental and physical parameters of porous layer studied. The simple model developed here has been utilized to explain the different experimental observations.

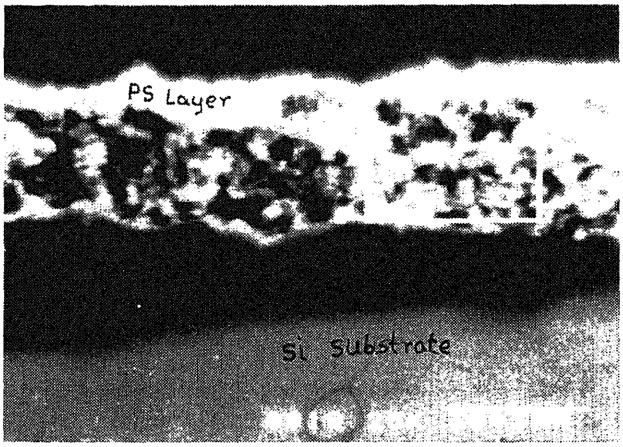

**Figure 12.** SEM micrograph of porous silicon (HF = 48%, $J = 10$ mA/cm$^2$) showing branching of pores.

With increase in $J$ and/or decrease in HF concentration, the uniformity factor increases leading to better vertical growth. With more methanol proportion in HF electrolyte, the uniformity factor decreases giving more branching. The results can be explained with reference to the critical density of nucleation centres on the silicon surface.

## Acknowledgements

The authors wish to acknowledge with gratitude the help and cooperation received from Dr Utpal Gangopadhyay, Dr Sikha Bandopadhyay and other members of the IC Design and Fabrication Centre. Thanks are also due to the Department of Science and Technology, New Delhi for sanctioning the research project on Porous Silicon.

## References

Amato G 1995 *Jpn. J. Appl. Phys.* **34** 1716
Bandopadhyay S *et al* 1996 *Bull. Mater. Sci.* **15** 725
Beale M I *et al* 1985 *J. Cryst. Growth* **73** 622
Feng Z C and Tsu R 1994a *Porous Silicon (WS)* 17
Feng Z C and Tsu R 1994b *Porous Silicon (WS)* 99
Feng Z C and Tsu R 1994c *Porous Silicon (WS)* 301
Jain V K *et al* 1994 *Bull. Mater. Sci.* **17** 551
John G C and Singh V A 1995 *Phys. Rep.* 263
Kocka J *et al* 1996 *Thin Solid Films* **276** 187
Koshida N *et al* 1992 *Appl. Phys. Lett.* **60** 20
Lehmann V 1993 *J. Elec. Soc.* **140** 2836
Marusak H P *et al* 1993 *Appl. Phys. Lett.* **63** 5
Smith R L and Collins S D 1992 *J. Appl. Phys.* **71** 1
Turner D R 1958 *J. Elec. Chem. Soc.* 402

# Phase diagram and thermochemical properties of organic eutectic in a monotectic system

**U S RAI*** **and R N RAI**
Department of Chemistry, Banaras Hindu University, Varanasi 221 005, India

MS received 16 May 1997; revised 10 March 1998

**Abstract. The phase diagram of a binary organic system involving diphenyl and succinonitrile shows the formation of a eutectic (0·968 mole fraction of succinonitrile) and a monotectic (0·074 mole fraction of succinonitrile) with a large miscibility gap in the system, the upper consolute temperature being 53·5°C above the monotectic horizontal. From the enthalpy of fusion of the pure components, the eutectic and the monotectic, determined by the DSC method, the enthalpy of mixing, Jackson's roughness parameter, interfacial energy, size of the critical nucleus and excess thermodynamic functions were calculated.**

**Keywords. Phase diagram; monotectic system; thermochemistry; organic eutectic; organic monotectic.**

## 1. Introduction

The fundamental understanding of solidification (Elliott 1983; Herlach *et al* 1993; Glazer 1995; Rzyman *et al* 1996) and properties of polyphase alloys has become a subject of potential investigation during the past two decades. Due to low transformation temperature, ease in purification, transparency, wider choice of materials, minimized convection effects and simplicity of experimentation, organic systems (Glicksman *et al* 1983; Ecker *et al* 1989; Grugel and Poorman 1989; Podolinsky *et al* 1989; Sangster 1994; Trivedi and Kurz 1994; Favite 1996; Yasuda *et al* 1996) are better than metallic systems for scientific investigations. Succinonitrile is a low enthalpy of fusion material and solidifies like a metal. In contrast, diphenyl is a high enthalpy of fusion material and solidifies like a nonmetal. As such a system involving succinonitrile (SCN) and diphenyl (DP) is an organic analogue of metal–nonmetal system giving eutectic and monotectic alloys. Preliminary investigations on this system have already been published earlier (Rai and Rai 1996). However, in the absence of thermal data many aspects of this system could not be properly analysed. In view of this, phase diagram and thermochemistry of this system are reported here.

## 2. Experimental

### 2.1 *Materials and purification*

Diphenyl obtained from Sojuz Chem., Moscow was purified by fractional crystallization with ethanol. Succinonitrile (Aldrich, Germany) was purified by repeated distillation under vacuum. The purity of each compound was checked by determining melting point.

### 2.2 *Phase diagram*

Phase diagram of SCN–DP system was determined by the thaw-melt method (Rai and Mandal 1990). In this method mixtures of two components covering the entire range of composition are prepared in long-necked test tubes. The thawing and melting temperatures of each mixture were determined using a Toshniwal melting point apparatus attached with a thermometer which could read correctly up to ±0·5°C. A graph between melting temperature and composition gives the phase diagram.

### 2.3 *Enthalpy of fusion*

The values of enthalpy of fusion of each of the pure components, the eutectic and the monotectic, were determined by the DSC method using Mettler DSC-4000 system. Indium metal was used to calibrate the system. Amount of sample and rate of heating were about 5 mg and 10°C/min, respectively, for each estimation. The maximum percentage error in the experimental value is 2.

## 3. Results and discussion

### 3.1 *Phase diagram*

The phase diagram of SCN–DP system is given in figure 1. The melting temperature of diphenyl decreases with increase in concentration of succinonitrile. When concentration of succinonitrile is 0·074 mole fraction, liquid immiscibility appears (Rai and Rai 1996). At this composition which corresponds to 66·5°C melting temperature, two liquid phases, $L_1$ and $L_2$ and a solid phase are in equilibrium. This is the monotectic temperature and the composition corresponding to this temperature is the monotectic composition. When a liquid of monotectic composition is cooled below the monotectic temperature ($T_m$), the monotectic reaction occurs and a liquid, $L_1$ which is rich in DP decomposes into a solid phase $S$ (rich in DP) and another liquid $L_2$ (rich in SCN) according to the reaction,

---

*Author for correspondence

$$L_1\,(\text{rich in DP}) \rightleftharpoons \text{DP}(S) + L_2\,(\text{rich in SCN}). \quad (1)$$

When composition of succinonitrile is increased beyond 0·074 mole fraction, in a wide range area indicated by $L_1 + L_2$, the two immiscible liquids are observed. At 0·968 mole fraction of succinonitrile there is a eutectic point and at this temperature two solid phases and a liquid phase are in equilibrium. When a liquid of eutectic composition is allowed to cool below the eutectic temperature ($T_E$), the liquid decomposes to

$$L_1\,(\text{rich in SCN}) \rightleftharpoons S_1\,(\text{rich in DP}) + S_2\,(\text{rich in SCN}). \quad (2)$$

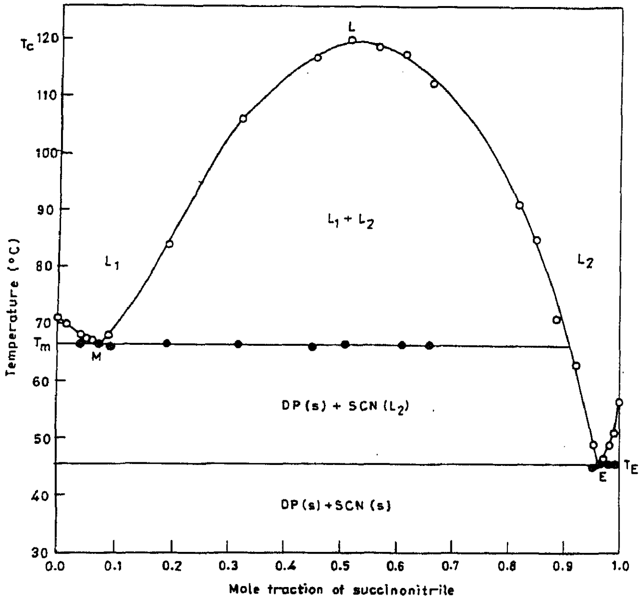

**Figure 1.** Phase diagram of diphenyl–succinonitrile system (o Melting temperature; • thaw temperature).

### 3.2 *Thermochemistry*

It is well known that phase transformation involves two steps: (i) nucleation, and (ii) growth. While the nucleation mechanism depends on the solid–liquid interfacial energy, the growth mechanism depends on the manner in which particles from the liquid phase are added at the solid–liquid interface. The interface structure further depends on the entropy of fusion of the material under investigation and also upon the thermal environment in which the crystal is growing. Both the parameters, viz. interfacial energy and entropy of fusion can be calculated from the enthalpy of fusion data. Apart from this, radius of the critical nucleus, enthalpy of mixing, Jacksons roughness parameter and excess thermodynamic functions can also be calculated to throw light on the mechanism of solidification and formation of different microstructures of the eutectic and the monotectic.

3.2a *Enthalpy of mixing*: The values of enthalpy of fusion of the pure components, the eutectic and the monotectic, determined by the DSC method are given in table 1. For the purpose of comparison the enthalpy of fusion of the eutectic, calculated by the mixture law (Rai and George 1996), is also given in the same table. If the eutectic is a simple mechanical mixture involving no interaction, the value of enthalpy of fusion determined experimentally and calculated by the mixture law should be the same. The enthalpy of mixing ($\Delta_m H$) (Rai and Shekhar 1994), which is the difference between the experimental value of the enthalpy of fusion and the calculated value of the enthalpy of fusion, is 0·4 kJ mol$^{-1}$ in the present system. Thermochemical studies (Singh *et al* 1985; Rai *et al* 1987) suggest that the structure of eutectic melt depends on the sign and the magnitude of the enthalpy of mixing. Three types of structures are suggested, quasi-eutectic for $\Delta_m H > 0$, clustering of mole-

**Table 1.** Heat of fusion, entropy of fusion and roughness parameter.

| Material | Heat of fusion (kJ · mol$^{-1}$) | Entropy of fusion (J · mol$^{-1}$) | Roughness parameter ($\alpha$) |
|---|---|---|---|

**Table 2.** Interfacial energy of diphenyl, succinonitrile and their eutectic and monotectic.

| Parameter | Value (erg $cm^{-2}$) |
|---|---|
| $SL_1$ (DP) | 30·3 |
| $SL_2$ (SCN) | 9·3 |
| E (DP–SCN) | 10·0 |
| $L_1L_2$ (DP–SCN) | 6·0 |

**Table 3.** Radius of critical nucleus at different degrees of undercoolings.

| Undercooling ($\Delta T$°C) | Critical radius ($\times 10^8$ cm) | | |
|---|---|---|---|
| | DP | SCN | Eutectic |
| 2·5 | | 6·65 | |
| 3·0 | | 5·55 | 4·62 |
| 3·5 | | 4·75 | 3·96 |
| 4·0 | | 4·16 | |
| 4·5 | | 3·70 | 3·08 |
| 5·0 | 2·25 | | 2·77 |
| 5·5 | 2·05 | | |
| 6·0 | 1·88 | | |
| 7·0 | 1·61 | | |
| 9·0 | 1·25 | | |

cules for $\Delta_m H < 0$ and molecular solution for $\Delta_m H = 0$. The value of $\Delta_m H$ being $+0{\cdot}4\,\mathrm{kJ\,mol^{-1}}$, suggests quasi eutectic structure (Rai *et al* 1987) in the eutectic melt.

3.2b *Entropy of fusion and excess thermodynamic functions*: Theoretical studies on the entropy of fusion and calculation of some excess thermodynamic functions of eutectic predict the structure, stability and ordering in the eutectic melt. The values of entropy of fusion ($\Delta_f S$) of the pure components and eutectic were calculated using the equation,

$$\Delta_f S = \frac{\Delta_f H}{T}, \tag{3}$$

where $\Delta_f H$ is the enthalpy of fusion, $T$ the fusion temperature. The value of entropy of fusion being positive suggests that there is an increase in randomness during melting. Entropy factor is more effective in the eutectic in comparison to that of succinonitrile. On the other hand, it is less effective in comparison to that of diphenyl.

The deviation from ideal behaviour and quantitative measure of molecular interactions can be expressed in terms of excess thermodynamic functions. They are given by the difference between the thermodynamic function of mixing for a real system and the corresponding value for an ideal system at the same temperature and pressure.

$$Y^E = \Delta_{mix} Y(\text{real}) - \Delta_{mix} Y(\text{ideal}), \tag{4}$$

where $Y$ is any of the thermodynamic functions. These functions can be calculated using the method reported earlier (Rai *et al* 1983). The value of $Y^E$ being positive ($210{\cdot}7\,\mathrm{J\,mol^{-1}}$) suggests (Wisniak and Tamir 1978) that associative interaction between like molecules is stronger than that between unlike molecules.

3.2c *Interfacial energy and size of critical nucleus*: When a liquid is cooled below its equilibrium melting temperature, the liquid phase does not solidify spontaneously because, under equilibrium condition, it contains clusters of molecules. So long as the clusters are all below the critical size (Christian 1965), they cannot grow to form crystals and so no solid is formed. The

$$r^* = \frac{2\cdot\sigma T_m}{\Delta_f H\cdot\Delta T}, \tag{5}$$

where $T_m$, $\Delta_f H$ and $\Delta T$ are melting temperature, heat of fusion and degree of undercooling, respectively. The interfacial energy is given by the relation

$$\sigma = \frac{C\cdot\Delta_f H}{(N)^{1/3}(V_m)^{2/3}}, \tag{6}$$

where $N$ is the Avogadro number, $V_m$ the molar volume and parameter $C$ lies between 0·30 and 0·33. The values of interfacial energy calculated using (6) are given in table 2. The critical size of the nucleus for pure components and the eutectics is given in table 3. It is evident from the reported data that for a sample, the size of the critical nucleus decreases with an increase in the undercooling. This is due to an increase in the amplitude of vibration resulting from an increase in the undercooling.

## Acknowledgement

Authors thank CSIR, New Delhi for providing financial assistance.

## References

Christian J W 1965 *The theory of phase transformations in metals and alloys* (Oxford: Pergamon Press)
Ecker A, Frazier D O and Alexander J I D 1989 *Metall. Trans.* **A20** 2517
Elliott R 1977 *Int. Met. Rev.* **22** 161
Elliott R 1983 *Eutectic solidification processing* (London: Butterworths)
Favite G 1996 *J. Cryst. Growth* **166** 29
Glazer J 1995 *Int. Mater. Rev.* **40** 65
Glicksman M E, Singh N B and Chopra M 1983 *Manufacturing in Space* **11** 207
Grugel R N and Poorman R 1989 *Mater. Sci. Forum* **50** 89

Rai U S and Mandal K D 1990 *Mol. Cryst. Liq. Cryst.* **182** 387

Rai U S and Shekhar H 1994 *Cryst. Res. Technol.* **29** 551

Rai U S and George S 1996 *J. Thermal Anal.* **46** 1809

Rai U S and Rai R N 1996 *Thermochim. Acta* **277** 209

Rai U S, Singh O P, Singh N P and Singh N B 1983 *Thermochim. Acta* **71** 373

Rai U S, Singh O P and Singh N B 1987 *Can. J. Chem.* **65** 2639

Rzyman K, Moser Z, Watson R E and Weinert M 1996 *J. Phase Equilibria* **17** 173

Sangster J 1994 *J. Phys. Chem. Ref. Data* **23** 295

Singh N B 1978 *Acta Ciencia Indica* **4** 4

Singh N, Singh N B, Rai U S and Singh O P 1985 *Thermochim. Acta* **95** 291

Trivedi R and Kurz W 1994 *Int. Mater. Rev.* **39** 49

Wisniak J and Tamir A 1978 *Mixing and excess thermodynamic properties* (*A literature source book*), in *Phys. Sci. Data* (New York: Elsevier)

Yasuda H, Ohnaka I, Matsunaga Y and Shiohara Y 1996 *J. Cryst. Growth* **156** 128

# Thermally stimulated current and electrical conduction in metal (1)–ethyl cellulose–metal (1)/(2) systems

**P K KHARE*, ASHISH VERMA[†] and SUNIL K PALIWAL**

Department of Postgraduate Studies and Research in Physics, Rani Durgavati Vishwavidyalaya, Jabalpur 482 001, India

[†]Department of Physics, Dr H S Gaur University, Sagar 470 001, India

MS received 11 April 1997; revised 12 August 1997

**Abstract. Depolarization current characteristics of solution grown pure ethyl cellulose (EC) films of about 20 $\mu$m thickness have been studied as a function of electrode materials at constant poling field ($5 \times 10^4$ V/cm) and poling temperature 40°C. Thermally stimulated current (TSC) thermograms of EC consists of two well resolved peaks (located at 60°C and 140°C) for Al–Al system, which are attributed to the deorientation of strongly attached ethoxy groups of glycosidal units and diffusion of space charges either at electrodes or due to their thermal release at higher temperatures from the defect levels. For dissimilar electrode combinations (Al–Ag/Cu/Au/Sn/Pb), an indication of peak of lower magnitude at around (50–70°C) alongwith a higher temperature peak (140–155°C), have been observed. TSC parameters are found to change with the choice of electrode material. The dependence of dark current at 40°C in metal–ethyl cellulose–metal systems on applied voltage in the range $(2{\cdot}0\text{–}5{\cdot}0) \times 10^4$ V/cm has also been studied. The results of current–voltage measurement on EC have been interpreted to show that the Schottky–Richardson mechanism is the controlling transport mechanism. Zero field current density extrapolated from $I$–$E^{1/2}$ plots are found to vary with metal work function.**

**Keywords. Thermally stimulated current; electrical conduction; ethyl cellulose; space charge relaxation; dipolar orientation; Schottky–Richardson mechanism.**

## 1. Introduction

Thermally stimulated discharge (TSD) of polymers has become a widely used experimental technique for the investigation of various material parameters such as charge storage properties, determination of the mean depth of the internal charge, activation energies of traps and the trap structure of the material. The importance of carrier injection (Gutman and Lyons 1967; Koton 1968; Lampert and Mark 1970) for the explanation of electrical properties of organic solids has been long recognized. It is only in recent years that the possibility of technological application of electrification of polymers due to their contacts with metal has been discovered (Shrivastava *et al* 1981). The availability of new measuring techniques such as photocurrent (Wintle 1974) and thermally stimulated discharge (TSD) current (Turnhout 1975) has freshened interest in achieving a better understanding and application of the phenomena. Many studies and reviews (Pulfrey 1972; Kryozewski 1975; Khare and Srivastava 1992a, 1994; Khare *et al* 1994a) have been devoted to the problem of contacts and surface charge influence but there is controversy about the causes of the polarity and amount of charge transferred under given conditions.

Ethyl cellulose (EC) is a thermally stable polymer that exhibits excellent chemical resistance and good mechanical properties and probably there is no report on contact electrification of EC using different metal contacts. Hence, it is worthwhile to investigate electret forming characteristics of EC in contact with metals providing a range of work functions. In view of this an analysis of the thermally stimulated current (TSC) and steady state current–voltage ($I$–$V$) characteristics of EC polarized under identical conditions with a special reference to the nature of the electrode metals has been made to elucidate the electrode effect on injection in the polymer.

## 2. Experimental

The isothermal immersion technique was utilized for preparing thin films of ethyl cellulose (EC). The solution was prepared in a glass beaker by first dissolving 2·1 g EC in 30 ml of chemically pure chloroform at room temperature and continuously stirred for 30 min by means of a teflon-coated magnetic stirrer. Thereafter, it was stirred and heated to 40°C to yield a homogeneous solution. The glass beaker containing the solution was

---

*Author for correspondence

Ultrasonically cleaned vacuum metallized microscopic glass slides were immersed vertically into the solution for a period of about 30 min. After deposition of the film the glass slide was taken out and dried in an oven at 40°C for 24 h. This was followed by room temperature outgassing at $10^{-5}$ torr for a further period of 24 h. Aluminium, copper, silver, lead, tin and gold metals were vacuum deposited on the upper surface of the film to obtain a sandwich configuration. The following electrode combinations were used—Al–Al, Al–Ag, Al–Cu, Al–Pb, Al–Sn and Al–Au. The preparation of electrodes and measurement of thickness were the same as reported earlier (Khare and Srivastava 1992; Khare *et al* 1994b). The voltage was applied from a high voltage unit EC-4800 D and current was recorded with an electrometer (Keithley 600B), which was carefully shielded and grounded to avoid ground loops or extraneous electrical noise, at a linear heating rate of 4 K/min. The thickness of the sample was of the order of 20 $\mu$m which was estimated by measuring the capacitance of the fabricated sandwiches taking the value of dielectric constant $\varepsilon$ of ethyl cellulose as 3.

In the present case EC thermoelectrets were formed by a thermal method under identical polarizing conditions of temperature ($T_p$), higher field ($E_p$) and time ($t_p$), viz. 40°C, $5\cdot0 \times 10^4$ V/cm and 120 min but with different metal electrodes, namely copper, silver, lead, tin and gold, having different work functions. Thermoelectrets were shorted for 5 min to eliminate stray charges. The method of polarization of sample and measurement of TSC and steady current were same as reported earlier (Khare and Srivastava 1992; Khare *et al* 1993).

Below 40°C it was difficult to measure the small currents generated by voltage application in the measuring set up. The film was kept at 40°C for about 2 h and then a voltage was applied and the transient behaviour of the current was noted. Voltage application gave a current which was found to decrease to a much lower value in a matter of 2–5 min and then very slowly attain an almost steady value in a few hours. The same procedure was followed to observe the steady value of current at each step of voltage increment.

The depolarization kinetic data, activation energy ($E$), charge released ($Q$) and relaxation time ($\tau_0$) for the observed peaks have been calculated using initial rise method of Garlick and Gibson (1948), Simson's rule and Bucci *et al* (1966) theory, respectively (table 1).

## 3. Results and discussion

Thermally simulated current (TSC) thermograms of ethyl cellulose (EC) samples formed by incorporating aluminium, copper, silver, lead, tin and gold as electrode metals with polarizing field, $E_p = 5\cdot0 \times 10^4$ V/cm at $T_p = 40$°C are shown in figure 1. In all the cases of electrode variation, an indication of peak at lower lying in between 140–155°C have been observed. For Al–Al system, TSC thermograms are characterized with two peaks located at 60° and 140°C, respectively. Current–voltage ($I$–$V$) characteristics of EC at 40°C with polarizing fields $(2\cdot0\text{–}5\cdot0) \times 10^4$ V/cm using different metal electrodes in $I - E^{1/2}$ form are shown in figure 2. It is clear from figures 1 and 2 that the current through the sample is greater when the upper electrode aluminium is replaced by silver, copper, tin, lead or gold.

The TSC thermograms are characterized by various peaks, due to dissipation of charges arising because of polarizations during charging process. The polarization of the material may arise due to various mechanisms, the important of which are dipole orientation, charge displacement, molecular and domain structures, macro/microscopic displacement of ions with subsequent trapping, surface and space charge polarization etc. The trapping centres originate in the transition of the crystalline state into amorphous regions, in the rearrangement of molecules in the polymer chain and from the presence of impurities and defects in the materials. The various defects, in addition to giving rise to their own characteristic trapping levels, can also combine with other trapping centres present around them, and thus they can modify qualitatively as well as quantitatively the TSC spectra observed under polarizing conditions. EC is known to be a partial polar polymer. Its main chain is C–O–C. The side groups also have a structure of the form C–O–C but they differ in electronegative nature from the main chain. The electronegativity of the main chain bond arises from the difference in the electronegativity of carbon and oxygen atoms; however, the electronegativity of the side groups arises from the difference in electronegativity of $H_2C–O–C_2H_5$ and $C–O–C_2H_5$ bonds in the side chains. The slight polar nature of the polymer is due to the difference in electronegativity of the main chain and the side groups. The dipolar relaxation is maximum around the glass transition temperature ($T_g$). Its $T_g$ lies in the temperature range 60–75°C for its atactic form and around 80°C for high molecular weight ethyl cellulose. In view of above characteristic of the polymer, it is expected to get first peak around 60–80°C. This peak seems to be due to the orientation of strongly attached ethoxy groups of glycosidal units. The relaxation process has been found to be associated with an activation energy of 0·18 eV and related to the segmental rotations or translations of the main chain (Khare *et al* 1996). It remains unaffected with heating rate and storage time (Khare and Srivastava 1993). The peak current is almost linearly dependent on poling field. It is suggestive of the dipolar polarization (Khare *et al* 1992). The second peak appears on the higher temperature side of the TSC thermograms. This peak may be considered due to space charge polarization arising out of localization of bulk generated and/or injected charge carriers in various available traps distributed energetically and spatially over the bulk of the sample. The joint motion/deorientation of the backbone chains of EC may be considered to contribute to some extent to this peak. The charge released from the trap levels at temperatures greater than $T_g$ are very well documented previously (Dubey *et al* 1990; Khare *et al* 1992; Khare and Srivastava 1993). An indication of peak of smaller magnitude (around 50–70°C) alongwith a broad TSC peak around 140–155°C have been found for dissimilar electrode combinations. These are space charge peaks modified by the type of metal (Shrivastava *et al* 1979), probably because the various metal–polymer interfaces possess different charge exchange rates, which change the space charge storage and current released by diffusion. The first stage of charging is carrier injection and the second stage is the entrapment of these charges in the border layer (Hino and Yamashita 1974). Consequently, the interpretation of depolarization appears to be reasonably possible in terms of charge detrapping of a space-charge build up due to carriers injected from the electrodes (Shatzkes 1978). At high fields, the charges are injected from the electrodes into the polymer film and then trapped. It is only at temperatures above the glass transition of EC that the molecular chains are sufficiently agitated to release the charge stored in them (Khare *et al* 1994c). The amount and sign of charge injected depends on the relative work function of the metal–polymer interface, i.e. the difference in energy between the Fermi level in metal and the bottom of the conduction band in the insulator. Therefore, the TSC parameters are changed when the electrode forming material is changed. It also seems possible that the dipolar peak either gets masked by the space charge peak or its contribution to the total polarization is very small (Khare *et al* 1994a).

The absence of peak at 60°C in Al–Sn and Al–Pb combinations may be due to oxidation of Pb and Sn metal electrodes. The ethoxy group being weakly electronegative and the oxide layer electropositive, will neutralize each other's effects to some extent. It is probably for this reason that in these two particular electrode combinations, the peak at 60°C is suppressed and only small humps are observed.

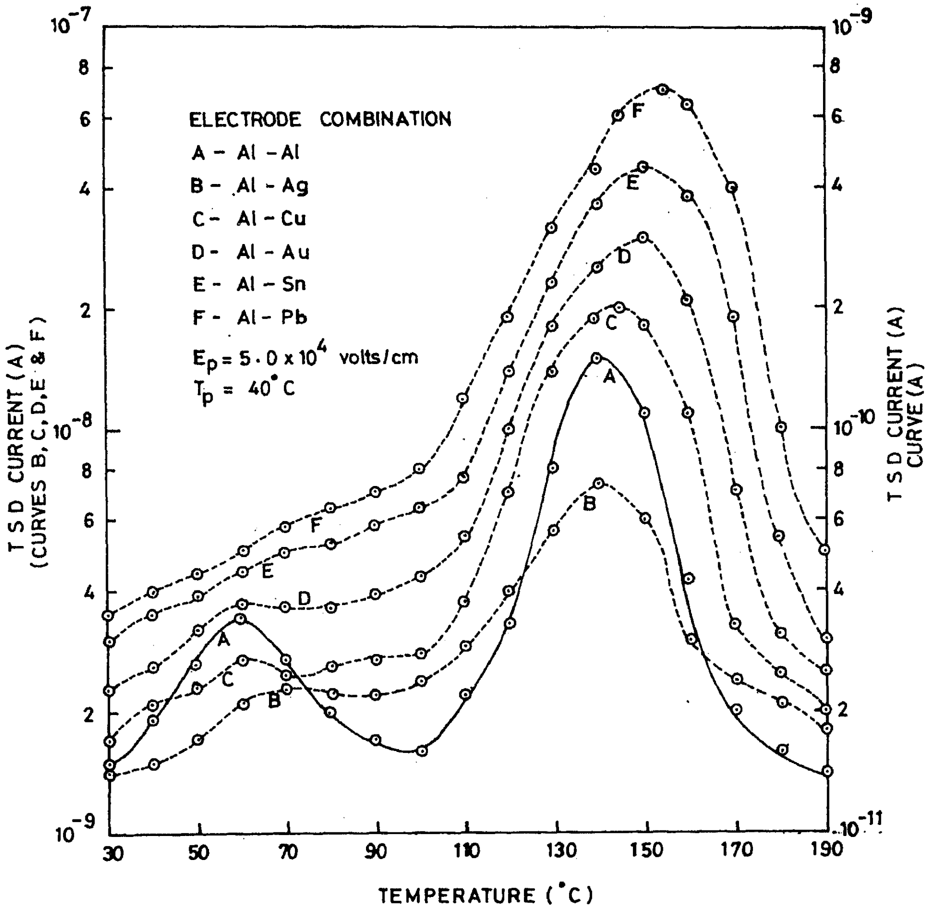

**Figure 1.** Effect of electrode materials on thermally stimulated current for ethyl cellulose samples with polarizing field $E_p = 5{\cdot}0 \times 10^4$ V/cm at polarizing temperature $T_p = 40$°C.

In wide gap insulators and polymers with $\pi$-electrons, intrinsic carrier generation is not possible. Charge transfer from the metal depends on the electron levels in which the carriers shift freely under the influence of the applied field. The energy on this level may be given by (Baessler 1972)

$$E_b = E_g = (I_g - p^+) - (A_c + p^-) = I_c - A_c \, , \qquad (1)$$

where $I_g$ is the ionization energy, $A_c$ the electron affinity, $p^+$ and $p^-$ are the polarization energies and $I_c$ the ionization energy of a molecule of the dielectric. The observed relation between the current and voltage points to a conduction mechanism in which the charge carriers are released by thermal activation over a coulombic potential barrier that is decreased by the electric field. The potential barrier can be one of the two types; (i) barrier between electrodes and dielectric taking the classic image force into consideration (Schottky emission), and (ii) barriers due to trapping centres in the dielectric (Poole–Frenkel effect). Taylor and Lewis (1971) assumed a more generalized form of the potential barrier rather than a Coulombic barrier usually employed in treatment of the RS effect. They concluded that the potential barrier chosen is referred to the cathode–dielectric interface and probably is determined by a space-charge layer in the dielectric. Such space-charge layers are charged up by the absorption current. In the present case, $I$–$E^{1/2}$ plots may be interpreted in terms of Richardson–Schottky (RS) field assisted thermionic injection of carriers from metal electrodes.

The primary source of charge carriers is the electrode contacts. Carriers are generated in the bulk on account of thermal ionization of impurities and absorbed water molecules. Nath and Kumar (1980) have shown injection of holes in cellulose acetate film. Hole injection results in depletion of layer of negative charges creating a field at the interface between the electrode and film surface. When two metals are brought in close contact, a potential difference of work function $\phi_2 - \phi_1$, is created between the two metals. The semi-insulating polymer differs from a metal, however, in that an electric field may exist within the interior of the semi insulator. For this reason the contact potential drop between the metal and the semi-insulator may take place within the material rather than at the contact interfaces. Along with the field, there may exist a depletion in the accumulation of charges in

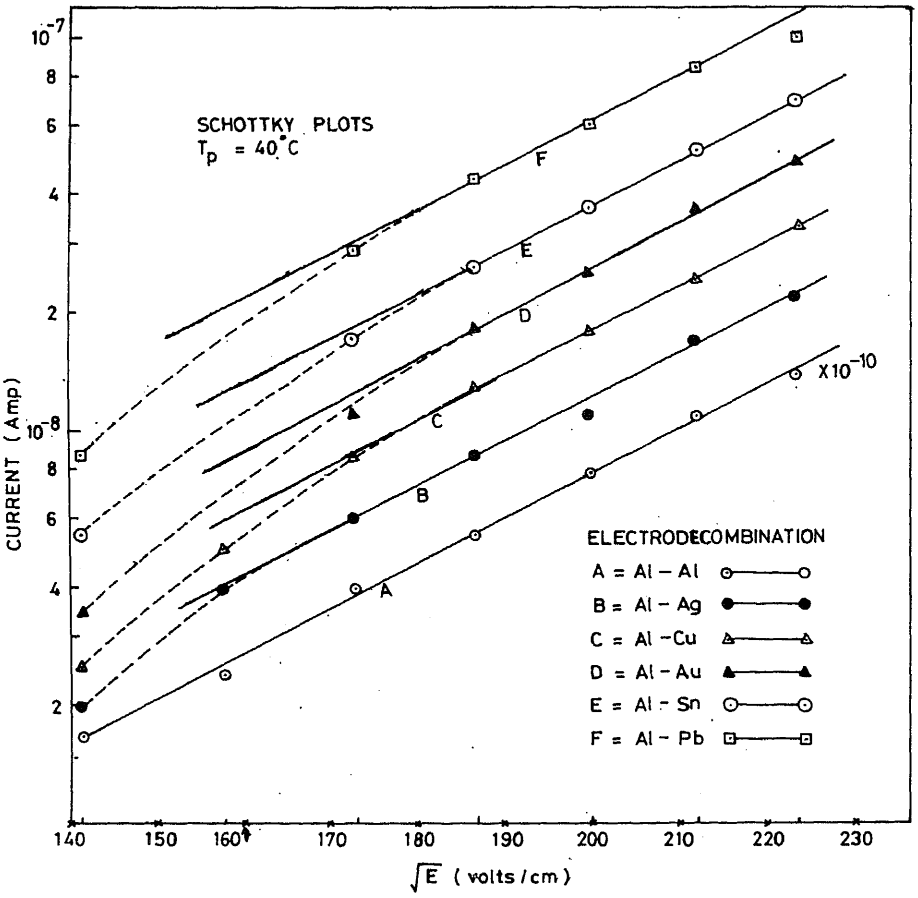

**Figure 2.** Log $I$ vs $\sqrt{E}$ plots (Schottky plots—similar and dissimilar electrode system).

the surface layers (Khare and Srivastava 1992b). The work function of the metals used for contacts is lower compared to that of the work function of the polymeric material which creates an accumulation layer at the interfaces and leaves charged donors in the bulk. This in turn creates fields at the interfaces of the metal–polymer system (Khare *et al* 1994d). Suppose an insulator has a large energy gap with its Fermi level located above the mid gap and there is no surface state, then after contact with a metal surface, the electron transfer at contact equalizes both Fermi levels. The barrier height depends on the relative values of metal work function and the electron affinity of the insulator (Takai *et al* 1975). The surface state (Wintle 1977) is one of the factors which affects injection phenomena. Donor-like surface states located between the conduction band and Fermi level, after contact tend to bend the band edge towards the Fermi level, making electron injection from the metal much easier. On the other hand, acceptor like surface states located between the valence band and Fermi level act as a stepping-stone for electrons injected from the valence band of the insulator to the metal, thus, enhancing hole injection (Shrivastava *et al* 1979). Electrons must overcome the potential barrier ($x$) given by

$$x^{-} = \phi - A_c ,$$

while holes are given by

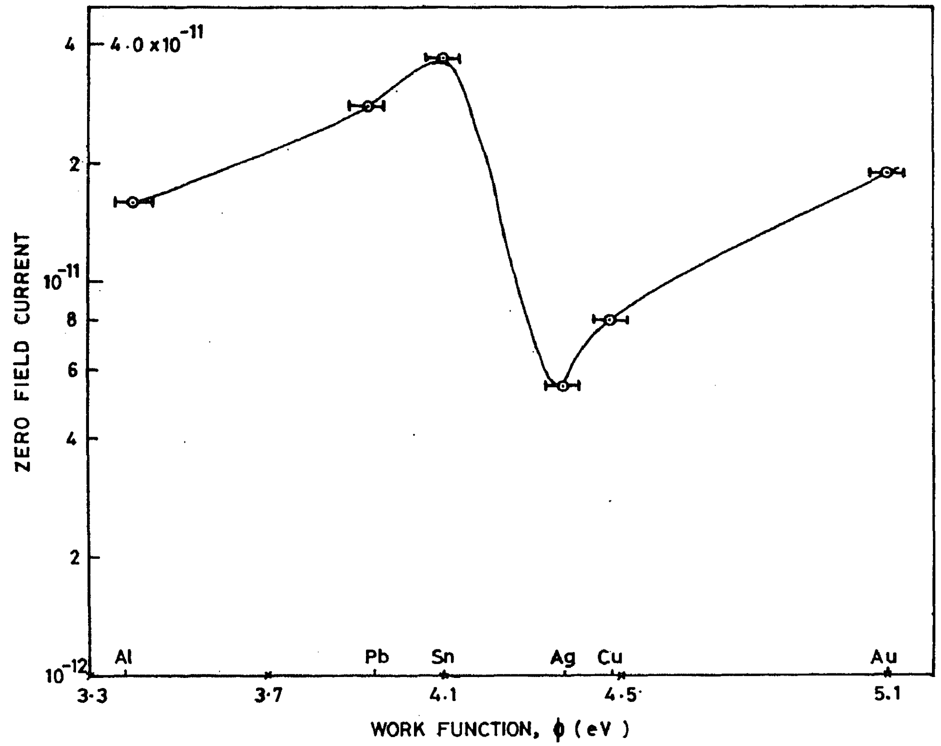

**Figure 3.** Zero field current vs metal work function for EC films.

**Table 1.** Depolarization kinetic data of electrode variation in ethyl cellulose films ($E_p = 5{\cdot}0 \times 10^4$ volts/cm, $T_p = 40$°C).

| Electrode combination | Peak temperature (°C) | Peak current ($A$) | Activation energy (eV) | Relaxation time $\tau_0$ (sec) | Charge released $Q$ (Coul) |
|---|---|---|---|---|---|
| Al–Al | 60 | $3{\cdot}2 \times 10^{-11}$ | 0·18 | $4{\cdot}789 \times 10^{-11}$ | $6{\cdot}222 \times 10^{-11}$ |
| | 140 | $1{\cdot}5 \times 10^{-10}$ | 0·32 | $8{\cdot}698 \times 10^{-10}$ | $1{\cdot}576 \times 10^{-10}$ |
| Al–Ag | 140 | $7{\cdot}2 \times 10^{-9}$ | 0·48 | $9{\cdot}978 \times 10^{-10}$ | $3{\cdot}321 \times 10^{-9}$ |
| Al–Cu | 145 | $2{\cdot}0 \times 10^{-8}$ | 0·52 | $3{\cdot}957 \times 10^{-9}$ | $2{\cdot}234 \times 10^{-8}$ |
| Al–Au | 150 | $3{\cdot}0 \times 10^{-8}$ | 0·56 | $6{\cdot}998 \times 10^{-9}$ | $8{\cdot}768 \times 10^{-8}$ |

$$x^{+} = I_{c} - \phi , \tag{2}$$

where $\phi$ is the metal work function, $A_c$ the electron affinity and $I_c$ the ionization energy of a molecule of the dielectric.

In the present case the magnitude of TSC and steady state current was found to be higher in dissimilar electrode than similar electrode combinations. This shows the effect of materials of electrodes on the current of the sample sandwiched between them. The observations are consistent with the proposed R–S mechanism in which the carriers are injected over the field-dependent polymer–electrode interfacial barrier. The emission current is described by Richardson's equation

$$J_0 = AT^2 \exp\left(-\frac{x}{kT}\right), \tag{3}$$

where $J_0$ is the current density, $T$ the absolute temperature, $k$ the Boltzmann's constant and $A$ a constant.

The classical RS effect predicts a current–voltage relationship of the form

$$J = AT^2 \exp\left(-\frac{x}{kT}\right) \exp(\beta_s V^{1/2}) , \tag{4}$$

with

$$\beta_s = \frac{e}{kT}\left(\frac{e}{4\pi\,\varepsilon\,\varepsilon_0\,d}\right)^{1/2}, \tag{5}$$

where $d$ is the film thickness, $\varepsilon$ the dielectric constant, $\varepsilon_0$ the permittivity of the free space and $e$ the electronic charge. For zero field, (4) reduces to (3) and the current density depends on the potential barrier at a constant temperature. The zero-field current density ($J_0$) was extrapolated by extending the linear portion of the $I$–$E^{1/2}$ plot backwards to meet the current axis. The values of $J_0$ vs metal work function have been plotted in figure 3. The negative slope of the line when EC makes contact with Ag which signifies that the electron injection decreases for Al–Ag electrode combination and so the zero field current decreases. The possible meaning that may be attached to the positively sloped line which is obtained when ethyl cellulose will be in contact with copper, tin, lead and gold is that, hole injection into the polymer film increases with the increase in metal function (Khare 1994) and hence zero field current also increases.

## 4. Conclusion

Thermally stimulated current and conduction current of ethyl cellulose films reveal a strong dependence on the electrode forming material which is the source of charge carriers responsible for conduction and observed polarization of the polymer.

## Acknowledgement

The significant help provided by Mr Arun Kumar Khare, LIG-5, Shakun Sadan, New Anand Nagar, Adhartal, Jabalpur, is gratefully acknowledged.

## References

Baessler H 1972 *Kunststoffe* **62** 115

Bucci C, Fieschi R and Guidi G 1966 *Phys. Rev.* **148** 816

Dubey V, Khare P and Saraf K K 1990 *Indian J. Pure & Appl. Phys.* **28** 579

Garlick G F J and Gibson A P 1948 *Proc. Phys. Soc.* **60** 574

Gutman F and Lyons L E 1967 *Organic semiconductors* (New York: Wiley)

Hino T and Yamashita K 1974 *Jpn J. Appl. Phys.* **13** 1015

Khare P K 1994 *Indian J. Pure & Appl. Phys.* **32** 160

Khare P K and Srivastava A P 1992a *Indian J. Pure & Appl. Phys.* **30** 102, 131

Khare P K and Srivastava A P 1992b *Thin Solid Films* **208** 233

Khare P K and Srivastava A P 1993 *Indian J. Pure & Appl. Phys.* **31** 126

Khare P K, Surinder P and Srivastava A P 1992 *Indian J. Pure & Appl. Phys.* **30** 165

Khare P K, Gaur M S, Alka Bajpai, Pandey R K and Srivastava A P 1993 *Indian J. Pure & Appl. Phys.* **31** 326

Khare P K, Vishwakarma H L and Srivastava A P 1994a *Indian J. Phys.* **A68** 571

Khare P K, Gaur M S and Srivastava A P 1994b *Indian J. Pure & Appl. Phys.* **32** 14

Khare P K, Keller J M, Gaur M S, Ranjeet Singh and Datt S C 1994c *Polym. Int.* **35** 337

Khare P K, Chandok R S, Dubey Neeraj and Srivastava A P 1994d *Polym. Int.* **35** 153

Khare P K, Keller J M, Gaur M S, Ranjeet Singh and Datt S C 1996 *Polym. Int.* **39** 303

Koton J E 1968 *Organic semiconducting polymers* (New York: Marcel Dekker)

Kryozewski M 1975 *J. Polym. Sci. Polym. Phys.* **50** 359

Lampert M A and Mark P 1970 *Current injection in solids* (New York: Academic Press)

Nath R and Kumar A 1980 *Phys. Status Solidi* **a61** 301

Pulfrey D L 1972 *J. Phys. D* **5** 647

Shatzkes M 1978 *J. Appl. Phys.* **49** 4868

Shrivastava S K, Ranade J D and Srivastava A P 1979 *Jpn J. Appl. Phys.* **18** 2303

Shrivastava S K, Ranade J D and Srivastava A P 1981 *Polymer* **22** 1645

Singh R, Datt S C, Keller J M, Khare P K and Chandok R S 1991 *IEEE* 563

Takai Y, Osawa T, Chikao K, Mizutani T and Ieda M 1975 *Jpn J. Appl. Phys.* **10** 473

Taylor D M and Lewis T J 1971 *J. Phys. D: Appl. Phys.* **4** 1346

Van Turnhout J 1975 *Thermally stimulated discharge of polymer electrets* (Amsterdam: Elsevier)

Wintle H J 1974 *J. Polym. Sci. Polym. Phys.* **12** 2135

Wintle H J 1977 *IEEE Trans. Electr. Insul.* **EI-12** 97

# Electrical properties of zirconium diselenide single crystals grown by iodine transport method

**S G PATEL*, M K AGARWAL, N M BATRA[†] and D LAKSHMINARAYANA[‡]**

Department of Physics, [†]Department of Materials Science, [‡]Department of Electronics, Sardar Patel University, Vallabh Vidyanagar 388 120, India

MS received 26 August 1997; revised 3 April 1998

**Abstract. Single crystals of zirconium diselenide ($ZrSe_2$) were grown by chemical vapour transport method using iodine as the transporting agent. The crystals were found to exhibit metallic behaviour in the temperature range 77–300 K and semiconducting nature in 300–443 K range. The measurements of thermoelectric power and conductivity enabled the determination of both carrier mobility and carrier concentration. The variation of carrier mobility and carrier concentration with temperature indicates the presence of deep trapping centres and their reduction with temperature in these crystals.**

**Keywords. Zirconium diselenide; chemical vapour transport; electrical conductivity; thermoelectric power; trapping centres.**

## 1. Introduction

Zirconium diselenide ($ZrSe_2$) crystallizes in a cadmium iodide type structure, which is characterized by strong bonding within layers and relatively weak Van der Waal's bonding between adjacent sheets of layers. The structure is markedly anisotropic giving rise to an extended growth perpendicular to c-axis of the hexagonal crystals. These crystals have interesting electrical (Lee *et al* 1969a), and semiconducting (Lee *et al* 1969b) properties. They also exhibit some interesting switching and memory effects (Lee *et al* 1969a). A possibility of their use in solid state solar cell has also been predicted (Tributsch 1980).

The data concerning electrical properties of $ZrSe_2$ in the literature are very scarce and there have been no recent reports. It has been reported that $ZrSe_2$ grown by granular zirconium has a metallic nature whereas samples prepared from powdered zirconium show a semiconducting behaviour (Onuki *et al* 1982). They have also shown that in the temperature range 50–300 K the electrical resistivity of layered $ZrSe_2$ is proportional to $T^2$. It has also been reported that samples with higher stoichiometry exhibit semiconducting behaviour while the less stoichiometric compounds are metallic (Deniard *et al* 1987). The normal semiconducting behaviour of $ZrSe_2$ has also been reported (Zheng *et al* 1989) in electrical anisotropic studies in the temperature range 100–800 K. Looking at the anomaly in the resistivity behaviour of samples in the low and high temperature regions, we have carried out these measurements in both the ranges of temperatures. Moreover, the fact is $ZrSe_2$ is expected to have highly anisotropic electrical properties. We have also concentrated on this aspect in the resistivity measurements. In this paper, we, therefore, report the growth, characterization, measurements of d.c. resistivity, thermoelectric power, mobility and anisotropy in electrical resistivity in different temperature ranges.

## 2. Experimental

### 2.1 *Growth of $ZrSe_2$ single crystals*

Synthesis of zirconium diselenide was first reported by Van Arkel (1924). Later, Hahn and Ness (1957, 1959), McTaggari and Wadsley (1958), Greenway and Nitsche (1965), Gleizes and Jeannin (1970), Remmington *et al* (1972), Lucovsky *et al* (1973) and Whitehouse *et al* (1973) have grown this compound by halogen transport methods. However, in the usual vapour growth experiments the quartz ampoule containing the charge is placed in the furnace in such a way that its bottom is directly in contact with the furnace wall while the upper portion is projected inside the furnace tube. This creates an uneven temperature gradient in the vertical direction leading to the introduction of defects into the grown crystals. In order to avoid this temperature gradient, arrangements were made to keep the quartz ampoule (along with the charge) coaxially within the furnace tube in the present investigation. The length of the quartz ampoule was about 250 mm with an inner diameter of 20 mm. The hot and cold junctions of the furnace were maintained at 1123 K and 1073 K, respectively. Iodine was used as a transporting agent and large sized single crystals of $ZrSe_2$ were obtained over a growth period of 500 h at the colder end of the ampoule. The crystals could easily be cleaved along the basal (0001) plane. The structural characterization and the compositional analysis were made by X-ray diffraction and energy dispersive analysis of X-rays (EDAX), respectively.

---

*Author for correspondence

### 2.2 *Electrical resistivity measurements*

D.C. electrical resistivity measurements were performed on the freshly cleaved (0001) basal planes in a direction perpendicular to c-axis. Low temperature resistivity measurements along the basal planes ($\rho_{\parallel}$) in the temperature range 77–300 K were made in a specially designed cryostat LN-DP manufactured by Scientific Solutions, Mumbai. Electrical contacts were made using proper solder/silver paste. Four point contacts were used to obtain the resistivity. For resistivity ($\rho_{\parallel}$) measurements in the temperature range 303–443 K a four-probe set up manufactured by Scientific Equipments, Roorkee was used. Resistivity measurements normal to the basal plane ($\rho_{\perp}$) were carried out on an experimental set up designed and prepared by the University Science and Instrumentation Centre (USIC), Sardar Patel University, Vallabh Vidyanagar. Starting from room temperature (303 K), the temperature of the sample was increased slowly in steps of 10 K until a temperature of 443 K was reached. At each step the corresponding value of resistivity was evaluated.

### 2.3 *Thermoelectric power measurements*

The thermoelectric power (TEP) measurements were carried out using the thermopower ($S$) measurements set up TPSS-200 developed by Scientific Solutions, Mumbai. In all the measurements $\Delta T$ was kept as 4 K and the TEP ($S_{\parallel}$) measurements were carried out in the temperature range 313–443 K. Due to experimental limitations, TEP ($S_{\perp}$) measurements normal to the basal plane i.e. parallel to c-axis, could not be made.

## 3. Experimental

### 3.1 *Structural characterization*

Figure 1 shows the zirconium diselenide ($ZrSe_2$) single crystals obtained in the present investigation. Figure 2 shows an a-axis oscillation photograph corresponding to the cleaved front face of $ZrSe_2$ crystals taken with CuK$\alpha$ radiation employing a conventional X-ray tube with a camera radius of 3 cm and collimeter aperture of 0·1 cm. The crystal was oscillated about the a-axis between 25–40°. The a-axis oscillation photograph shows rows of constant $h, k$ and varying $l$. The presence of spots along the rows clearly indicates that the grown crystals have an ordered single crystal nature. The values of lattice parameters obtained from the X-ray diffraction are found to be $a = 3{\cdot}772$ Å and $c = 6{\cdot}122$ Å clearly matching with the reported values (Whitehouse *et al* 1973) for the compound $ZrSe_{1{\cdot}96 \pm 0{\cdot}3}$. The composition of the crystals as obtained by EDAX correspond to $ZrSe_{1{\cdot}96}$.

### 3.2 *Variation of resistivity with temperature*

Results of low temperature (77–300 K) resistivity ($\rho_{\parallel}$) measurements on a representative sample are shown in figure 3. It is seen that resistivity increases with increase in temperature and is found to be proportional to $T^2$ similar to $TiS_2$ and $ZrSe_2$ as reported by Onuki *et al* (1982).

In the temperature range 303–443 K it is seen that

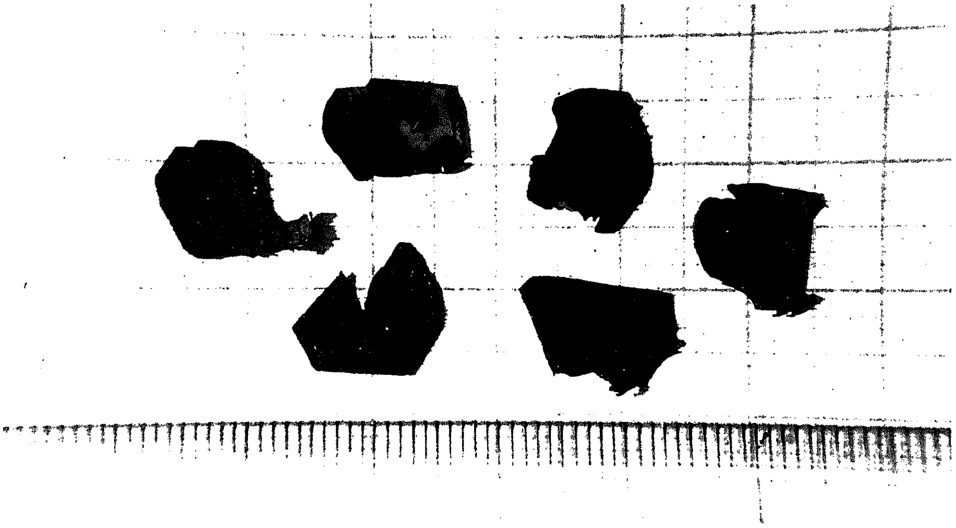

**Figure 1.** Single crystals of $ZrSe_2$.

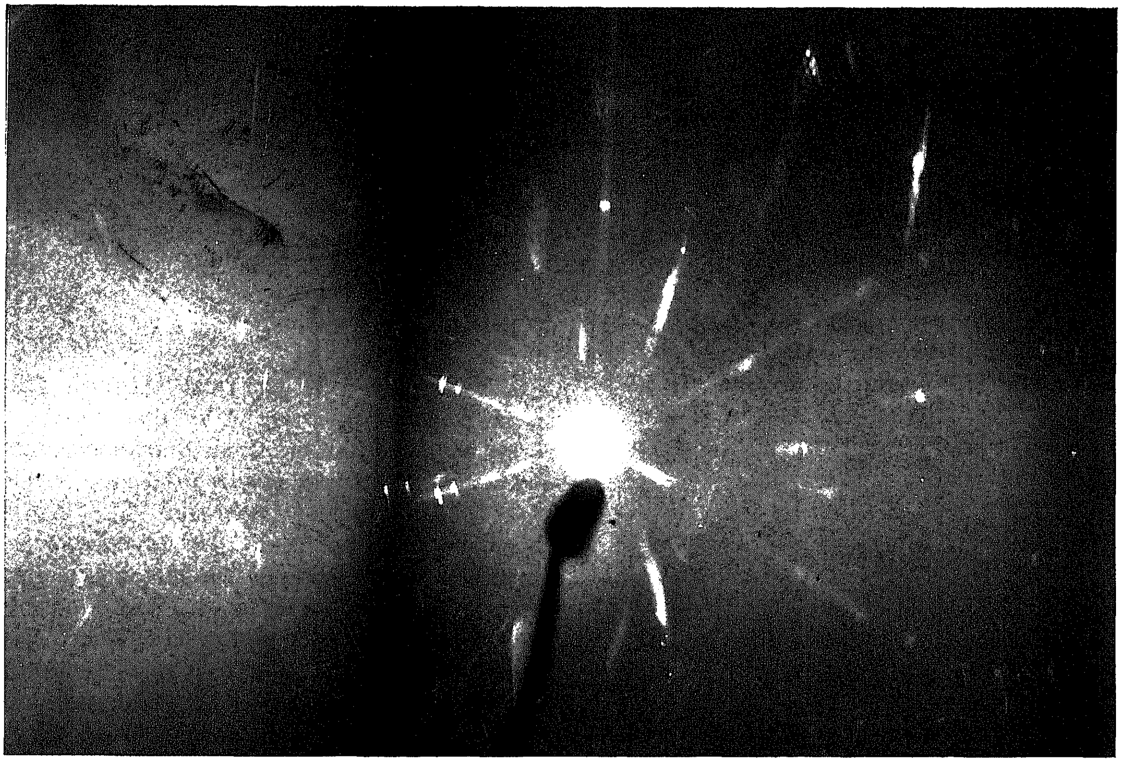

**Figure 2.** X-ray oscillation photograph of $ZrSe_2$ single crystal.

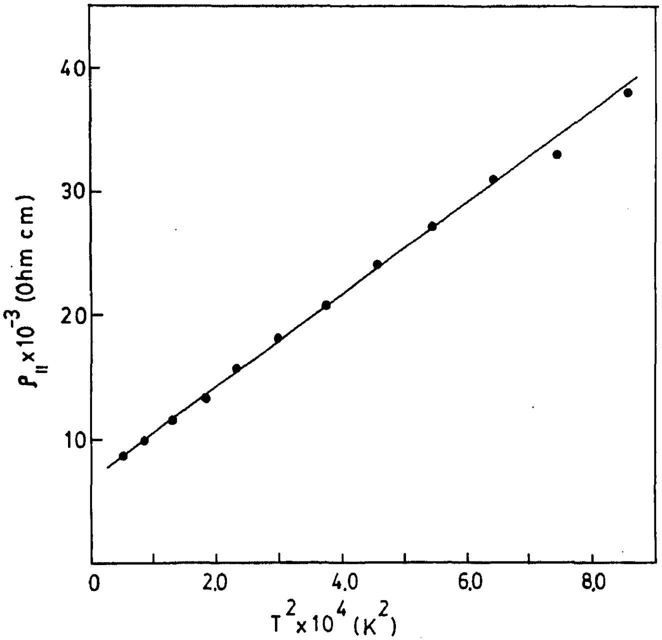

**Figure 3.** Variation of resistivity with square of temperature.

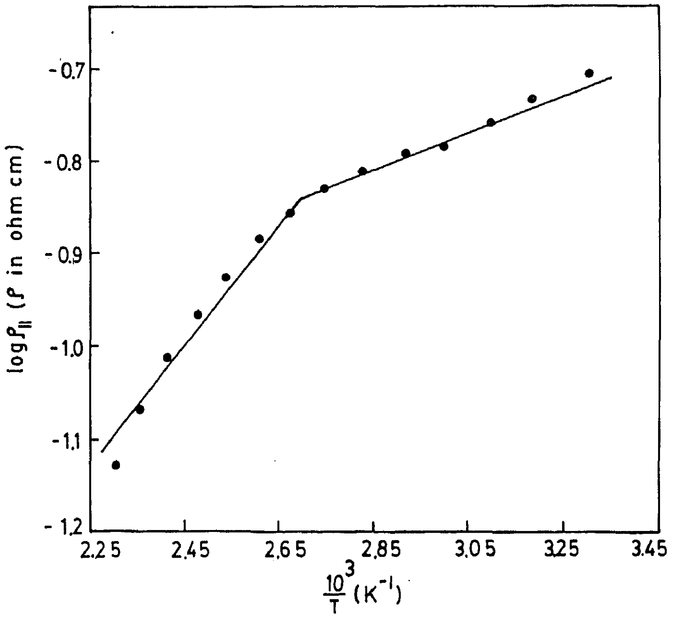

**Figure 4.** Variation of resistivity with reciprocal of temperature.

the resistivity decreases with an increase in temperature showing a semiconducting behaviour. The activation energies obtained from the graph (figure 4) are 0·0587 eV in the temperature range 303–393 K and 0·187 eV in the temperature range 393–443 K.

### 3.3 *Variation of electrical resistivity anisotropy with temperature*

Zheng *et al* (1989) measured anisotropy in the electrical resistivity ($\rho_{\perp}/\rho_{\parallel}$), in the temperature range 100–300 K.

In our investigation anisotropy measurements have been carried out in the temperature range 303–443 K. It is seen in figure 5 that the anisotropy ($\rho_\perp/\rho_\parallel$) ratio increases with increase in temperature. This variation of anisotropy with temperature shows an identical behaviour to that reported by Zheng *et al* (1989).

### 3.4 *Variation of TEP with temperature*

The polarity of the thermally generated voltage at the hot end was positive indicating that the crystals are *n*-type in nature. The TEP was found to increase linearly with temperature. The TEP ($S=S_\parallel$) has been used to evaluate the carrier mobility using the relation given by Lee *et al* (1969b):

$$\mathrm{TEP}=S=-\frac{k}{e}\left\{\frac{E_a}{kT}+A\right\},$$

or

$$S=-\frac{k}{e}\left\{A+\ln[2(2m_e^*kT)^{3/2}/nh^3]\right\}, \qquad (1)$$

where $A$ is the thermoelectric factor, $n$ the electron density, $h$ the Planck constant and $m_e^*$ the effective mass of electron. The above equation after the substitution of various constants and taking $A=1{\cdot}5$ for ionized impurity scattering simplifies to

$$\log n=(3/2)\log T-0{\cdot}005S+15{\cdot}719\,. \qquad (2)$$

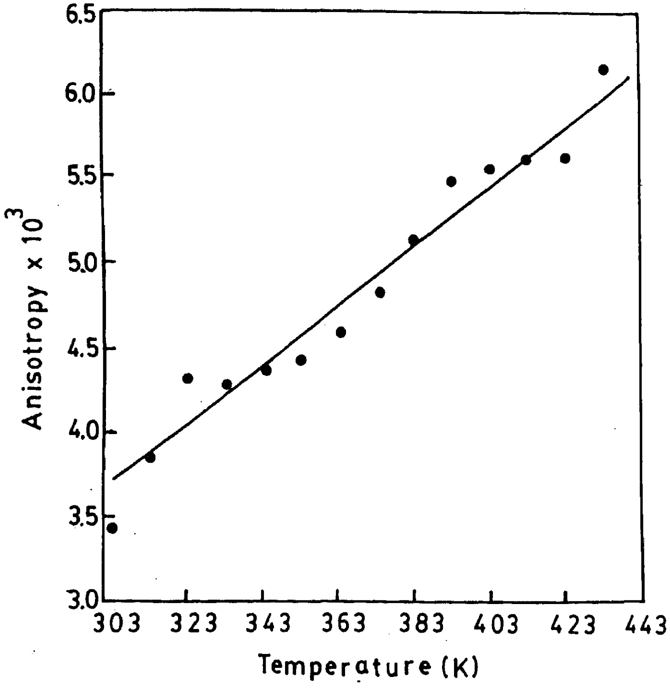

**Figure 5.** Variation of anisotropy with temperature.

The electron density has been evaluated by using the above relation. The mobility, $\mu$, of the charge carriers is determined from the relation

$$\mu=\frac{\sigma}{ne}, \qquad (3)$$

where $n$ is the carrier concentration, $e$ the charge of electron and $\sigma$ the electrical conductivity.

## 4. Discussion

The $T^2$ dependence of electrical resistivity can be attributed to carrier scattering rather than carrier activation. However, due to experimental limitations the scattering and degeneracy could not be studied in detail in this range (77–300 K) of temperature. The high value of resistivity in the perpendicular direction suggests that conduction of electron in the direction normal to the layer is very little. Further, the anisotropic behaviour and its variation with temperature clearly shows that electronic conduction in $\mathrm{ZrSe_2}$ is highly anisotropic. This large anisotropy in electronic behaviour may be attributed to the sufficiently larger effective mass anisotropy $m_\parallel^*$ being 0·43 whereas $m_\perp^*$ being 7·00, where ∥ and ⊥ denote, respectively, parallel and perpendicular to the layers of $\mathrm{ZrSe_2}$ single crystals (Isomaki *et al* 1979). The high values of resistivity and large anisotropy further suggest that electron states in $\mathrm{ZrSe_2}$ is two dimensional in contrast to a three dimensional behaviour seen in GaSe and SnSe. The low values of activation energy obtained from figure 4 can be attributed to the high carrier concentration density which gives rise to energy levels very close to the conduction band. These carriers will also be scattered by various centres or regions such as grain boundaries, dislocations, surface states etc in addition to the normally observed scattering modes, viz. ionized impurity, lattice or phonon, piezoelectric etc. The positive temperature dependence of mobility suggests that ionized impurity scattering might be the dominant scattering mechanism in these crystals in the observed temperature range. From the slope of temperature dependent mobility graph (figure 6), it is possible to obtain some qualitative idea about the scattering mode. Since all scattering processes are likely to follow the relation $\mu\propto T^x$, the magnitude and sign of x will determine the scattering mode. In the present case the value of x from figure 6 comes to about 0·05 and is positive. The theoretical value of x for ionized impurity acting as a single mode of scattering is 3/2. The deviation in the observed value seems to be due to the superimposition of the ionized impurity scattering with some of the above mentioned scattering processes. The observed range of temperature i.e. 303–443 K, corresponds to the extrinsic/impurity range only as seen from the low values of conductivity activation energy. Also, the carrier concen-

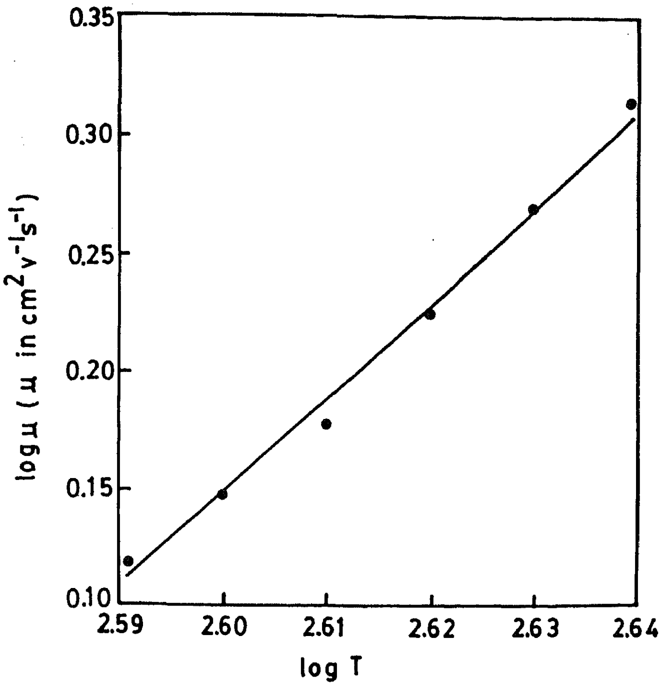

**Figure 6.** Variation of mobility with temperature.

tration can be expressed as

$$n \approx \exp\left(\frac{En}{kT}\right), \tag{4}$$

where $En$ is the carrier activation energy of the $n$-type $ZrSe_2$ single crystal. The above equation predicts a linear relation between $\log n$ and $1/T$ as observed in figure 7. The carrier activation energy estimated from the slope, was found to be 0·29 eV. Since this value is much less than half the reported value of electrical band gap of 1·22 eV (Murray *et al* 1972), the presence of deep donor like levels is possible in this material. Hence, heating in the lower temperature range reduces the number of deep trapping centres and thereby increasing the number of free carriers and carrier mobility. The mobility may reduce only at still higher temperatures where the scattering due to lattice thermal vibration dominates.

## 5. Conclusions

Single crystals of zirconium diselenide could be grown by chemical vapour transport using iodine as the transporting agent. These crystals exhibited metallic behaviour in the temperature range 77–300 K and semiconducting nature in the temperature range 300–443 K. The positive temperature dependence of carrier mobility suggested that ionized impurity scattering might be the dominant scattering mechanism in these crystals. The variation of carrier mobility and carrier concentration with temperature in the semiconducting range indicates the presence of deep trapping centres.

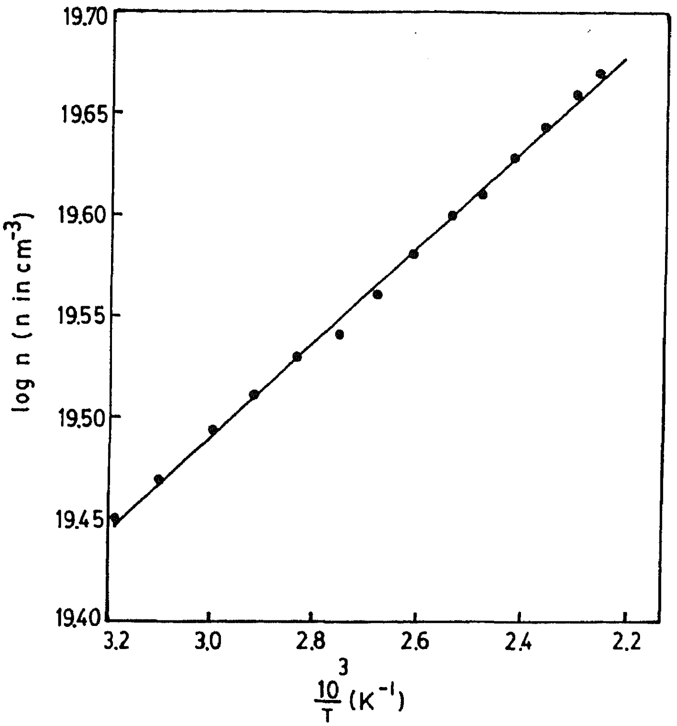

**Figure 7.** Variation of carrier concentration with reciprocal of temperature.

## References

Deniard P, Chevalier P, Trichet L and Chabre Y 1987 *Solid State Commun.* **64** 175

Gleizes A and Jeannin Y 1970 *Solid State Chem.* **1** 180

Greenway D L and Nitsche R 1965 *J. Phys. Chem. Solids* **26** 1445

Hahn H and Ness P 1957 *Naturwiss.* **44** 534

Hahn H and Ness P 1959 *Z. Anorg. Allg. Chem.* **302** 37

Isomaki H, Von Boehm J and Krusivs P 1979 *J. Phys.* **C12** 3239

Lee P A, Said G and Devis R 1969a *Solid State Commun.* **7** 1359

Lee P A, Said G, Devis R and Lim T 1969b *J. Phys. Chem. Solids* **30** 2719

Lucovsky G, White R M, Benda J A and Revelli J F 1973 *Phys. Rev.* **B7** 3859

McTaggari K F and Wadsley A D 1958 *Aust. J. Chem.* **11** 445

Murray R B, Bromley R A and Yoffe A D 1972 *J. Phys.* **C5** 746

Onuki Y, Inada R and Tanuma S 1982 *J. Phys. Soc. Jap.* **51** 1223

Remmington H P B, Tanner B K and Balchin A A 1972 *J. Cryst. Growth* **15** 51

Tributsch H 1980 *Appl. Phys.* **23** 61

Van Arkel A E 1924 *Physica* **4** 286

Whitehouse C R, Remmington H P B and Balchin A A 1973 *Phys. Status Solidi (a)* **18** 623

Zheng X, Kuriyaki H and Hirakawa K 1989 *J. Phys. Soc. Jap.* **58** 622

# Dielectric properties and electrical conduction in yttrium iron garnet (YIG)

**LALITHA SIRDESHMUKH*, K KRISHNA KUMAR, S BAL LAXMAN, A RAMA KRISHNA and G SATHAIAH**

Department of Physics, Kakatiya University, Warangal 506 009, India

MS received 28 April 1997; revised 5 March 1998

**Abstract.** **The dielectric properties (dielectric constant and loss) of a single crystal of yttrium iron garnet ($Y_3Fe_5O_{12}$) were measured in the temperature range 77–725 K and in the frequency range 100 Hz–1 MHz. AC conductivity was derived from dielectric constant and loss. DC conductivity was measured in the temperature range 30–725 K. Thermoelectric power (TEP) was measured from 77–800 K. On the basis of the results, conduction in this garnet is interpreted as due to small polarons. The nature of conduction at different temperature ranges is discussed in the light of existing reports on defect formation.**

**Keywords.** **Yttrium iron garnet; dielectric constant; conductivity; polaron conduction.**

## 1. Introduction

Yttrium iron garnet (YIG) exhibits ferrimagnetism with low hysteresis loss and high resistivity at room temperature. Because of this, it is of technical importance and finds use in radio-electronics and UHF technology (Krupichka 1976). Hence the study of magnetic and electrical properties is important and useful.

The magnetic properties of YIG have been investigated by many workers (Epstein and Frackiewicz 1959; Wurlitzer and Richter 1970; Wurlitzer 1987; Bush 1988; Chukalkin *et al* 1989). There are some reports on studies on electrical conductivity (Elwell and Dixon 1968; Fontana and Epstein 1971; Metselaar and Larsen 1974; Lal *et al* 1982; Petrov *et al* 1986). There are only a few reports on dielectric properties. Hirakata *et al* (1991) reported the dielectric behaviour at liquid nitrogen temperatures but the dielectric constant was not clearly indicated. Hofmeister and Campbell (1992) determined low- and high-frequency dielectric constants from infrared reflectivity measurements and indicated that the data by direct measurement is not available for a pure YIG single crystal.

From resistivity and thermoelectric power measurements on $Hf^+$-doped YIG in the range 500–1000 K, Elwell and Dixon (1968) concluded that the conduction should be described by localized model rather than the band model. Studies on electrical conduction in silicon-doped YIG by Fontana and Epstein (1971) in the temperature range 20–200°C is interpreted as arising from localized hopping of electron amongst four $Fe^{3+}$ cation sites around $Si^{4+}$ impurity sites.

From DC conductivity and thermoelectric power measurements, Metselaar and Larsen (1974) indicate the possibility of *p*-type conduction in YIG in the high temperature range 1200–1700 K. Results of Lal *et al* (1982) and Petrov *et al* (1986) in high temperature range $>600$ K and $>1270$ K, respectively support conduction via thermally-activated hopping of *p*-type charge carriers.

As evident from literature survey, while dielectric properties have been measured only in the liquid nitrogen range of temperature, resistivity measurements have been done on a $Hf^{4+}$-doped sample at higher temperature beyond 500 K. Electrical conductivity studies have been made up to 475 K on a polycrystalline sample. The authors have neither come across a detailed investigation of dielectric properties over wide range of temperatures and frequencies nor conductivity measurements on a single crystal sample.

It is well-known that the measurement of dielectric loss is a powerful method to detect relaxation due to formation of dipoles. AC conductivity in a wide range of frequencies combined with DC conductivity and thermoelectric power measurements helps to understand the conduction mechanism and identify the charge carriers responsible for conduction.

Based on the above-mentioned facts, the measurements of dielectric constant and loss, DC conductivity and thermoelectric power have been carried out on a single crystal of YIG. The results are discussed to understand the conduction mechanism.

## 2. Experimental

All the measurements were carried out on a flux-grown single crystal of YIG with parallel (111) faces. The sample was well polished and was in the form of a semi-circular disk of dimensions 0·67 cm$^2$ × 0·0615 cm.

---

*Author for correspondence

In the low-temperature region, capacitance and loss were recorded using a fully automated computer-controlled CGA-83 transformer ratio arm bridge. The bridge was capable of measurement in three-terminal configuration. The accuracy of capacitance and loss is 0·1% and 1%, respectively. The measurements were carried out at 17 frequencies in the range 10–100 kHz at temperatures from 77 K to 340 K with an interval of 5 K and with an accuracy of 0·1 K.

The high-temperature dielectric measurements were carried out using a Hewlett-Packard 4192 A impedance analyzer in conjunction with a laboratory-designed cell, in two-terminal method. The sample was coated with silver paint to ensure good electrical contact. Low-temperature resistivity measurements were carried out using an automated temperature controller and a Keithley digital electrometer. A Keithley electrometer (model 610 C) was used for high-temperature DC conductivity measurements with an applied voltage of 3 volts.

For low-temperature resistivity and thermoelectric power measurements, laboratory-built sample holders were used with a closed cycle helium cryo-refrigerator as the cooling device. The temperature gradient was controlled by using a Lakeshore temperature controller with an accuracy in temperature of 0·1 K. High-temperature thermoelectric power measurements were carried out using differential method and a Keithley nano-voltmeter for recording the data.

## 3. Results

### 3.1 *Dielectric properties and conductivity*

3.1a *Low-temperature measurements*: The low-temperature data was recorded as capacitance $C(\omega)$ and $G(\omega)$, $\omega$ as a function of temperature, where $G(\omega)$ is conductance. The variations are to be treated as relative variations in dielectric constant and loss. The temperature variation of capacitance and loss at a few selected frequencies are shown in figures 1 and 2, respectively. The change in capacitance with frequency from 1–100 kHz is only 1% in low-temperature range and 2% around 340 K. The variation with temperature is slow with distinct peaks around 130 K, 160 K and a sharp increase at 280 K. This increase may be attributed to a large increase in ionic contribution to dielectric constant. Hirakata *et al* (1991) observed some anomalies in the real part of the dielectric constant and loss around 130 K. They believe that these changes reflect the changes observed in the first-order magnetoelectric effect experiments of Kita *et al* (1988). Kita *et al* (1988) attributed the changes to some sort of phase transition, leading to a non-centrosymmetric structure below 125 K.

Such a transformation could not be detected by X-ray and Mössbauer studies (Hirakata *et al* 1991). According to Hirakata *et al* (1991), the lattice strain due to the structural transition is so small that it could not be detected by X-ray, electron diffraction, Mössbauer and dielectric measurements. However, they support the existence of some sort of phase transformation, on the basis of the fact that the second-order magnetoelectric effect also shows a sharp decrease around 125 K (Takano *et al* 1991).

The variation of loss ($G/\omega$) with temperature is shown in figure 2. The peaks around 130 K, 160 K and 285 K are the manifestation of the effects observed in magnetic dispersion curves due to the presence of Si$^{4+}$ in YIG (Wurlitzer and Richter 1970). Other studies on YIG such as magnetoelectric effect (Hirakata *et al* 1991) mentioned earlier and studies on magnetic effect by Torres *et al* (1993) indicate peaks around 130 K and 180 K. The effect is believed to be due to the electron transfer between Fe$^{2+}$ and Fe$^{3+}$ ions creating local order and induced anisotropy. The temperature at which large increase is observed i.e. 295 K corresponds to $\theta/2$ where

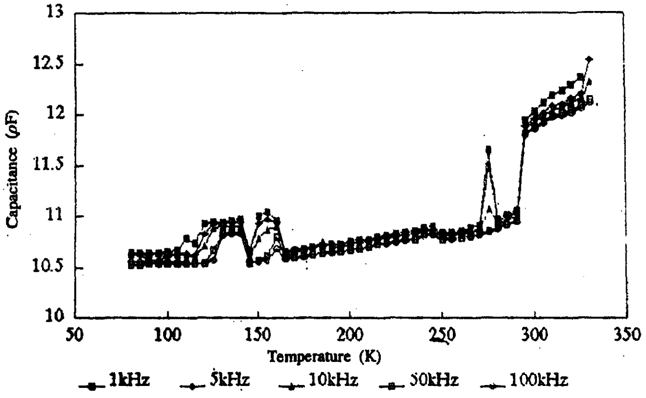

**Figure 1.** Variation of capacitance with temperature at different frequencies.

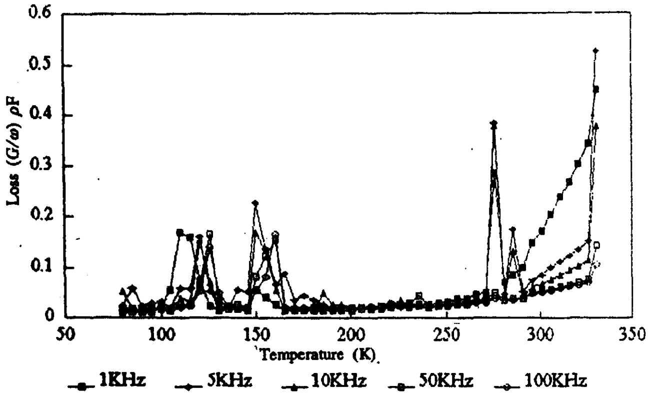

**Figure 2.** Variation of loss ($G/\omega$) with temperature at different frequencies.

$\theta$ (600 K) is Debye temperature (Landolt–Bornstein 1991).

AC conductivity $\sigma_{AC}$ is obtained from the data on dielectric constant ($\varepsilon$) and loss, $\tan\delta$ using the relation

$$\sigma_{AC} = \varepsilon\, \varepsilon_0\, \omega \tan\delta, \tag{1}$$

where $\varepsilon_0$ is the vacuum permittivity and $\omega$ the angular frequency. Figure 3 shows plots of AC conductivity against reciprocal temperature. For clarity, the regions of peaks in dielectric loss are not shown. It can be seen that conductivity is frequency-dependent and temperature-independent up to 250 K. The low-temperature DC conductivity (figure 4) is found to be independent of temperature. (Relative variation with temperature is to be noted and not the absolute value).

In the magnetic loss studies in YIG, Wurlitzer and Richter (1970) and Wurlitzer (1987) observed magnetic loss dispersion when a small amount of silicon is present as impurity which gets incorporated during growth or as dopant. This is attributed to the electron hopping between $Fe^{3+}$ and $Fe^{2+}$ ions. The crystal used for the present measurements is grown by flux in which divalent impurities Pb, Ca, $Fe^{2+}$ and F are present in addition to $Si^{4+}$ (Haussuhl 1976).

3.1b *High temperature measurements*: Initially, the dielectric constant and loss were measured as functions of frequency at room temperature. It is well established that for ionic crystals an increase in $\varepsilon$ and loss ($\tan\delta$) at low frequencies is observed for samples due to voids, dislocations and other defects. These spurious effects cease to influence the value beyond a certain frequency. The frequency-independent value is taken as static dielectric constant. For the sample of YIG used for measurements, the dielectric constant is almost frequency-independent beyond 50 kHz at room temperature. Values of the dielectric constant obtained in the present work and those reported by earlier workers are given in table 1. The values obtained from direct measurement are close to one another.

The variation of dielectric constant with temperature at different frequencies is shown in figure 5. It can be seen that large variations with temperature are observed at low frequencies. The variation of loss with temperature at different frequencies is shown in figure 6. The curves show well-defined peaks. The peaks show a shift to higher frequencies for higher temperatures indicating that they are relaxation peaks. The activation energy for the relaxation process is obtained from the plot of log peak frequency ($\omega_p$) against reciprocal temperature shown in figure 7. The activation energy is calculated to be 1·01 eV.

The temperature variation of AC conductivity is shown in the form of a $\log\sigma$ vs $T^{-1}$ plot (figure 8). It can be

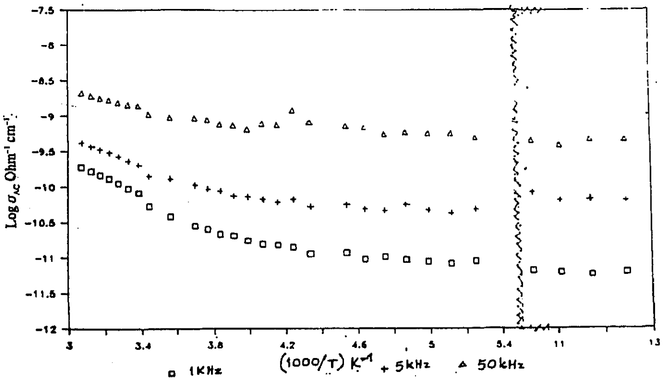

**Figure 3.** Variation of AC conductivity with reciprocal temperature at different frequencies.

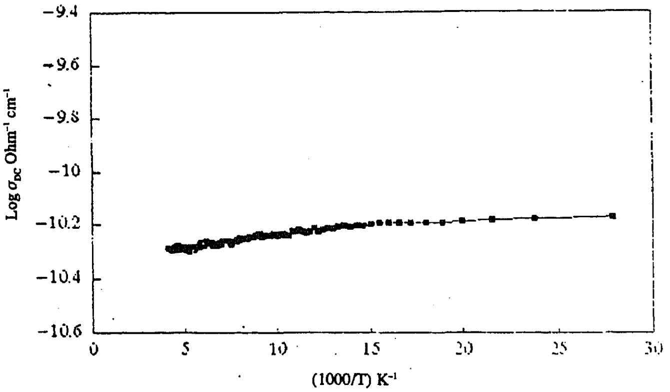

**Figure 4.** Variation of DC conductivity with reciprocal temperature.

**Table 1.** Dielectric constant of YIG.

| Sample | Frequency (temp.) | Dielectric constant | Reference |
|---|---|---|---|
| Polycrystalline | 2 MHz (R.T.) | ~ 12 | Anderson (1959) |

seen that a frequency-dependent slow increase is observed up to 500 K. The conductivity is found to be high for higher frequencies as in the case of variation at low temperatures discussed earlier. At 500 K, all the curves merge at a point showing frequency independence. The frequency dependence is shown once again beyond 500 K which is rather an unusual behaviour. These measurements were repeated to check for consistency. The same type of variation was observed in repeated measurements. The increase with temperature is faster beyond 500 K with higher values at lower frequencies and beyond 670 K an abrupt increase of more than two orders is observed.

The DC conductivity in the temperature range from room temperature to 700 K is shown in figure 9. Room temperature conductivity is of the order of $10^{-13}$ mho $cm^{-1}$. It reaches an order of $10^{-4}$ mho $cm^{-1}$ around 670 K and still higher beyond that temperature. It is to be noted that distinct kinks are observed at 500 K and 575 K. The temperature at which the first kink is observed corresponds to the point at which a frequency-independent conductivity is observed in AC conductivity just at one fixed temperature. Perhaps the nature of conduction changes beyond this point as discussed earlier. The second kink at higher temperature corresponds to Neel temperature of YIG (573 K). Lal *et al* (1982) observed similar variation for several iron garnets at the Neel temperature. For a related material, DyIG, Yadav and Lal (1979) have reported a break in the $\log \sigma$ vs $T^{-1}$ curve at magnetic ordering temperature. Change in the activation energy for conduction near curie temperature has been observed for Ti-substituted YIG by Om Prakash and Bahadur (1982).

The significance of such an observation can not be explained at this stage. It can only be said that magnetic ordering has some effect on conductivity. In the entire region, conduction is extrinsic and AC conductivity is higher than DC conductivity.

### 3.2 *Thermoelectric power*

The variations of thermoelectric power with temperature in the low- and high-temperature ranges are shown in figures 10a and b, respectively. The thermoelectric voltage, $\Delta E$ developed across the sample over a

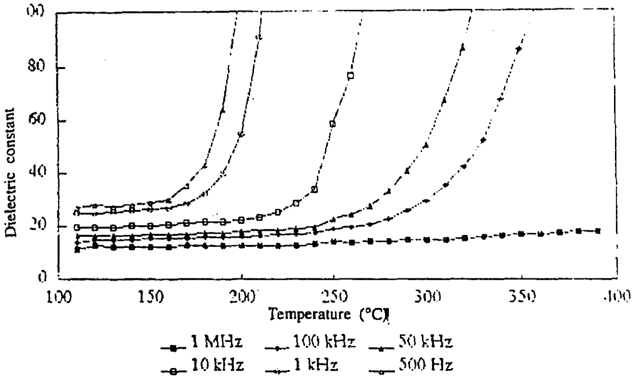

**Figure 5.** Variation of dielectric constant with temperature at different frequencies.

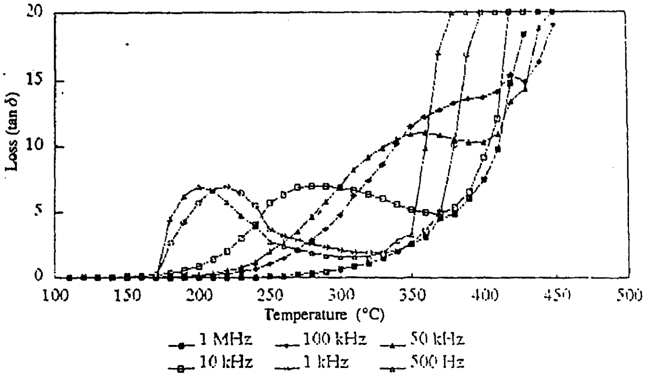

**Figure 6.** Variation of tan $\delta$ with temperature at different frequencies.

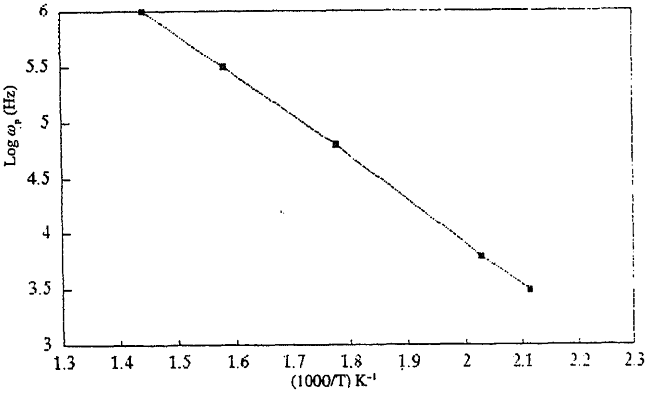

**Figure 7.** Variation of $\log \omega_p$ with reciprocal temperature.

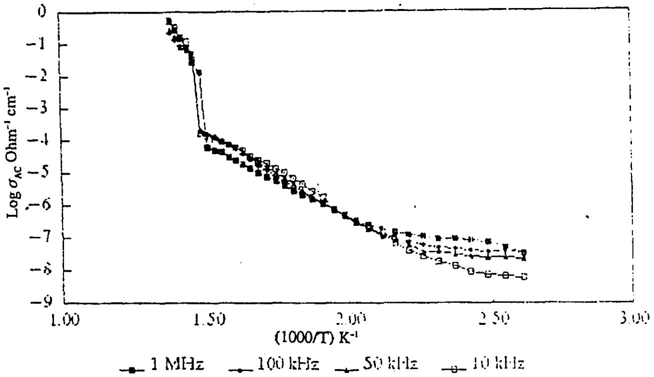

**Figure 8.** Variation of AC conductivity with reciprocal temperature at different frequencies.

temperature gradient, $\Delta T$ is shown as $S = \Delta E/\Delta T$. Following the convention adopted by Lal *et al* (1982), the positive sign of $S$ indicates negative charge carriers and *vice versa*. In the low-temperature range the thermoelectric power shows a gradual increase while decrease is observed beyond room temperature up to 700 K. Similar variation with an increase to a certain temperature has been observed in other oxide compounds (Om Prakash *et al* 1994). The charge carriers are $n$-type as shown by the sign of the thermoelectric power. The value remains almost constant at higher temperatures beyond 700 K.

## 4. Discussion

YIG shows $n$-type conduction due to the presence of substitutional cations or anion vacancies. Doping of YIG with $Si^{4+}$ induces creation of $Fe^{2+}$ ions. The simultaneous presence of $Fe^{3+}$ ions alter the electric and magnetic properties of garnets. The anisotropic magnetic resonance and slow relaxation phenomenon are examples of the electron exchange between the two irons (Judy 1966; Wurlitzer 1987). These effects in magnetic properties have been extensively studied as mentioned earlier. The sample used for the present investigation has marginal excess of donor concentrations. The sample characterization is given as $Si^{4+}$ (0·003) + F (0·02) (Haussuhl 1976) against the sum of divalent impurities $Fe^{2+}$ (0·01) + $Ca^{2+}$ (0·001) + Pb (0·011) (concentrations are expressed in the units of ions per formula unit of YIG). The presence of anion vacancies also introduces additional amounts of donor concentrations.

YIG is a cubic crystal $(I_a3_d - O_h^{10})$ with a structural chemical formula $Y_3Fe_3^{3+}Fe_2^{3+}O_{12}^{2-}$. The trivalent iron cations are distributed over two different sets of lattice sites; 'd' sublattice in which each cation is tetrahedrally surrounded by oxygen ions and 'a' sublattice with octahedral coordination. The yttrium ions occupy 'c' sites characterized by a dodecahedral oxygen coordination. The $Si^{4+}$ ions are known to structurally enter the 'd' sites forcing the reduction of some of the octahedrally-coordinated $Fe^{3+}$ ions to $Fe^{2+}$. The $Fe^{2+}$ ion may be considered as $Fe^{3+}$ cation plus an electron. The dipole formed with this electron and the positive charge located at tetrahedral 'd' sites lead complex polarizability. This accounts for the relaxation phenomenon observed in dielectric loss. As the temperature is increased, some of the electrons get ionized and participate in electrical conduction. The dipolar component gives an additional term in AC field. The AC conductivity is found to be two orders more than the DC conductivity. Thus conduction is due to the localized charge carriers. Metselaar and Larsen (1974) have proposed a model for the band structure for YIG. They are of the opinion that in dealing with the band

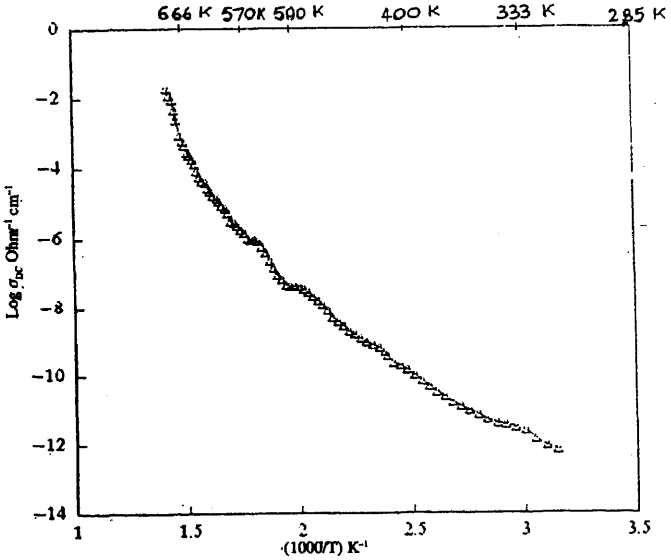

**Figure 9.** Variation of DC conductivity with reciprocal temperature.

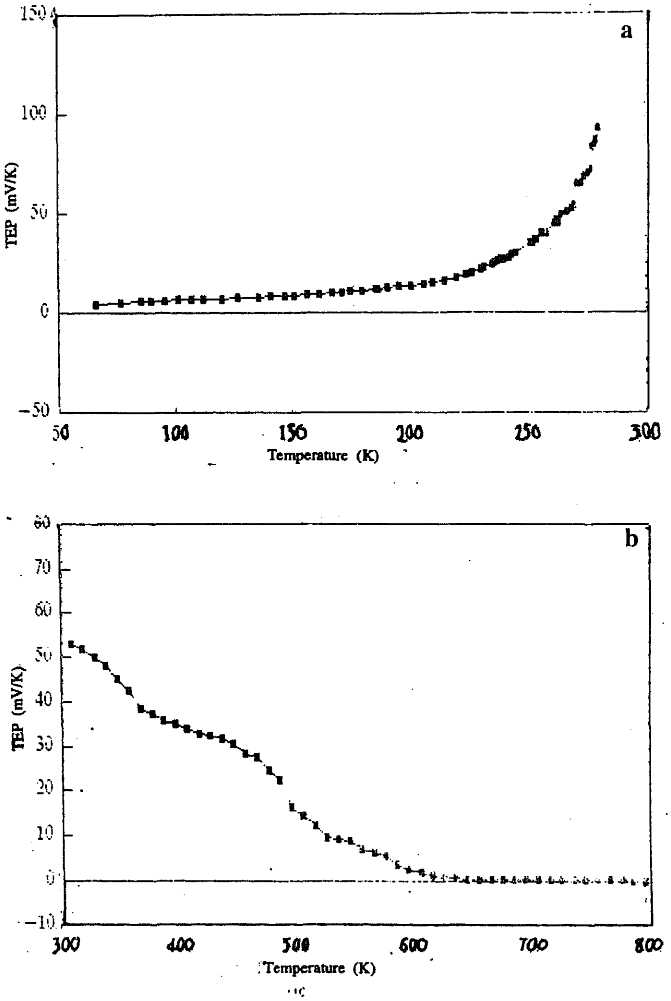

**Figure 10.** a–b. Variation of thermoelectric power with temperature.

structure of YIG the problems are similar to the case of transition metal oxides like NiO. Hence the conduction takes place in the narrow band derived from Fe (3*d*) orbitals which are octahedral in character. Lal *et al* (1982) proposed energy band diagram for rare earth garnets. $Fe^{3+}$-3*d* bands are shown to lie above the top of the uppermost completely filled $O^{2-}$-2*p* band.

Under normal situation these garnets should exhibit high metallic conduction. Experimentally it is found that pure garnets are insulators with conductivity less than $10^{-12}$ at room temperature. It may be concluded that $Fe^{3+}$-3*d* bands are localized. Hence in the presence of $Si^{4+}$ impurity the mode of conduction could only be due to localized electrons. The conduction mechanism can be understood by treating it as narrow band semiconductor as in the case of transition metal oxides and rare earth compounds.

Investigations of electrical conductivity in transition metal oxides (Adler and Feinleib 1970), rare earth sesquioxides (Subba Rao *et al* 1970; Lal *et al* 1976; Lal and Dar 1976) and in rare earth perovskites (Gschneidner and Eyring 1979) indicated polaron conduction through hopping mechanism. Though for DyIG conduction, thermally-activated hopping mechanism has been proposed by Yadav and Lal (1979). Om Prakash and Bahadur (1982) have explained the electrical properties of Ti-substituted YIG on the basis of electron hopping model as suggested by Austin and Mott (1969). For YIG, small polaron hopping mechanism is proposed by Petrov *et al* (1986) at high temperatures.

Theoretical work by several workers over the years has provided some understanding of conduction in oxides and transition metal compounds (Bosman and Van Daal 1970). For these materials, the interaction between electrons and optical phonons is strong and the conduction is explained on the basis of polarons.

The treatment of conduction by polarons is discussed by several workers (Appel 1968; Austin and Mott 1969; Mott and Davis 1971). Polarons belong to two categories, large and small polarons. In the large polaron model, the conductivity is by band mechanism at all temperatures and the AC conductivity decreases with frequency. The small polarons conduct in band-like manner up to a certain temperature, the conductivity showing an increase

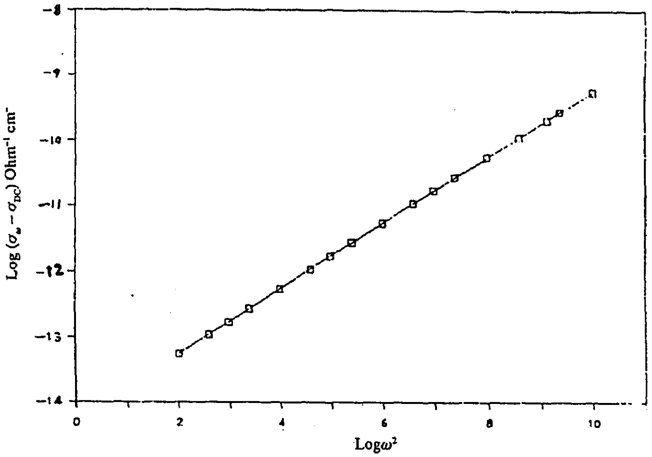

**Figure 11.** Variation of $\log(\sigma_\omega - \sigma_{DC})$ with $\log\omega^2$ at 90 K.

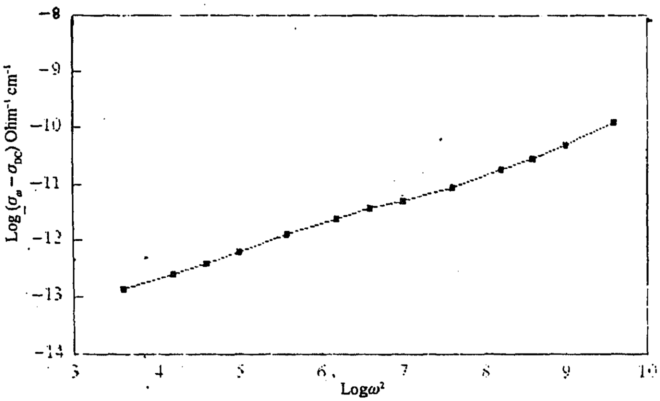

**Figure 12.** Variation of $\log(\sigma_\omega - \sigma_{DC})$ with $\log\omega^2$ at 200 K.

**Table 2.** Polaron parameters.

| Crystal parameters | Polaron parameters | Calculated values |
|---|---|---|
| $\varepsilon_s$ (Static dielectric constant)$^a = 12\cdot5$ | $r_p = 1/2\,[\pi/6N]^{1/3}$ | 0·918 Å |
| $\varepsilon_\alpha$ (High frequency dielectric constant)$^b = 4\cdot84$ | $\omega_0 = 2\pi\, K\theta/h$ | $7\cdot85 \times 10^{13}$ Hz |
| $\theta$ (Debye temperature)$^c = 600$ K | $\varepsilon_p = \varepsilon_s\,\varepsilon_\alpha/[\varepsilon_s - \varepsilon_\alpha]$ | 7·900 |
| $N$ (Number of sites per unit volume)$^d = 160/a^3$ | $W_p = e^2/[8\pi\,\varepsilon_0\,\varepsilon_p\,r_p]$ | 0·993 eV |
| Inter ionic distance$^e = 5\cdot7$ Å | $m^* = 20\,\varepsilon_p^2\,h^2\,\omega_p/e^2$ | $5\cdot88 \times 10^2\ m_e$ |
| $a$ (Lattice constant)$^f = 12\cdot376$ Å | $\alpha = e^2\,[m^*/2h^3\,\omega_e]^{1/2}/\varepsilon_p$ | 13·85 |
|  | $m_p = 0\cdot02\,m^*\,\alpha^4$ | $4\cdot33 \times 10^5\ m_e$ |

[a] Present value, [b] Hofmeister and Campbell (1992), [c] Landolt-Bornstein (1991), [d] Geller (1960), [e] Austin and Mott (1969) and [f] Gschneidner and Eyring (1979).

with frequency. At higher temperatures, the conduction is by thermally-activated hopping mechanism. The experimental results in the present case also shows the trend expected for small polaron conduction mechanism. It has been shown (Appel 1968; Adler 1968) that for ionic solids the concept of small polaron conduction is valid.

As an evidence for small polaron conduction, we have examined the variation of conductivity with frequency on the basis of relaxation process, as applied to bound small polaron (Adler and Feinleib 1970; Bosman and Van Daal 1970). Adler and Feinleib (1970) have shown that for conduction by small polarons the conduction increases with frequency and the following relation holds good:

$$\sigma_\omega - \sigma_{\mathrm{DC}} = \frac{\omega^2 \tau^2}{1+\omega^2 \tau^2}, \tag{2}$$

where $\omega$ is the angular frequency and $\tau$ the staying time ($\sim 10^{-10}$ sec) for frequencies $\omega^2 \tau^2 < 1$. $\log(\sigma_\omega - \sigma_{\mathrm{DC}})$ vs $\log \omega^2$ should be a straight line. Plots of $\log(\sigma_\omega - \sigma_{\mathrm{DC}})$ as a function of $\omega^2$ at two temperatures 90 K and 200 K, are shown in figures 11 and 12, respectively. It can be seen that the plots are straight lines. This indicates that the conduction is due to small polarons.

The important parameters associated with polarons are: polaron radius, $r_\mathrm{p}$, polaron binding energy, $W_\mathrm{p}$, effective mass, $m_\mathrm{p}$ and dimensionless electron–phonon coupling constant $\alpha$. The polaron parameters were evaluated from the data on dielectric constant and other crystal parameters using the relations given by Austin and Mott (1969). The input data and the polaron parameters are shown in table 2.

For small polarons $r_\mathrm{p}$ should be less than the inter ionic distance and the coupling constant should be greater than 6 (Bosman and Van Daal 1970). The values of the parameters are appropriate for small polarons.

## 5. Conclusions

The static dielectric constant for YIG is found to be 12·5 at room temperature at 1 MHz frequency. The disturbances observed in the dielectric constant around 130 K, 160 K and in the dielectric loss at three temperatures 130 K, 160 K and 285 K correspond to the peaks observed in magnetic loss and induced anisotropy measurements on silicon-doped samples. No indication of phase transition is observed. From AC and DC conductivity measurements, creation of $\mathrm{Fe}^{2+}$ due to the presence of $\mathrm{Si}^{4+}$ as impurity and electron hopping between $\mathrm{Fe}^{2+}$ and $\mathrm{Fe}^{3+}$ ions is believed to be the cause for conduction. Thermoelectric power data shows *n*-type charge carriers up to 700 K.

temperatures and by thermally-activated hopping mechanism at high temperatures. The relaxation pattern observed in the dielectric loss and the frequency variation of conductivity at low temperatures support this conclusion.

## Acknowledgements

We thank the referee for critical scrutiny of the paper and for many valuable suggestions. The authors also thank Prof. S Haussuhl, University of Koln, and Prof. W Tolkdorf, Germany, for the gift of garnet crystal. The authors are grateful to the Director, IUC; Dr A Ganesan, Indore, and Prof. S V Suryanarayana and Dr P Venugopal Reddy, Osmania University, Hyderabad for providing laboratory facilities. The senior author (LSD) is grateful to Prof. Donald E Scheule and Dr Z Z Zhong, Case Western Reserve University, USA, for providing facilities for the low-temperature dielectric measurements. Financial assistance from the Department of Science and Technology, New Delhi, is gratefully acknowledged.

## References

Adler D 1968 *Solid state physics* (eds) F Seitz, D Turnbull and H Ehrenreich (NY: Academic Press) **21** p. 1
Adler D and Feinleib 1970 *Phys. Rev.* **B2** 3112
Appel J 1968 *Solid state physics* (eds) F Seitz, D Turnbull and H Ehrenreich (NY: Academic Press) **21** p. 193
Anderson E E 1959 *J. Appl. Phys. Suppl.* **30** 299 S
Austin I G and Mott N F 1969 *Adv. Phys.* **18** 41
Bosman A J and Van Daal H J 1970 *Adv. Phys.* **19** 1
Bush G G 1988 *J. Appl. Phys.* **64** 5653
Chukalkin Y G, Shtirz V R and Goshchitskii B N 1989 *Phys. Status Solidi (a)* **112** 161
Elwell D and Dixon A 1968 *Solid State Commun.* **6** 585
Epstein D J and Frackiewicz 1959 *J. Appl. Phys. Suppl.* **30** 295
Fontana Jr. R E and Epstein D J 1971 *Met. Res. Bull.* **6** 959
Geller S 1960 *J. Appl. Phys. Suppl.* **31** 30
Gschneidner Jr. K A and Eyring L 1979 *Hand book of physics and chemistry of rare earths* 3 (New York: North-Holland and Physics Publishing Co)
Haussuhl S 1976 *Naturforsch Z.* **a31** 390
Hirakata S, Tanaka M, Kohn K, Kita E, Siratori E, Kimura S and Tasaki A 1991 *J. Phys. Soc. Jap.* **60** 294
Holstein T 1959 *Ann. Phys.* **8** 343
Hofmeister A M and Campbell K R 1992 *J. Appl. Phys.* **72** 638
Judy J H 1996 *J. Appl. Phys.* **37** 1328
Kita E, Takano S, Tasaki A, Siratori K, Kohn K and Kimura S 1988 *J. Appl. Phys.* **64** 5659
Krupichka S 1976 *The physics of ferrites and magnetic oxides related to them* (Russian Translation) (Moscow: Mir) 1st Edn
Lal H B, Verma B K and Dar N 1976 *Indian J. Cryogenics* **1** 119
Lal H B and Dar N 1976 *Indian J. Pure & Appl. Phys.* **14** 788

Landolt-Bornstein 1991 *Numerical Data and Functional Relationships in Science and Technology* (New York: Springer Verlag) **27**

Metselaar R and Larsen P K 1974 *Solid State Commun.* **15** 291

Mott N F and Davis E A 1971 *Phonons and polarons in electronics processing in non crystalline materials* (Oxford: Clarendon Press)

Om Prakash and Bahadur D 1982 *J. Appl. Phys.* **53** 8228

Om Prakash, Devendra Kumar and Durga Prasad Ch 1994 *J. Phys. D: Appl. Phys.* **27** 1509

Petrov A N, Denisov G V and Zhukovskii U M 1986 *Inorg. Mater. (USA)* **22** 579

Subba Rao G V, Ramdas S, Mehrotra P N and Rao
1970 *J. Solid State Chem.* **2** 377

Takano S, Kita E, Siratori K, Kohn K, Kimura S and
A 1991 *J. Phys. Soc. Jap.* **60** 288

Torres L, de Francisco D, Munoz J M, Zazo M and
J I 1993 *J. Appl. Phys.* **73** 6301

Wurlitzer M 1987 *Phys. Status Solidi (a)* **100** 607

Wurlitzer M and Richter 1970 *Phys. Status Solidi*
K211

Yadav V R and Lal H B 1979 *Jap. J. Appl. Ph*
2229

Bull. Mater. Sci., Vol. 21, No. 3, June 1998, pp. 227–231. © Indian Academy of Sciences.

# Optical and mechanical characteristics of zinc sulphide–thorium fluoride mixed composition thin films for use in the near infrared region (1–10 $\mu$m)

A BASU, B S VERMA, T K BHATTACHARYYA, M KAR and R BHATTACHARYYA*
Thin Film and Amorphous Materials Group, National Physical Laboratory, New Delhi 110 012, India

MS received 25 November 1997

**Abstract.** Mixed composition thin films of zinc sulphide–thorium fluoride have been deposited on glass and silicon substrates by thermal evaporation of mixtures of these materials in different proportions, from a single resistively heated source. The films are characterized for their optical properties (refractive index and extinction coefficient), mechanical properties (intrinsic stress), surface morphology and chemical composition. It is found that these films have tailorable refractive indices and low losses, and that films with certain compositions have low intrinsic stress and smooth surface morphology, making them suitable for incorporation in thin film multilayers for use in the near infrared region up to at least 10 $\mu$m.

**Keywords.** Mixed composition thin films; zinc sulphide–thorium fluoride; optical and mechanical characteristics; near IR region.

## 1. Introduction

It is well known that there are relatively few single materials available which are suitable for incorporation in thin film multilayer stacks useful in the near infrared region (1–10 $\mu$m). The fabrication of multilayer optical coatings with specified spectral characteristics in this region would be greatly simplified if low loss optical materials with tailorable refractive indices (especially in the low index range) and acceptable mechanical properties (low intrinsic stress, adequate hardness, etc) are available. Mixed composition films offer the possibility of solving this problem. So far, most studies of mixed composition films have been confined to the visible region. Only in recent years has interest been shown in mixed composition films useful in the near infrared region (Sankur *et al* 1988, 1991; Targrove and Murphy 1990; Gluck *et al* 1992, 1993). The mixed composition films reported so far, along with their regions of transparency, are listed in table 1.

Zinc sulphide and thorium fluoride are high and low index materials which are used for fabrication of multilayers in the near IR region. We therefore investigated mixed composition thin films of zinc sulphide and thorium fluoride in the search for a suitable thin film material with desirable properties.

## 2. Deposition of thin films of ZnS–ThF$_4$

Both zinc sulphide and thorium fluoride have the same evaporation temperature (1100°C). Therefore, mixtures of the two materials could be evaporated from the same resistively heated source. The two materials were taken in different proportions by weight (measured by a Mettler microbalance), ground and mixed together thoroughly in a mortar and pestle and put into a tungsten boat, covered with a perforated shield to prevent spattering of the material. The thermal evaporation was carried out under a vacuum of about $3 \times 10^{-6}$ mbar, and the thickness of the deposited film was monitored by an optical thickness

**Table 1.** Mixed composition films reported in the literature.

| Composition of film | Region of transparency ($\mu$m) | Reference |
|---|---|---|
| ZnSe–LaF$_3$ | 0·8–2·0 | Gluck *et al* (1992, 1993) |
| ZnSe–SrF$_2$ | 0·6–8·0 | Sankur *et al* (1991),<br>Gluck *et al* (1993) |
| Si–YF$_3$ | 1·5–7·0 | Sankur *et al* (1991),<br>Gluck *et al* (1993) |
| Si–ZnSe | 1·5–7·0 | Gluck *et al* (1992, 1993) |
| Si–ZnS | 1·5–7·0 | Gluck *et al* (1993) |
| LaF$_3$–BaF$_2$ | 0·25–2·0 | Targrove and Murphy (1990) |
| Ge–MgF$_2$ | 2·0–4·0 | Sankur *et al* (1988) |
| Ge–CeF$_3$ | 2·0–5·0 | Sankur *et al* (1988) |
| Ge–ZnS | 2·0–12·0 | Sankur *et al* (1988) |
| Ge–CdTe | 2·0–10·0 | Sankur *et al* (1988) |

---

*Author for correspondence

monitor to keep track of the film thickness. Films of physical thicknesses in the range 0·3–1·0 $\mu$m were deposited on substrates of ophthalmic glass (for refractive index, extinction coefficient and thickness measurements, as also for SEM and XRD studies), thin glass microslides (for stress measurements) and polished Si wafer pieces (for IR transmittance measurements and XPS studies for the chemical composition).

## 3. Determination of refractive index, extinction coefficient and thickness of the films

The refractive index, extinction coefficient and thickness of the films were determined from the trace of the transmittance vs wavelength of the films by the well known procedure described by Swanepoel (1983). The transmittance of the ophthalmic glass substrate coated with the film was measured as a function of wavelength from about 400–1500 nm. Depending on the thickness of the film, a number of maxima and minima were observed in the spectrophotometric trace. Figures 1a and b show typical traces for a pure ZnS film and a mixed composition ZnS–$ThF_4$ film deposited on glass substrates. The envelopes of the maxima and minima in these curves were drawn, and the values of transmittance (from actual transmittance curve or from envelope curve) at the wavelengths corresponding to each maximum or minimum were noted. A computer programme was developed which calculated the refractive index, $n$, extinction coefficient, $k$ and film thickness, $d$ at each of these wavelengths, on the basis of these transmittance values. These calculated results are also shown in figures 1a and b, along with the transmittance curves. The variation in the calculated values of $d$ at the different wavelengths, and the corresponding variations in the refractive indices calculated using these values of $d$, gave estimates of the uncertainties in the values of $n$ and $d$ at each wavelength. The values of $k$ are of the order of $10^{-3}$, which shows that these films are almost transparent in the near infrared region.

The refractive indices, extinction coefficients and thicknesses of a few selected films were also determined from ellipsometric measurements at 546·1 nm wavelength, and were found to agree with the values determined by the above method to within a few per cent. The thicknesses of a few films were also determined directly by

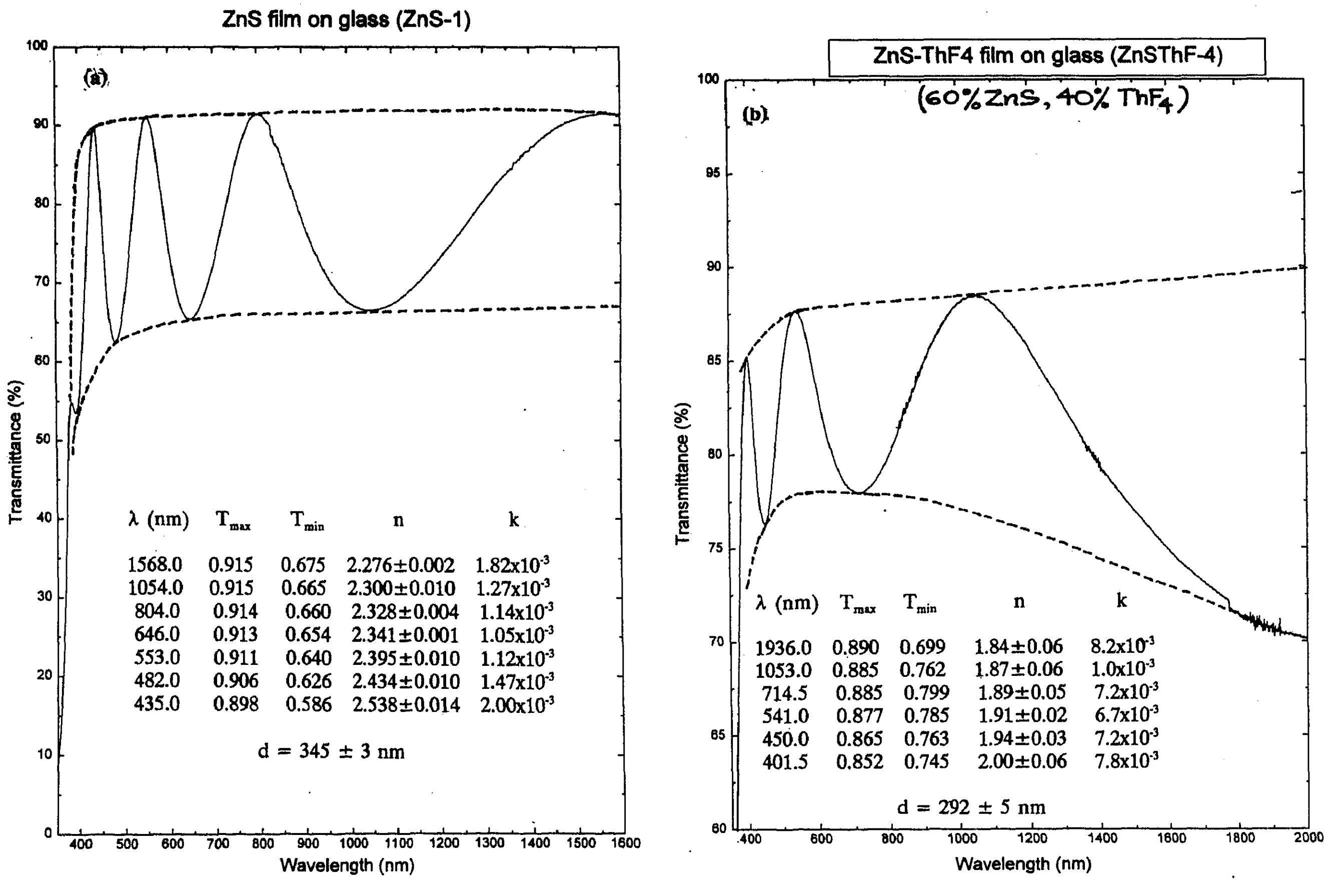

ZnS film on glass (ZnS-1)

ZnS-ThF4 film on glass (ZnSThF-4)

(60%ZnS, 40% ThF4)

| λ (nm) | $T_{max}$ | $T_{min}$ | n | k |
|---|---|---|---|---|
| 1568.0 | 0.915 | 0.675 | 2.276±0.002 | $1.82 \times 10^{-3}$ |
| 1054.0 | 0.915 | 0.665 | 2.300±0.010 | $1.27 \times 10^{-3}$ |
| 804.0 | 0.914 | 0.660 | 2.328±0.004 | $1.14 \times 10^{-3}$ |
| 646.0 | 0.913 | 0.654 | 2.341±0.001 | $1.05 \times 10^{-3}$ |
| 553.0 | 0.911 | 0.640 | 2.395±0.010 | $1.12 \times 10^{-3}$ |
| 482.0 | 0.906 | 0.626 | 2.434±0.010 | $1.47 \times 10^{-3}$ |
| 435.0 | 0.898 | 0.586 | 2.538±0.014 | $2.00 \times 10^{-3}$ |

d = 345 ± 3 nm

| λ (nm) | $T_{max}$ | $T_{min}$ | n | k |
|---|---|---|---|---|
| 1936.0 | 0.890 | 0.699 | 1.84±0.06 | $8.2 \times 10^{-3}$ |
| 1053.0 | 0.885 | 0.762 | 1.87±0.06 | $1.0 \times 10^{-3}$ |
| 714.5 | 0.885 | 0.799 | 1.89±0.05 | $7.2 \times 10^{-3}$ |
| 541.0 | 0.877 | 0.785 | 1.91±0.02 | $6.7 \times 10^{-3}$ |
| 450.0 | 0.865 | 0.763 | 1.94±0.03 | $7.2 \times 10^{-3}$ |
| 401.5 | 0.852 | 0.745 | 2.00±0.06 | $7.8 \times 10^{-3}$ |

d = 292 ± 5 nm

**Figure 1.** Plots of the transmittance vs wavelength for two films: ZnS-1 (a) and ZnSThF-4 (b), deposited on ophthalmic glass substrates. The envelopes of the transmittance maxima and minima are shown. The results of calculations (§ 3)—the values of

a stylus scan measurement in a Talystep instrument, and the values were again found to be in good agreement with the previously determined values.

In figure 2, we have plotted the dispersion curves for the refractive indices of a pure ZnS film and a film (ZnSThF-4) fabricated from a mixture with 60% ZnS and 40% $ThF_4$ by weight. The refractive index shows a regular decrease with increasing wavelength in both cases, as expected.

In figure 3, we have plotted the refractive index of each film at 1 μm (obtained by interpolation from the refractive index vs wavelength data) against the ratio $f$ for the film, defined as

$$f = w/(1+w), \quad w = w_L/w_H,$$

where $w_L$ is the weight of $ThF_4$ (low index, $n_L$, constituent) in evaporation mixture and $w_H$ the weight of ZnS (high index, $n_H$, constituent) in evaporation mixture.

As we shall show later (§ 7), the fractional composition by weight of a film is found to agree with the fractional composition by weight of the evaporation mixture.

There are various models (linear and non-linear) that predict the refractive index of a mixed composition film (Niklasson *et al* 1981), and some researchers, e.g. Chen *et al* (1996), have tried to fit their refractive index vs fractional composition data for mixed composition films to one or the other model. However, the scatter in the refractive index vs $f$ data in figure 3 does not warrant the fitting to a particular model. Other researchers (Gluck *et al* 1992) have also expressed the same opinion. We can, however, say that in the present case the refractive index of the ZnS–$ThF_4$ mixed composition film varies monotonically with composition (represented by the fraction, $f$) and follows an approximately linear relation. In fact, the dotted line in figure 3 is the result of the Linear Model (Niklasson *et al* 1981), according to which the effective refractive index of the mixed composition film is given by

$$n_{\text{eff}} = (n_H \cdot w_H + n_L \cdot w_L)/(w_H + w_L)$$
$$= (1-f) \cdot n_L + f \cdot n_H = n_L + f \cdot (n_H - n_L),$$

using the expression for $f$ given earlier.

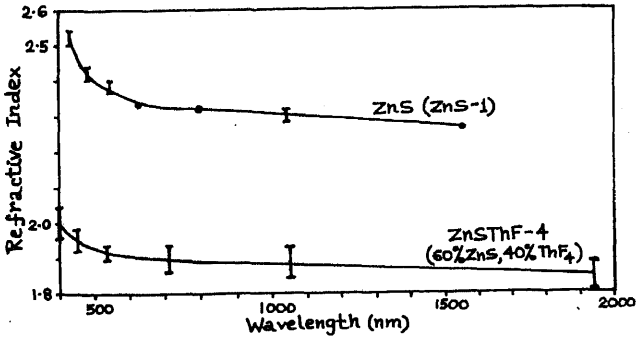

**Figure 2.** Refractive index (calculated in § 3) vs wavelength for the two films ZnS-1 and ZnSThF-4.

## 4. Stress measurement

The intrinsic stresses in the mixed composition films of ZnS–$ThF_4$ are expected to be small, since ZnS films have been reported to have moderate compressive stress and $ThF_4$ films have moderate tensile stress. The intrinsic stresses in the films were determined by a laser scanning set-up. Light from a HeNe laser was passed through a beam expander and aperture to obtain a collimated beam which would not suffer much divergence over a distance of several metres. The laser beam was split by a beam-splitter into two beams: one was sent off to the side, and the other was directed to the sample under investigation. After reflection from the sample, this beam was directed by the same beamsplitter to a position sensitive quadrant detector, or to a screen a few metres away. The laser beam spot on the sample was translated over the surface of the sample by a micrometer over a distance of several mm, in a direction normal to the incident light, and the resultant deflection of the reflected light beam (which would indicate curvature of the sample surface) was measured by the position sensitive detector or on the screen. For deflections of less than 1 cm, the detector could measure the deflection to an accuracy of 0·1 mm. But greater accuracy was usually obtained by measuring a deflection of a few cm on the screen.

The intrinsic stress in the film was determined by the following relation:

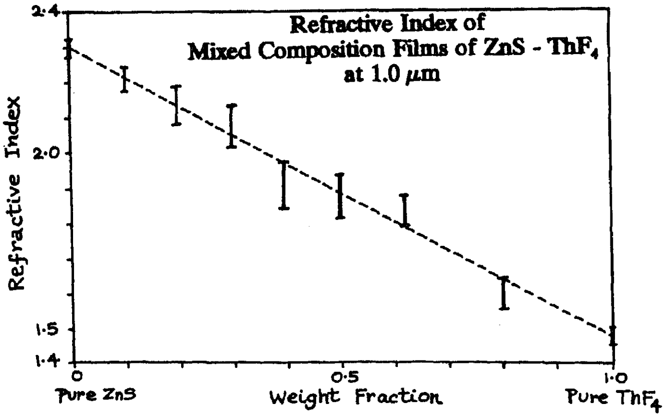

**Figure 3.** Refractive index at 1 μm (calculated in § 3 and interpolated to 1 μm) vs the weight fraction, for various mixed composition films. The dashed line is the plot corresponding to the theoretical Linear Model.

$$\text{Film stress } \sigma = \frac{E t_s^2}{6 t_f (1-\mu)}\left[\frac{1}{R}-\frac{1}{R_0}\right],$$

where $E$ is the Young's modulus, $\mu$ the Poisson's ratio, $t_s$ the thickness of substrate, $t_f$ the film thickness and $R$ and $R_0$ are the radii of curvature of substrate before and after deposition of film, and

$$R = 2xL/d,$$

where $x$ is the displacement of sample, $L$ the distance of screen/detector from sample and $d$ the displacement of beam spot, and similarly for $R_0$.

For the thin glass microslide used as the substrate for stress measurements (Corning 0211 alkali zinc borosilicate sheet glass), we used the values [Corning catalog]: $E = 7{\cdot}45 \times 10^{10}\,\mathrm{N/m^2}$, $\mu = 0{\cdot}22$, $t_s = 0{\cdot}15$ mm.

The radius of curvature of the substrate was measured at the centre of the substrate before and after deposition of the film. The results of measurement are shown in figure 4. Compressive stresses are shown as positive and tensile stresses as negative. For ease of representation of positive and negative stresses in the same figure, and since stresses have usually been expressed in kg/cm$^2$ in the literature, we have expressed the stresses in our films in kg/cm$^2$, using the conversion 1 kg/cm$^2 = 9{\cdot}8 \times 10^4$ N/m$^2$. We see that as the weight fraction of $\mathrm{ThF_4}$ in the mixed composition films increases, the intrinsic stress changes from compressive to tensile, and a film with a weight fraction of about 0·5, i.e. a film with about 50 : 50 ratio of ZnS–$\mathrm{ThF_4}$, has very low stress. This is an illustration of the reduction of intrinsic stresses in mixed composition films reported by several researchers (Austin 1973; Sankur *et al* 1988, 1991; Targrove and Murphy 1990; Gluck *et al* 1992, 1993).

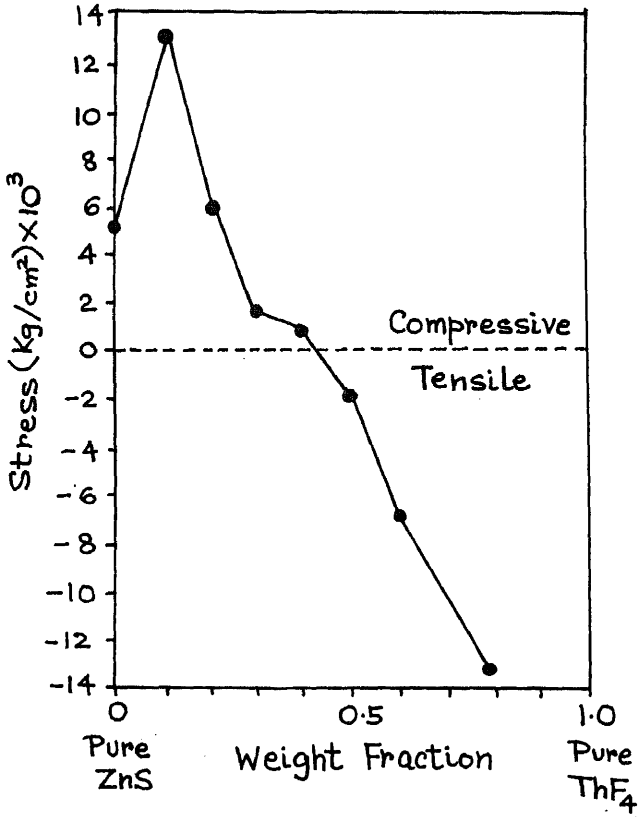

**Figure 4.** Intrinsic stress (in kg/cm$^2$) vs the weight fraction for the various mixed composition films studied in § 4. Compressive stresses are shown as positive and tensile stresses as negative.

## 5. Surface morphology

The mixed composition films were examined under a scanning electron microscope to see the surface roughness, cracks or other surface features of the films. The films were examined both at normal incidence and at oblique incidence up to a magnification of 15,000×. However, all the films exhibited featureless surface morphology up to this magnification. We therefore anticipate that these films will exhibit very low optical scattering losses and hence are suitable for use in optical multilayer stacks without introducing appreciable scattering losses.

## 6. Transparency in near IR (1–10 $\mu$m) range

The IR transmittance spectrum of thin films coated on silicon substrates was measured on a Perkin-Elmer spectrophotometer from 2·5–10 $\mu$m. The spectra showed absorption peaks of the silicon substrate at about 9·1 $\mu$m, and were otherwise quite flat over this entire range. We therefore conclude that these thin films are almost transparent over the wavelength range of interest, and are thus suitable for the fabrication of multilayer stacks.

## 7. Structure and chemical composition

X-ray diffraction studies of some of the mixed composition films showed a peak corresponding to zinc sulphide, but there was no defined peak corresponding to thorium fluoride. This is clearly seen in the plots in figure 5, for films ZnSThF-1 (a), ZnSThF-4 (b) and ZnSThF-8 (c). The films in (a) and (b) have large weight fractions of ZnS, and the diffraction peaks corresponding to ZnS are clearly seen. The film in (c) is predominantly $\mathrm{ThF_4}$, and no diffraction peak is seen here. This indicates that zinc sulphide exists in a crystalline phase in the mixed composition films, while thorium fluoride exists in an amorphous phase.

The chemical composition of the mixed composition films was determined by the XPS technique, where

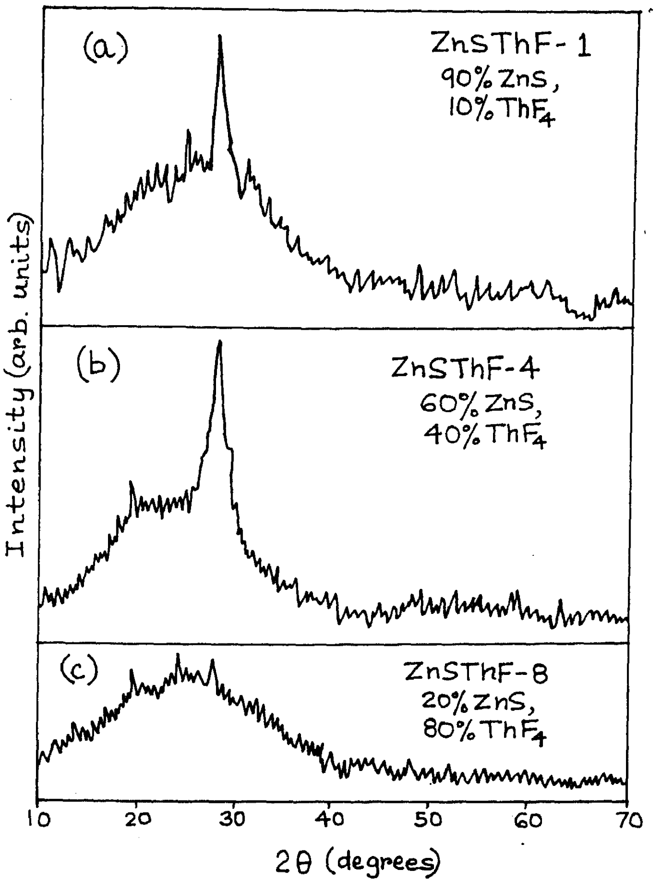

**Figure 5.** X-ray diffraction plots for three mixed composition films, showing the peak corresponding to ZnS and the absence of a peak corresponding to ThF$_4$.

surface scans of some of the films showed that the films were comprised of ZnS and ThF$_4$ only. The weight proportions of ZnS and ThF$_4$ in the films were found to be quite close to the weight proportions in the evaporation mixture.

## 8. Conclusions

The mixed composition films of zinc sulphide and thorium fluoride have tailorable refractive indices (from about 2·3–1·5 at 1 $\mu$m wavelength) and fairly low extinction coefficients, of the order of $10^{-3}$ or lower. The intrinsic stress is very low for film compositions with a 50 : 50 ratio by weight of ZnS and ThF$_4$. The films exhibit almost featureless surface morphology and therefore should have low optical scattering losses. Further, while ZnS appears to exist in a crystalline phase in these films, ThF$_4$ appears to exist in an amorphous phase. In conclusion, these mixed composition films should be useful in the fabrication of multilayer stacks to meet specified spectral characteristics in the near IR region.

## Acknowledgements

This work was carried out under a research grant from the Ministry of Science and Technology (Science and Engineering Research Council), Govt of India, for which we are most grateful.

We wish to place on record our gratitude to the several people who helped us to characterize the thin film samples: Mr Sushil Kumar for the stress setup and measurements, Dr S P Verma and Dr D Gupta for the IR transmittance measurements, Dr R P Pant for the X-ray diffraction analysis, Dr C Anandan for XPS studies and Mr K B Ravat for the SEM studies.

## References

Austin R R 1973 *Appl. Opt.* **12** 665

Catalog for Speciality Glasses and Glass Ceramic Materials, Corning Glass Works, Corning, NY, USA

Chen J-S, Chao S, Kao J-S, Niu H and Chen C-H 1996 *Appl. Opt.* **35** 90

Gluck N S, Taber D B, Heuer J P, Hall R L and Gunning W J 1992 *Appl. Opt.* **31** 6127

Gluck N S, Sankur H O and Taber D 1993 *Society of vacuum coaters, 36th annual technical conference proceedings* (USA: Society of Vacuum Coaters) p. 119

Niklaason G A, Granqvist C G and Hunderi O 1981 *Appl. Opt.* **20** 26

Sankur H O, Gunning W J and DeNatale J F 1988 *Appl. Opt.* **27** 1564

Sankur H O, DeNatale J F and Gunning W J 1991 *Appl. Opt.* **30** 495

Swanepoel R 1983 *J. Phys. E.: Sci. Instrum.* **16** 1214

Targrove J D and Murphy A R 1990 *Thin Solid Films* **191** 47

# Magnetic ordering in $Mg_{1+x}Mn_xFe_{2-2x}O_4$ system

N N JANI[†], B S TRIVEDI, H H JOSHI, G K BICHILE[‡] and R G KULKARNI*
Department of Physics, [†]Department of Computer Science, Saurashtra University, Rajkot 360 005, India
[‡]Physics Department, Dr B A Marathwada University, Aurangabad 431 004, India

MS received 25 August 1997; revised 24 March 1998

**Abstract. Magnetization measurements of the ferrite system $Mg_{1+x}Mn_xFe_{2-2x}O_4$ were undertaken primarily to study variation of the saturation magnetization with manganese concentration and to gain information about the type of magnetic ordering. The observations indicate the existence of Yafet–Kittel (YK) type of magnetic ordering in this system which is well supported by results of Mössbauer effect measurements. A molecular field analysis of the YK spin ordering using the three-sublattice model is shown to explain the experimental data satisfactorily.**

**Keywords. Ferrites; magnetic ordering; collinear; non-collinear.**

## 1. Introduction

This possibility of changing continuously the concentration of non-magnetic ions in the different sublattices makes the ferrites very interesting materials to study the appearance of various magnetic structures (Bhargava and Zeeman 1980; Brand *et al* 1985; Muralidharan *et al* 1985; Dormann *et al* 1987; Chakravarthy *et al* 1988; Dormann and Nogues 1990; Jotania *et al* 1992). Among these, systems with spinel structure seems to be particularly attractive, as they allow a variety of magnetic disorder and frustration to be introduced. This is due to the fact that, in spinel intra-sublattice interactions are weaker than the inter-sublattice interactions, as a result there are unsatisfied bonds in the ferrimagnetic phase. Because of these unsatisfied bonds increasing magnetic dilution accentuates the competition between the various exchange interactions resulting in a variety of magnetic structures (Bhargava and Zeeman 1980; Brand *et al* 1985; Muralidharan *et al* 1985; Dormann *et al* 1987; Chakravarthy *et al* 1988; Dormann and Nogues 1990; Jotania *et al* 1992).

A large number of investigators have studied Ti-substituted spinels in order to understand their magnetic properties. Brand *et al* (1985) found in the case of $Mg_{1+x}Ti_xFe_{2-2x}O_4$ that on increasing dilution $x$, the collinear ferrimagnetic phase breaks down before reaching the ferrimagnetic percolation threshold and for higher concentration of Ti, system approaches toward spin-glass. Dormann *et al* (1987) have also studied the magnetization measurements of $Ti^{4+}$ substituted lithium ferrite using different techniques and suggested the possibility of canted spin arrangements to explain the magnetization measurements.

In order to understand the influence of magnetic ion $Mn^{4+}$ in place of non-magnetic ion $Ti^{4+}$, we have modified the magnetic phase of $Mg_{1+x}Ti_xFe_{2-2x}O_4$ by replacing $Ti^{4+}$ by $Mn^{4+}$, so that intra-sublattice interaction ($J_{BB}$) will become predominant over the inter-sublattice interaction ($J_{AB}$), which may lead to a frustration in the spin sub systems. In our recent communication (Jani *et al* 1997), we have reported magnetic properties on the mixed spinel $Mg_{1+x}Mn_xFe_{2-2x}O_4$. The present paper reports the results of X-ray, magnetization and Mössbauer effect measurements on the $Mg_{1+x}Mn_xFe_{2-2x}O_4$ system. The variation of the saturation magnetization per formula unit in Bohr magneton number ($n_B$) with Mn-concentration in this system is similar in nature to that in the Ni–Zn (Satyamurthy *et al* 1969) and Cu–Zn (Kulkarni and Patil 1982) ferrites and the existence of Y–K angles on the B-site, observed in the latter systems is strongly suspected. A molecular field analysis of the Y–K spin ordering using a three-sublattice model is shown to explain the experimental data satisfactorily.

## 2. Experimental

Nine samples of Mn-substituted $Mg_{1+x}Mn_xFe_{2-2x}O_4$ system were prepared by the usual double sintering ceramic method for $0{\cdot}1 \leq x \leq 0{\cdot}9$ in steps of 0·1. The starting materials were analytical reagent grade oxides, $Fe_2O_3$, MgO and $MnO_2$. These oxides were mixed in proper proportions and presintered at 990°C for 24 h. In the final sintering process the material was held at 1050°C for 12 h and slowly cooled to room temperature (2°C/min). The X-ray diffractograms were obtained using $FeK_\alpha$ radiation on a Philips X-ray diffractometer model PW-1820. The diffraction patterns show the sharp lines corresponding to a single phase spinel for all the samples.

---

*Author for correspondence

The magnetization measurements of each sample at 300 K were carried out using high-field hysteresis loop technique (Radhakrishnamurthy *et al* 1971). The Mössbauer spectra were obtained at 12 K and 300 K in transmission geometry with source of 10 mCi $^{57}$Co(Pd) and a constant acceleration transducer interface to PC-based 1024 multi channel analyser.

## 3. Results and discussion

All the compositions of the system $Mg_{1+x}Mn_xFe_{2-2x}O_4$ exhibit single phase cubic spinel structure. No reflections other than those belonging to a spinel structure were observed in the patterns (figure 1). The values of lattice constant '$a$' (Å) determined from X-ray data with an accuracy of $\pm 0{\cdot}002$ Å for $x=0{\cdot}1$ to $0{\cdot}9$ are shown in figure 2 as a function of $x$. It is clear from figure 2 that the '$a$' parameter initially increases up to $x=0{\cdot}4$ and thereafter it levels off for further increase in $x \geq 0{\cdot}5$. The observed nonlinear behaviour in '$a$' with $x$ may be attributed to the simultaneous replacement of $Fe^{3+}$ (0·64 Å), $Mg^{2+}$ (0·60 Å) and $Mn^{4+}$ (0·60 Å). The cation distribution of $MgFe_2O_4$ ($x=0$) has been reported to be

$$(Mg_{0{\cdot}08}Fe_{0{\cdot}92})^A\,[Mg_{0{\cdot}92}Fe_{1{\cdot}08}]^B\,O_4, \tag{1}$$

where A is the tetrahedral site and B the octahedral site. In order to determine the cation distribution, XRD intensities were calculated using the formula suggested by Buerger (1960):

$$I_{hkl} = |F_{hkl}|^2\, PL_P, \tag{2}$$

where notations have their usual meanings. The distribution of divalent, trivalent and tetravalent cations amongst octahedral and tetrahedral sites in the $Mg_{1+x}Mn_xFe_{2-2x}O_4$ samples are determined from the ratios of intensities of X-ray diffraction lines: $I_{220}/I_{440}$, $I_{220}/I_{400}$ and $I_{400}/I_{422}$. In table 1, the results of X-ray intensity calculations for typical samples $x=0{\cdot}2$, $0{\cdot}6$, $0{\cdot}8$ and $0{\cdot}9$, are listed along with experimental intensity ratios. It is evident from table 1 that tetravalent Mn-ions occupy B-site replacing B-site iron and the added $Mg^{2+}$ ions substitute for A-site iron without any change with $x$ in the initial degree of inversion i.e. (1).

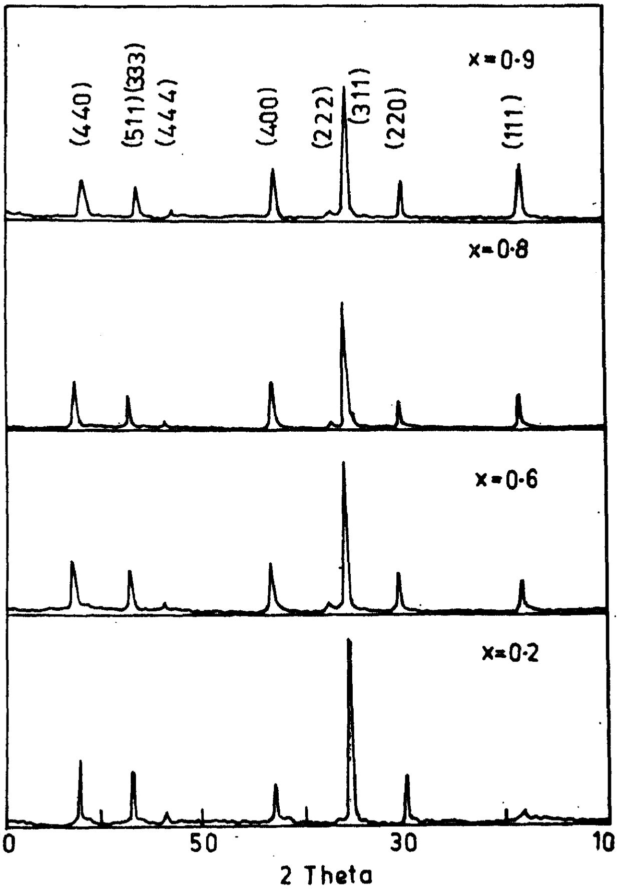

**Figure 1.** Typical X-ray diffractograms of the system $Mg_{1+x}Mn_xFe_{2-2x}O_4$ for $x=0{\cdot}2$, $0{\cdot}6$, $0{\cdot}8$ and $0{\cdot}9$.

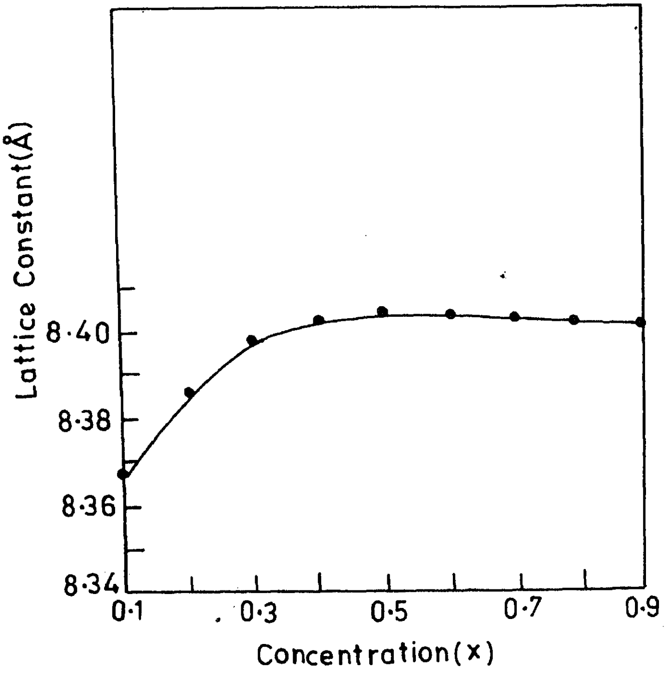

**Figure 2.** Variation of lattice parameter $a$ (Å) with Mn concentration $x$.

In deriving the cation distribution of $Mg_{1+x}Mn_xFe_{2-2x}O_4$ our X-ray intensity calculations (table 1) and relative $Fe^{3+}$ intensities of Mössbauer spectra (table 2), for A and B site ions were taken into account. Accepting the cation distribution of $MgFe_2O_4$ (1), an approximate cation distribution for the $Mg_{1+x}Mn_xFe_{2-2x}O_4$ can be written as

**Table 1.** Comparison of X-ray intensities ratio for $\mathrm{Mg}_{1+x}\mathrm{Mn}_x\mathrm{Fe}_{2-2x}\mathrm{O}_4$ in estimating cation distribution.

| $x$ | Lattice constant $a$ (Å) | A-site cation | B-site cation | $I_{220}/I_{440}$ Obs. | $I_{220}/I_{440}$ Cal. | $I_{220}/I_{400}$ Obs. | $I_{220}/I_{400}$ Cal. | $I_{400}/I_{422}$ Obs. | $I_{400}/I_{422}$ Cal. |
|---|---|---|---|---|---|---|---|---|---|
| 0·2 | 8·3853 | $\mathrm{Mg}_{0\cdot28}\mathrm{Fe}_{0\cdot72}$ | $\mathrm{Mg}_{0\cdot92}\mathrm{Mn}_{0\cdot20}\mathrm{Fe}_{0\cdot88}$ | 0·82 | 0·82 | 1·33 | 1·35 | 2·49 | 2·14 |
| 0·6 | 8·4320 | $\mathrm{Mg}_{0\cdot66}\mathrm{Fe}_{0\cdot34}$ | $\mathrm{Mg}_{0\cdot94}\mathrm{Mn}_{0\cdot60}\mathrm{Fe}_{0\cdot46}$ | 0·78 | 0·53 | 0·76 | 0·66 | 6·10 | 4·46 |
| 0·8 | 8·3984 | $\mathrm{Mg}_{0\cdot82}\mathrm{Fe}_{0\cdot18}$ | $\mathrm{Mg}_{0\cdot98}\mathrm{Mn}_{0\cdot80}\mathrm{Fe}_{0\cdot22}$ | 0·74 | 0·33 | 0·66 | 0·43 | 6·80 | 6·30 |
| 0·9 | 8·3965 | $\mathrm{Mg}_{0\cdot91}\mathrm{Fe}_{0\cdot09}$ | $\mathrm{Mg}_{0\cdot99}\mathrm{Mn}_{0\cdot90}\mathrm{Fe}_{0\cdot11}$ | 0·81 | 0·29 | 0·74 | 0·35 | 6·23 | 7·87 |

*$a$(Å) error ± 0·002 Å.

**Table 2.** Mössbauer parameters of $\mathrm{Mg}_{1+x}\mathrm{Mn}_x\mathrm{Fe}_{2-2x}\mathrm{O}_4$ obtained at 12 K. Average sublattice magnetization, $\mu(x)$ in $\mu_B$.

| $x$ | Isomer shifts (mm/s)* $IS_A$ | Isomer shifts (mm/s)* $IS_B$ | Hyperfine fields (KOe) $H_A$ | Hyperfine fields (KOe) $H_B$ | Mössbauer intensity ratio $I_B(\mathrm{Fe}^{3+})/I_A(\mathrm{Fe}^{3+})$ | $\mu(x) = n_B^M(x)$ in $\mu_B$ |
|---|---|---|---|---|---|---|
| 0·2 | 0·37 ± 0·05 | 0·37 ± 0·05 | 506 ± 3 | 523 ± 3 | 1·22 | 1·39 |
| 0·6 | 0·32 ± 0·05 | 0·32 ± 0·05 | 489 ± 3 | 510 ± 3 | 1·35 | 2·50 |
| 0·8 | 0·32 ± 0·05 | 0·32 ± 0·05 | 469 ± 3 | 495 ± 3 | 1·22 | 2·98 |
| 0·9 | 0·32 ± 0·05 | 0·32 ± 0·05 | 448 ± 3 | 480 ± 3 | 1·22 | 3·15 |

*$IS$ w.r.t. $\alpha$-Fe.

$$(\mathrm{Mg}_{0\cdot08+x}\mathrm{Fe}_{0\cdot92-x})^{\mathrm{A}}\,[\mathrm{Mg}_{0\cdot92}\mathrm{Mn}_x\mathrm{Fe}_{1\cdot08-x}]^{\mathrm{B}}\,\mathrm{O}_4. \tag{3}$$

Equation (3) expresses that the added $\mathrm{Mg}^{2+}$ ions substituted for A-site $\mathrm{Fe}^{3+}$ and the $\mathrm{Mn}^{4+}$ ions for B-site $\mathrm{Fe}^{3+}$ without any change in the initial degree of inversion except $x = 0{\cdot}6$. The experimental integrated intensity ratios of the A and B sites, $^{57}\mathrm{Fe}$ spectra and those calculated on the basis of cation distribution obtained from X-ray intensity data given in table 1, are in very good agreement with each other (table 2) for $0{\cdot}2 \le x \le 0{\cdot}9$.

The saturation magnetization ($\sigma_s$) and the magnetization number ($n_B$) at 300 K obtained from magnetization data for $x = 0{\cdot}1$–$0{\cdot}9$ are summarized in table 3. From field dependence of magnetization and observed magnetic moments at 300 K (table 3), it is clear that the samples with $x = 0{\cdot}0$–$0{\cdot}6$ show ferrimagnetic behaviour in agreement with Mössbauer data at 300 K (figure 3) which decreases with increasing $x$ values and samples with $x \ge 0{\cdot}7$ display paramagnetic behaviour. Figure 4 shows the variation of $n_B$ with $x$ for $x = 0{\cdot}0$–$0{\cdot}9$ at 300 K, $n_B$ increases with $x$ up to $x \le 0{\cdot}3$ and thereafter it decreases.

According to Neel's (1950), two sublattice models of ferrimagnetism, the magnetic moment per formula unit in $\mu_B$, $n_B^N$, is expressed as

$$n_B^N(x) = M_B(x) - M_A(x), \tag{4}$$

**Table 3.** Saturation magnetization $\sigma_s$ (emu/g) and saturation magnetization per formula unit in Bohr magnetons, $n_B$ at 300 K. The values of the exchange constants in K used in calculating $\alpha_{YK}$ are given as footnote.

| $x$ | Magnetization (300 K) $\sigma_s$ (emu/gm) | Magnetization (300 K) $n_B$ ($\mu_B$) | Yafet–Kittel angles $\alpha_{YK}$ (exp.) | Yafet–Kittel angles $\alpha_{YK}$ (cal.) |
|---|---|---|---|---|
| 0·0 | 23·2 | 0·80 | 0° | 0° |
| 0·1 | 29·2 | 1·03 | 0° | 0° |
| 0·2 | 43·2 | 1·50 | 0° | 0° |
| 0·3 | 45·3 | 1·55 | 14°36′ | 19°40′ |
| 0·4 | 39·5 | 1·32 | 31°27′ | 30°05′ |
| 0·5 | 38·4 | 1·26 | 40°09′ | 39°22′ |
| 0·6 | 28·5 | 0·92 | 53°07′ | 48°03′ |
| 0·7 | 22·2 | 0·70 | 63°11′ | 57°44′ |
| 0·8 | 11·4 | 0·36 | 83°39′ | 71°06′ |
| 0·9 | – | – | – | – |

$J_\alpha = -14{\cdot}0$; $J_\beta = -13{\cdot}0$; $J_\delta = -10{\cdot}0$; $J_\gamma = -4{\cdot}5$ and $J_\varepsilon = -7{\cdot}5$.

where $M_B$ and $M_A$ are B and A sublattice magnetic moments in $\mu_B$. The $n_B^N$ ($\mu_B$) values for $x = 0{\cdot}0$–$0{\cdot}9$ were calculated using the ionic magnetic moments of $\mathrm{Fe}^{3+}$, $\mathrm{Mn}^{4+}$ and $\mathrm{Mg}^{2+}$ with respective values $5\,\mu_B$, $3\,\mu_B$ and $0\,\mu_B$ in (3) and the results are shown in figure 4 as a solid line. The calculated $n_B^N$ values for $x = 0{\cdot}0$–$0{\cdot}3$ at 300 K are in good agreement with the experimentally found $n_B$ values confirming the collinear spin ordering, while for $x = 0{\cdot}4$–$0{\cdot}9$ they clearly differ from the observed values (figure 4) indicating that significant canting exists on B-sites, suggesting magnetic structure to be non-collinear. Thus the change of spin ordering from collinear to non-collinear displays a strong influence on the variation of the saturation magnetic moment per molecule as observed by magnetization (figure 4) with chemical composition.

In order to confirm the presence of a canted spin (non-collinear) structure indirectly, we have recorded Mössbauer spectra at 12 K for typical samples $x = 0{\cdot}2$, 0·6, 0·8 and 0·9 as shown in figure 5 in addition to Mössbauer spectra taken at 300 K (figure 3). The spectra exhibit the coexistence of magnetic as well as very small paramagnetic component. The full lines in figure 5 correspond to the least squares fitted spectra using two magnetic sextets and a central doublet. The magnetic components, which are well resolved at these temperatures, have been assigned to magnetically ordered $Fe^{3+}$ ions at the tetrahedral (A) and octahedral (B) sites. The hyperfine fields along with isomer shifts obtained from Mössbauer data analysis are listed in table 2 as a function of $x$ for both A and B sites. Both hyperfine fields ($H_A$ and $H_B$) decrease with increasing $x$ demonstrating reduction in ferrimagnetic behaviour and magnetic coupling $J_{AB}$, with increasing $x$ values in agreement with magnetization results (table 3). Isomer shifts *IS* (A) and *IS* (B) show very little change with Mn-content. The quadrupole shift is absent for all Mn-contents.

An indirect check for the presence of a canted spin (non-collinear) structure follows from the apparent proportionality between $|H_n|$ and the average sublattice magnetization.

It can be shown that

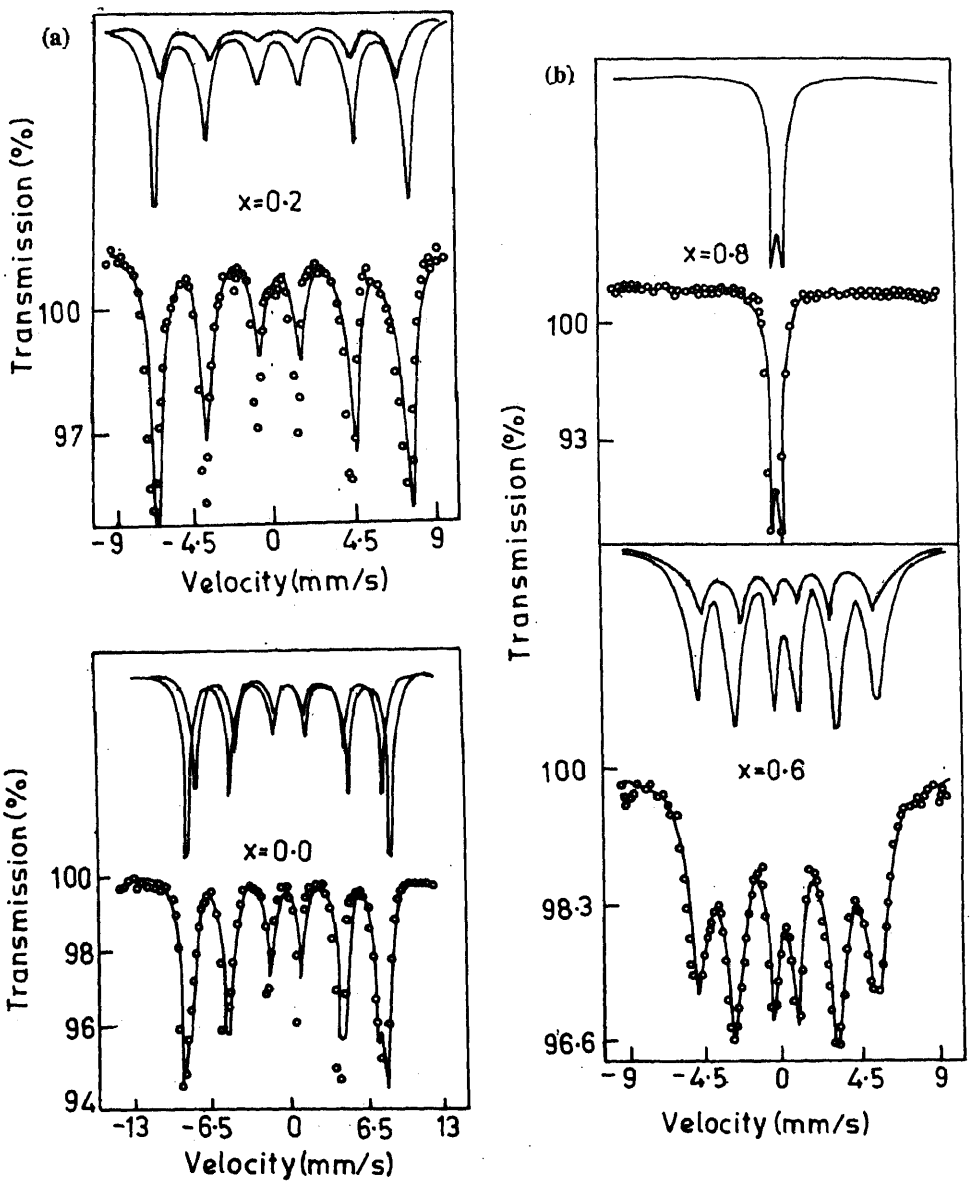

Figure 3. Typical Mössbauer spectra of Mg Mn Fe O taken at 300 K for (a) x = 0.0

$$\mu(x)=\frac{|H_{n_B}(x)|}{|H_{n_B}(o)|}\,M_B(x)-\frac{|H_{n_A}(x)|}{|H_{n_A}(o)|}\,M_A(x), \qquad (5)$$

where $\mu(x)$ is the magnetic moment per formula unit (3), and $|H_{n_B}(x)|$ and $|H_{n_A}(x)|$ are magnitudes of the average nuclear magnetic fields for the B and A sites, respectively. It is assumed that the relative saturation magnetization at 300 K is equal to $\mu(x)/\mu(0)$ at 12 K. The values of magnetic moment per formula unit $n_B^M(x)\approx\mu(x)$ as a function of $x$ were determined from (5) using the values of nuclear magnetic fields at 12 K from Mössbauer results (table 2) and the same are displayed in figure 4 and table 2. There is a reasonable agreement amongst the values of $n_B^M(x)$ obtained from Mössbauer data, $n_B(x)$ from magnetization measurements and $n_B^N(x)$ calculated from Neel's model as shown in figure 4 for $x=0{\cdot}0$ to $0{\cdot}2$ confirming collinear magnetic structure. Mössbauer data, $n_B^M(x)$, and $n_B^N(x)$ for $x\geq 0{\cdot}3$ clearly differ from magnetization data, $n_B(x)$, indicating that significant canting exists on B-site suggesting magnetic structure to be non-collinear.

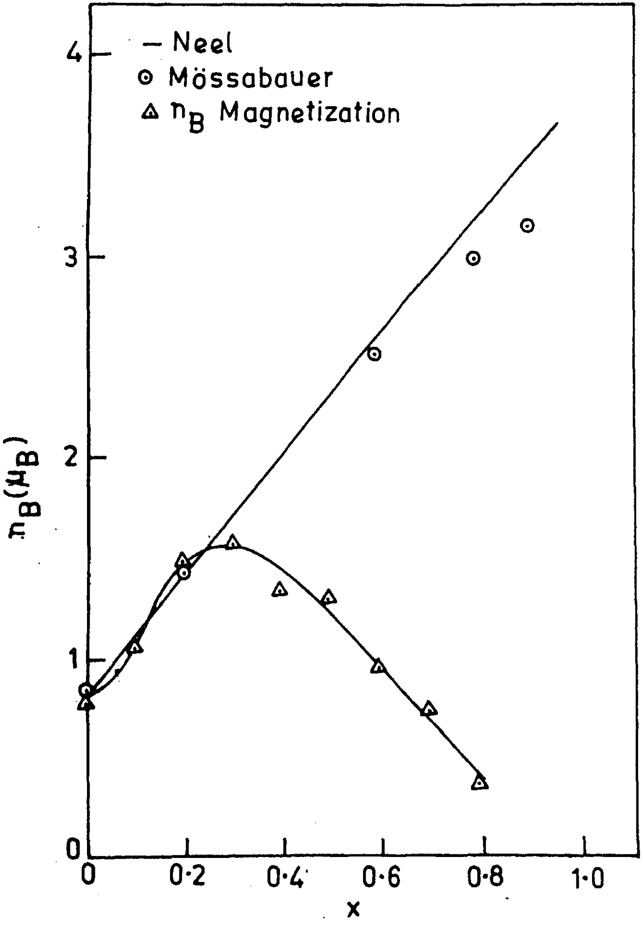

**Figure 4.** Variation of $n_B$ ($\mu_B$) with Mn concentration at 300 K for $Mg_{1+x}Mn_xFe_{2-2x}O_4$. The dots with circles represent the magnetic moment $n_B^M$ obtained from Mössbauer data and the triangles represent data from magnetization measurements. The solid line corresponds to Neel's model.

Adopting the procedure of Kulkarni and Patil (1982), the condition for the existence of YK angle can be found for $x>0{\cdot}3$, and the molecular field acting on various ions in the present system are given by

$$\begin{bmatrix} H_A(\mathrm{Fe})\\ H_{B1}(\mathrm{Mn})\\ H_{B1}(\mathrm{Fe})\\ H_{B2}(\mathrm{Mn})\\ H_{B2}(\mathrm{Fe})\end{bmatrix}=\begin{bmatrix}\lambda_{AA} & \alpha & \beta & \alpha & \beta\\ \alpha & \gamma' & \varepsilon' & \gamma & \varepsilon\\ \beta & \varepsilon' & \delta' & \varepsilon & \delta\\ \alpha & \gamma & \varepsilon & \gamma' & \varepsilon'\\ \beta & \varepsilon & \delta & \varepsilon' & \delta'\end{bmatrix}$$

$$\times\begin{bmatrix}(0{\cdot}92-x)\,m_A(\mathrm{Fe})\\ 1/2(x)m_{B1}(\mathrm{Mn})\\ 1/2(1{\cdot}08-x)\,m_{B1}(\mathrm{Fe})\\ 1/2(x)m_{B2}(\mathrm{Mn})\\ 1/2(1{\cdot}08-x)\,m_{B2}(\mathrm{Fe})\end{bmatrix}, \qquad (6)$$

where $H_A(\mathrm{Fe})$ is the molecular field acting on the $Fe^{3+}$ ion on the A-site due to all other ions, etc and

$$|m_A(\mathrm{Fe})|=|m_{B1}(\mathrm{Fe})|=|m_{B2}(\mathrm{Fe})|=5\mu_B,$$
$$|m_{B1}(\mathrm{Mn})|=|m_{B2}(\mathrm{Mn})|=3\mu_B,$$
$$m_{B1}\cdot m_A=-|m_{B1}|\,|m_A|\cos\alpha_{YK},$$
$$m_{B2}\cdot m_A=-|m_{B2}|\,|m_A|\cos\alpha_{YK},$$
$$m_{B1}\cdot m_{B2}=|m_{B1}|\,|m_{B2}|\cos 2\alpha_{YK}.$$

The molecular field constants are related to the following sets of interactions

$$\lambda_{AA}=\mathrm{A(Fe)}-\mathrm{A(Fe)},$$
$$\alpha=\mathrm{A(Fe)}-\mathrm{B_i(Mn)},$$
$$\beta=\mathrm{A(Fe)}-\mathrm{B_i(Fe)},$$
$$\gamma=\mathrm{B_i(Mn)}-\mathrm{B_2''(Mn)},$$
$$\gamma'=\mathrm{B_i(Mn)}-\mathrm{B_i(Mn)},$$
$$\delta=\mathrm{B_1(Fe)}-\mathrm{B_2(Fe)},$$
$$\delta'=\mathrm{B_i(Fe)}-\mathrm{B_i(Fe)},$$
$$\varepsilon=\mathrm{B_1(Fe)}-\mathrm{B_2(Mn)},$$
$$\varepsilon'=\mathrm{B_i(Fe)}-\mathrm{B_i(Mn)},$$

where $i=1,2$.

The part of the interaction energy involving YK angles may be written as

$$E(\mathrm{YK})=[15(0{\cdot}92-x)x\alpha+25(0{\cdot}92-x)\,(1{\cdot}08-x)\,\beta]$$
$$\times\cos\alpha_{YK}-1/4\,[9x^2\gamma+25(1{\cdot}08-x)^2\,\delta+30x$$
$$\times(1{\cdot}08-x)\,\varepsilon]\cos 2\alpha_{YK}. \qquad (7)$$

The energy is minimum for $\sin\alpha_{\mathrm{YK}} = 0$, which corresponds to Neel's configuration or for

$$\cos\alpha_{\mathrm{YK}} = \frac{15x(0{\cdot}92-x)\,\alpha + 25(0{\cdot}92-x)\,(1{\cdot}08-x)\beta}{9x^2\,\gamma + 25(1{\cdot}08-x)^2\,\delta + 30x(1{\cdot}08-x)\,\varepsilon}, \qquad (8)$$

which corresponds to the situation where the YK ordering is feasible. Here, for example the molecular field constant is related to the exchange integral $J_\alpha$ by

$$\alpha = \frac{2Z_{\mathrm{AB_i}}\,J[\mathrm{A(Fe)} - \mathrm{B_i(Mn)}]}{N_{\mathrm{B_i}}\,g_{\mathrm{A}}\,g_{\mathrm{B_i}}\,\mu_{\mathrm{B}}^2},$$

where $Z_{\mathrm{AB_i}}$, the number of $\mathrm{B_i}$ nearest neighbour to A, $N_{\mathrm{B_i}}$, the number of ions per formula unit, $\mu_{\mathrm{B}}$, the Bohr magneton and $g$ the Lande's splitting factor.

On physical grounds, it is expected that $J'_\gamma$, $J'_\delta$, $J'_\varepsilon$ will be close to $J_\gamma$, $J_\delta$ and $J_\varepsilon$, respectively, but they are not necessarily equal.

The molecular field constants can be obtained from the observed variation of the saturation magnetization with Mn concentration. The exchange constants so obtained should be consistent with the existing data on similar ferrimagnetic systems. Kulkarni and Patil (1982) have found $J_\alpha = -5{\cdot}25$ K for the $\mathrm{Cu_{1-x}Zn_xFe_2O_4}$ system, in the case of $\mathrm{Cu_{1-x}Zn_xFe_2O_4}$, $J_\alpha$ is the interaction between $\mathrm{A(Fe^{3+})}$ and $\mathrm{B_i(Cu^{2+})}$, in the present case it corresponds

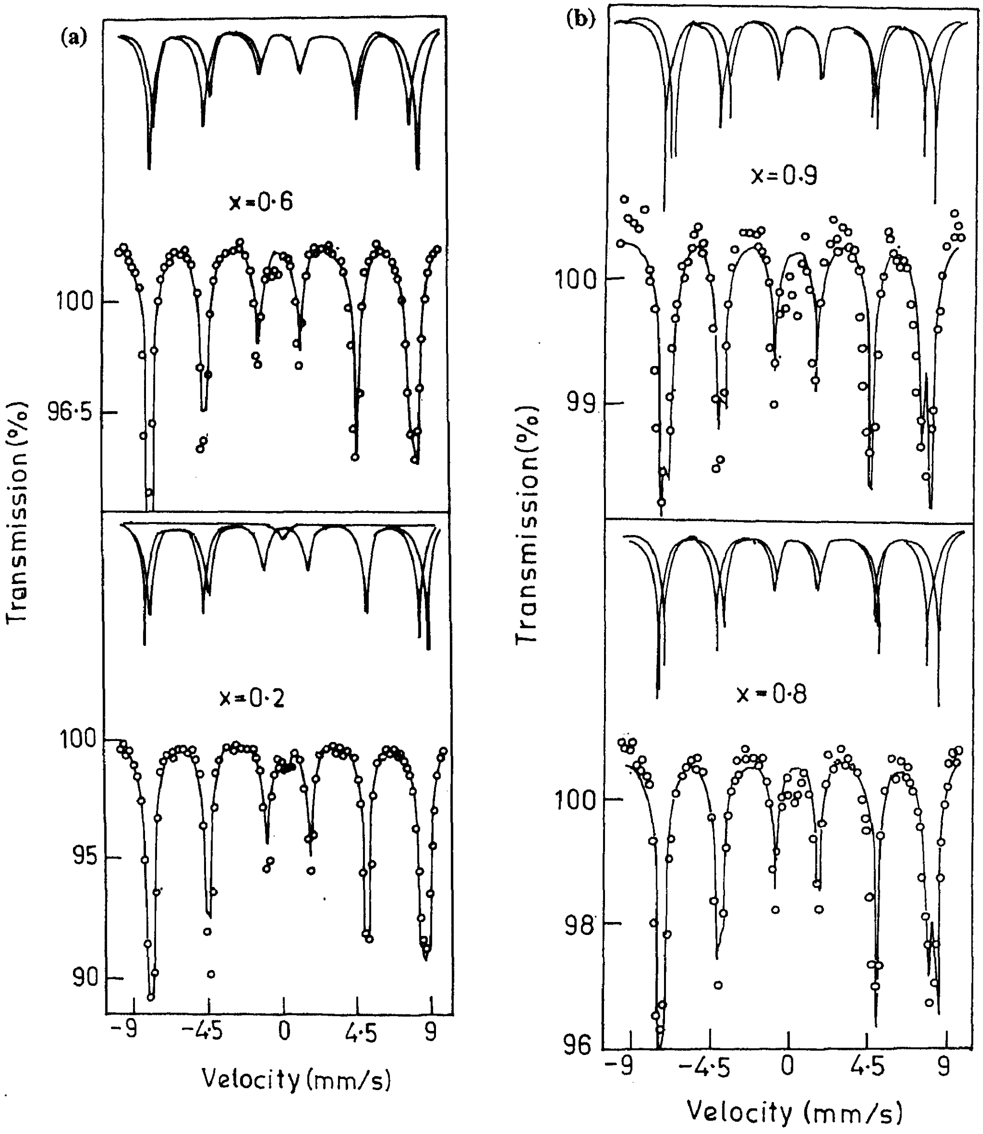

**Figure 5.** Typical Mössbauer spectra of $\mathrm{Mg_{1+x}Mn_xFe_{2-2x}O_4}$ taken at 12 K for (**a**) $x = 0{\cdot}2$, 0·6 and (**b**) 0·8, 0·9.

to the interaction between A($Fe^{3+}$) and $B_i$($Mn^{4+}$). Assuming $J_\alpha$ is approximately equal to the product of the moments of the ions, one gets $J_\alpha(Fe^{3+}-Cu^{2+}) = -5$ K and $J_\alpha(Fe^{3+}-Mn^{4+}) = -15$ K. The value of $J_\alpha = -5$ K compares reasonably well with $J_\alpha = -5{\cdot}25$ K value of Kulkarni and Patil (1982) for $Cu_{1-x}Zn_xFe_2O_4$. So $J_\alpha = -14$ K and $J_\beta = -13$ K values are accepted for $Mg_{1+x}Mn_xFe_{2-2x}O_4$. In a similar fashion the values of $J_\delta$, $J_\gamma$ and $J_\varepsilon$ have been estimated as $J_\delta = -10$ K, $J_\gamma = -4{\cdot}5$ K and $J_\varepsilon = -7{\cdot}5$ K. The values of the exchange constants used in calculating Yafet–Kittel angles, $\alpha_{YK}$ from (8) are listed in table 3 along with $\alpha_{YK}$ values.

The experimental values of $\alpha_{YK}$ have been obtained from the observed variation of $n_B$ with $x$ using the relation

$$n_B(x) = M_B(x)\cos\alpha_{YK} - M_A(x). \tag{9}$$

These values have also been given in table 3. There is a satisfactory agreement between the experimental and theoretical values of $\alpha_{YK}$. Thus the observed variations of the saturation magnetization has been explained on the basis of the existence of Yafet–Kittel angles on the B-site spins. This suggests that A–B and B–B superexchange interactions are comparable in strength.

## Acknowledgements

The authors are thankful to Prof. P Boolchand, University of Cincinati, USA for low temperature Mössbauer facilities and also Drs G J Baldha, D G Kuberkar for fruitful discussions.

## References

Bhargava S C and Zeeman N 1980 *Phys. Rev.* **B21** 1717

Brand R A, Georges-Gilbert H, Hubsch J L and Heller J A 1985 *J. Phys.* **F15** 1987

Buerger M J 1960 *J. crystal structure analysis* (New York: John Wiley)

Chakravarthy R, Madhav Rao L, Paranjpe S K, Kulshreshta S K, Sopen A K and Howells W S 1988 *J. Phys. (Paris) Colloq.* **49** C8–1111

Dormann J L 1980 *J. Phys. (Paris) Colloq.* **41** 175

Dormann J L and Reneudin P 1980 *Proc. int. conf. on ferrites, Japan* p. 156

Dormann J L and Nogues M 1990 *J. Phys. Condense Matter* **2** 1223

Dormann J L, Harfaouni M E I, Nogues M and Love J 1987 *J. Phys.* **C20** L161

Goodenough J B 1963 *Magnetism of the chemical bond* (New York: John Wiley)

Jani N N, Trivedi B S, Joshi H H and Kulkarni R G 1997 *Hyperfine interactions* (Netherlands: J. C. Baltzer AG, Science Publishers) **110** pp 227–237

Jotania R B, Upadhyay R V and Kulkarni R G 1992 *IEEE Trans. magn.* **28** 1889

Kulkarni R G and Patil V U 1982 *J. Mater. Sci.* **17** 843

Muralidharan K, Srivastava J K, Moratha V R and Vijayaraghavan R 1985 *J. Phys.* **C18** 5897

Neel L 1950 *C. R. Acad. Sci. Paris* **230** 375

Radhakrishnamurthy C, Likhite S D and Sastry N P 1971 *Philos. Mag.* **23** 503

Satyamurthy N S, Natera M G, Yousuf S I, Begum R J and Srivastava C M 1969 *Phys. Rev.* **181** 4412

Bull. Mater. Sci., Vol. 21, No. 3, June 1998, pp. 241–245. © Indian Academy of Sciences.

# Fracture toughness correlation with microstructure and other mechanical properties in near-eutectoid steel

**K V SUDHAKAR* and G S MURTY**

Department of Materials and Metallurgical Engineering, Indian Institute of Technology, Kanpur 208 016, India
*Present address: Department of Metallurgy, Indian Institute of Science, Bangalore 560 012, India

MS received 9 May 1997; revised 16 April 1998

**Abstract. The variation of yield strength and fracture toughness was investigated for four different heat treatments attempted on specimens of a near-eutectoid steel. The aim of this study was to optimize the microstructure for simultaneous improvements in strength and toughness. Further, the fracture toughness deduced through empirical relations from tensile and charpy impact tests was compared with those measured directly according to ASTM Designation: E 399. Among the four different heat treatments attempted in this study, the plane strain condition was valid in the fracture toughness tests for (i) normalized and (ii) hardened and tempered (500°C for 1 h) treatments only. The latter of the two heat treatments resulted in simultaneous improvement of strength and plane strain fracture toughness. The finely-dispersed carbides seem to arrest the crack propagation and also increase the strength. The pearlitic microstructure of the former leads to easy crack propagation along cementite platelets and/or cementite/ferrite interfaces. The nature of variation of empirically determined toughness values from tensile tests for different heat treatments is similar to that measured directly through fracture toughness tests, although the two sets of values do not match quantitatively. On the other hand, the toughness data deduced from charpy impact test is in close agreement with that evaluated directly from fracture toughness tests.**

**Keywords. Fracture toughness; near-eutectoid steel; mechanical properties; heat treatment.**

## 1. Introduction

One of the requirements of designing engineering structures is to enhance the load-bearing capacity without plastic yielding of the components. At the outset, it may appear that an increase in yield stress would meet this requirement. But it is not so because of increasing danger of brittle fracture in high strength materials. Simultaneous improvements in yield strength and fracture toughness are needed rather than either of them. While continuum mechanics is the basis of structural design, the control of mechanical properties of structural materials is in the realm of materials science requiring an understanding of the structure–property relations. Fracture toughness being a more complex property than the yield strength, the crucial issue requiring understanding is the effect of microstructure on crack propagation. This will provide solutions to problems like: (i) a systematic development of tougher alloys (alloy design), (ii) the inverse relationship between strength and toughness of a material, (iii) effect of heat treatment on toughness, and (iv) non-unique relation between strength and toughness. The variation in strength and fracture toughness for different microstructures in a near-eutectoid steel has been explored in this study. Further, the correlation between the fracture toughness measured directly and that deduced indirectly from other mechanical properties (obtained from tensile and impact tests) was also examined. The simpler test results may be availed to assess fracture toughness through such correlations.

## 2. Experimental

### 2.1 *Materials and heat treatment*

The chemical composition of the near-eutectoid steel used in this study is shown in table 1. Starting with hot-rolled plate of 12·5 mm thickness, various specimens for charpy, tensile and fracture toughness tests were machined according to the dimensions specified in figures

**Table 1.** Chemical composition of near-eutectoid steel.

| Element | C | Si | Mn | S | P | Fe |
|---|---|---|---|---|---|---|
| %Wt | 0·64 | 0·40 | 0·75 | 0·014 | 0·014 | Balance |

1a–c. These specimens were coated with a ceramic slurry prior to heat treatment in order to minimize oxidation and decarburization. Four different heat treatments were attempted on these specimens in such a way that their strength and toughness varied with some overlap in their range. The heat treatment schedules for this purpose were selected from ASM handbook (from the listed properties for different heat treatments). The details of the adopted heat treatments are mentioned in table 2.

### 2.2 *Fracture toughness test*

The fracture toughness tests were performed according to ASTM standard E399-83. Fatigue precracking and fracture toughness tests were carried out on an MTS 810 machine using three point bend test specimens.

Fatigue precracking was carried out by cyclically loading the notched specimens at a load ratio of 0·1 in load control mode. The maximum load of the fatigue cycle was chosen in such a way that the maximum stress intensity factor did not exceed 80% of the anticipated plane strain fracture toughness ($K_{IC}$) in each case. The precracked specimens were loaded monotonically in stroke controlled mode till fracture. From the recorded load versus crack opening displacement (COD) data, the apparent fracture toughness ($K_Q$) was calculated using the relation:

$$K_Q = [P_Q S/BW^{3/2}] f(a/W), \tag{1}$$

where $P_Q$ is the load corresponding to 2% crack extension (obtained through the intersection of 5% secant line), $S$ the span length, $B$ the thickness, $W$ the specimen width, $a$ the crack length and $f(a/W)$ is the specimen geometry and crack length related correction factor (known as Y factor), which is obtained analytically from the appropriate relations (ASTM E399; Provan 1988). The validity of plane strain condition is assessed by comparing the specimen thickness with $2{\cdot}5\,(K_Q/\sigma_{YS})^2$, where $\sigma_{YS}$ is the 0·2% yield stress in uniaxial tension.

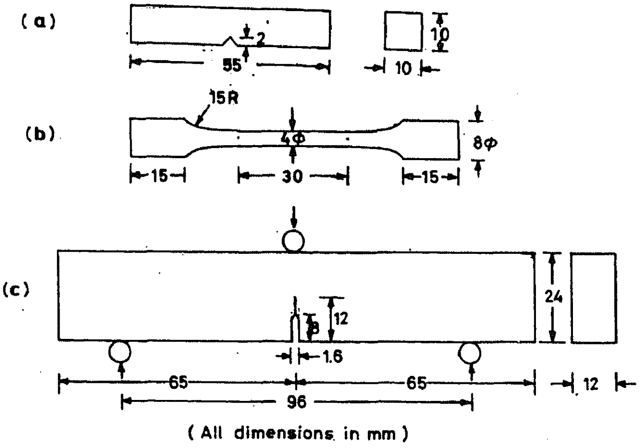

**Figure 1.** (a) Charpy test specimen, (b) tensile test specimen and (c) three-point bend test specimen.

### 2.3 *Charpy and tensile tests*

The impact energy $C_v$ (energy/unit area) of the standard charpy impact test is converted to equivalent $K_Q/K_{IC}$ making use of an empirical relation (Rolfe and Novak 1970):

$$K_{IC}^2/E = 0{\cdot}22\,(C_v)^{1{\cdot}5}, \tag{2}$$

where $E$ is the elastic modulus in MPa, $K_{IC}$ the plane strain fracture toughness in MPa$\sqrt{m}$, $C_v$ the charpy energy in MPa.m and the units of the constant are $[1/\text{MPa.m}]^{0{\cdot}5}$. Standard tensile tests were also performed on differently heat treated specimens using an Instron testing machine. Equivalent $K_{IC}$ values were deduced through an empirical relation (Hahn and Rosenfield 1968):

$$K_{IC} = n\,(2E\,\sigma_{YS}\,\varepsilon_f/3)^{1/2}, \tag{3}$$

where $n$ is the strain hardening exponent and $\varepsilon_f$ the fracture strain in uniaxial tension.

## 3. Results and discussion

### 3.1 *Strength and fracture toughness*

The tensile stress–strain curves and typical load-displacement (COD) curves of precracked specimens in fracture toughness tests are presented in figures 2 and

**Table 2.** Tensile test data of heat treated specimens.

| Sl no. | Heat treatment$^+$ | 0·2% YS (MPa) | UTS (MPa) | Elong. (%) | RA (%) | Equivalent fracture toughness $K_{IC}^*$ (MPa $\sqrt{m}$) |
|---|---|---|---|---|---|---|
| 1. | Normalized | 700 | 1060 | 19·1 | 36·0 | 30·2 |
| 2. | Oil hardened and tempered at 680°C for 1 h | 700 | 780 | 23·8 | 58·4 | 41·2 |
| 3. | Furnace cooled | 520 | 912 | 23·8 | 36·7 | 34·2 |
| 4. | Oil hardened and tempered at 500°C for 1 h | 1464 | 1568 | 7·2 | 16·7 | 38·7 |

*Obtained from equation (3); $^+$all austenitized at 860°C.

3, respectively. The tensile yield strength and fracture toughness ($K_Q$) data of differently heat treated specimens are given in tables 2 and 3. It is seen that the yield strength of normalized specimen and that tempered at 680°C for 1 h is the same. The specimen tempered at 500°C for 1 h exhibited the highest yield strength among all the heat treated specimens. It is well known that in a hardened steel, when heated successively to higher temperatures above room temperature, submicroscopic particles of cementite are formed through the gradual loss of excess carbon in martensite. With continued heating, the particles of cementite grow in size by a process of coalescence and growth. This coalescence is more pronounced at higher tempering temperature. The

**Table 3.** Fracture toughness test data of heat treated specimens.

| Sl no. | Heat treatment⁺ | Crack length $a$ (mm) | $P_{max}/P_Q$ | Fracture toughness ($K_Q$) (MPa$\sqrt{m}$) | 0·2% YS (MPa) from tensile test |
|---|---|---|---|---|---|
| 1. | Normalized | 12·02 | 1·10 | 47·5 | 700 |
| 2. | Oil hardened and tempered at 680°C for 1 h | 12·08 | 1·09 | 84·7 | 700 |
| 3. | Furnace cooled | 11·96 | 1·00 | 55·2 | 520 |
| 4. | Oil hardened and tempered at 500°C for 1 h | 12·06 | 1·01 | 69·0 | 1464 |

⁺All austenitized at 860°C.

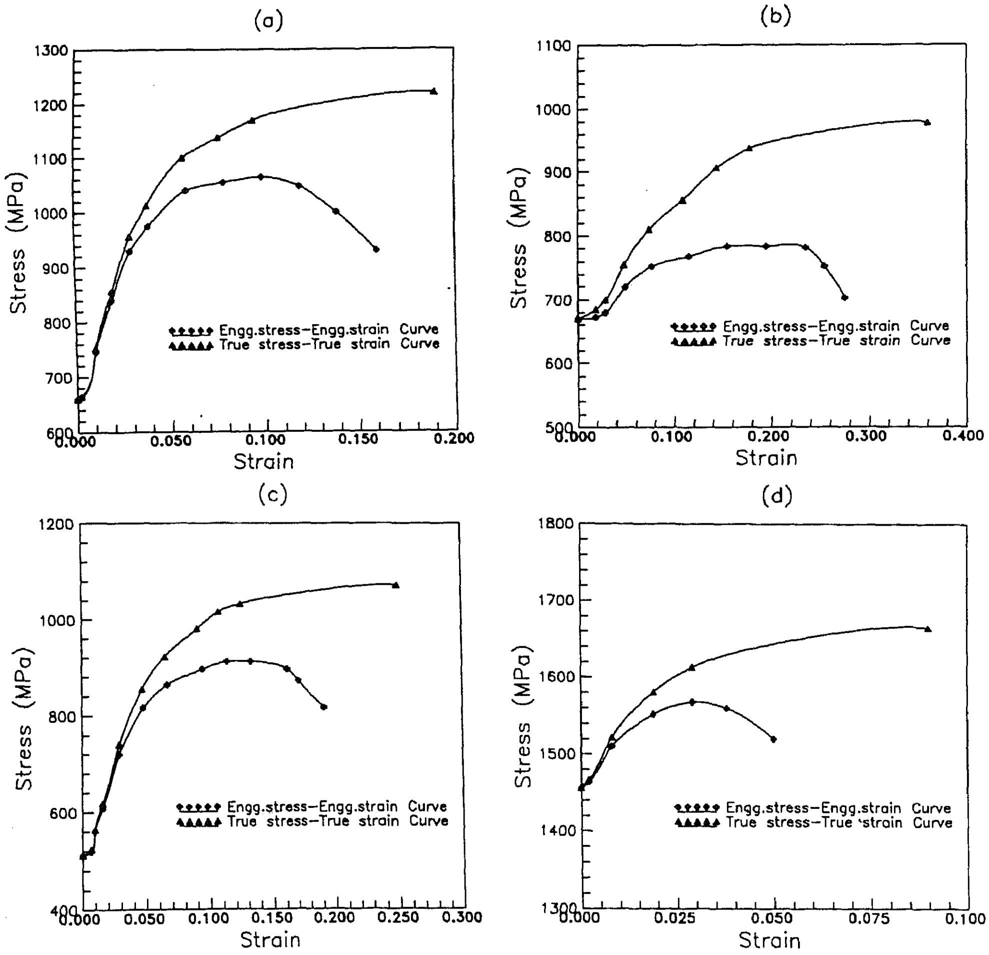

**Figure 2.** Tensile stress–strain curves for near-eutectoid steel: (**a**) Normalized, (**b**) hardened and tempered at 680°C for 1 h, (**c**) furnace cooled and (**d**) hardened and tempered at 500°C for 1 h.

dispersion strengthening effect of particles depends on their size and spacing. The coarsening of cementite particles causes a softening of the steel at higher tempering temperature as seen in the case of treatment 2 (tempering at 680°C for 1 h). On the other hand, higher strength obtained for treatment 4 (tempering at 500°C for 1 h) results from the ultrafine cementite particles.

The true stress–true strain curves of samples subjected to different heat treatments are shown in figure 2 and it may be noted that the true stress–true strain values of the last point of these stress–strain curves are based on the percent reduction in area at fracture. On checking the validity of plane strain condition in fracture toughness tests, the plane strain condition is valid only for the normalized (treatment 1) and tempered at 500°C for 1 h (treatment 4) cases. For fracture toughness tests involving the other two heat treatments, the condition of plane strain is not valid. Thus quantitative comparison of fracture toughness is possible for treatments 1 and 4 only but not for 2 and 3. Considering the treatments 1 and 4, the yield strength of the tempered (500°C) specimen is nearly twice that of the normalized one. It can be noted that despite the increase in strength, the fracture toughness of tempered (500°C for 1 h) specimen is significantly higher than that of normalized one. Thus the tempered (500°C for 1 h) specimen exhibits simultaneous increase in strength and toughness relative to the normalized treatment. The usual inverse relation between strength and toughness is not applicable while comparing the properties arising from these heat treatments. The higher toughness of the tempered (500°C

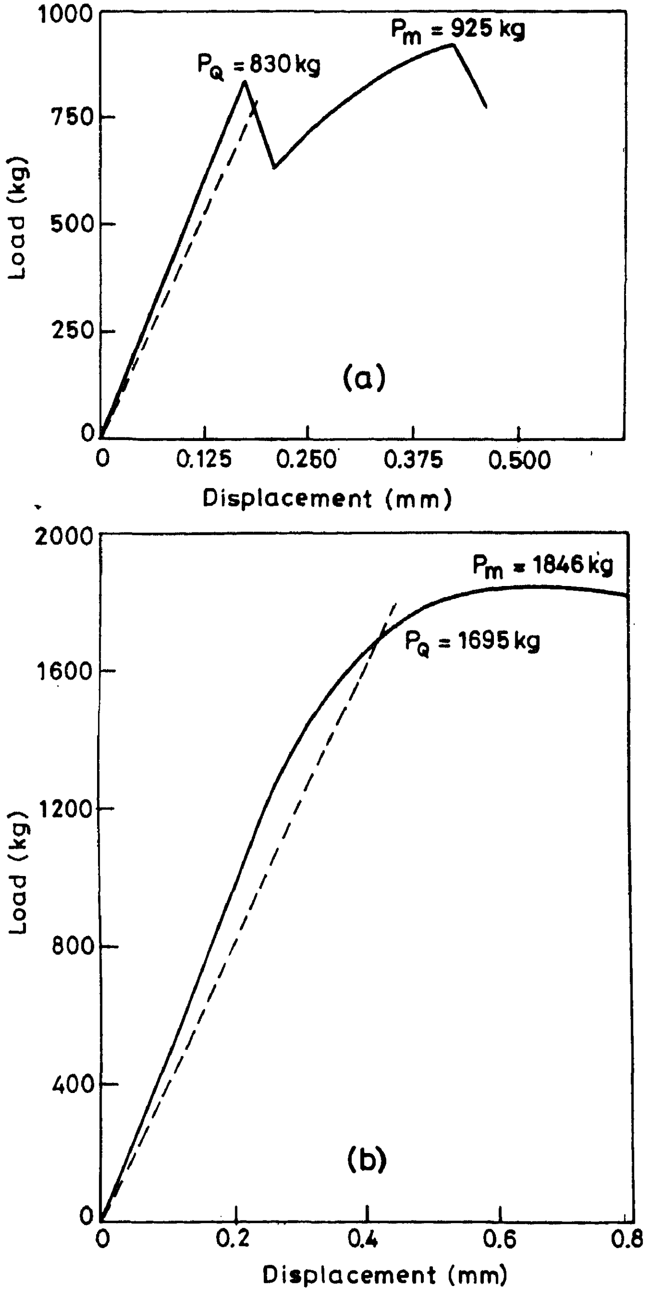

**Figure 3.** Typical load-displacement (COD) curves for near-eutectoid steel: (**a**) Normalized and (**b**) hardened and tempered at 680°C for 1 h.

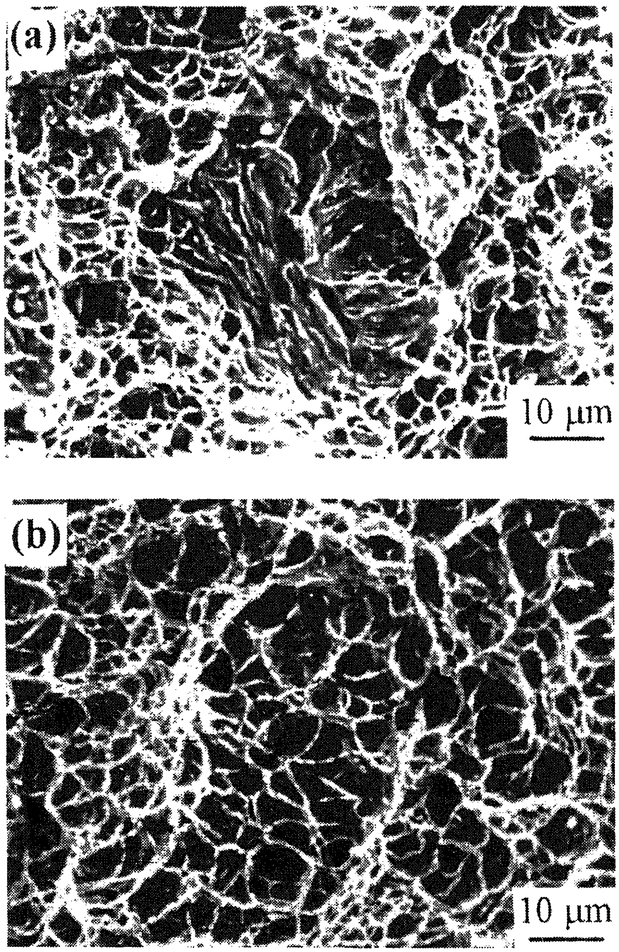

**Figure 4.** Typical SEM fractographs for near-eutectoid steel: (**a**) Normalized and (**b**) hardened and tempered at 680°C for 1 h.

**Table 4.** Charpy test data of heat treated specimens.

| Sl no. | Heat treatment$^+$ | Charpy energy ($C_v$) (J/cm$^2$) | Charpy energy ($C_v$) (MPa·m) | Equivalent $K_{IC}^*$ (MPa $\sqrt{m}$) |
|---|---|---|---|---|
| 1. | Normalized | 13·6 | 0·136 | 48 |
| 2. | Oil hardened and tempered at 680°C for 1 h | 44·7 | 0·447 | 117 |
| 3. | Furnace cooled | 16·3 | 0·163 | 55 |
| 4. | Oil hardened and tempered at 500°C for 1 h | 21·7 | 0·217 | 68 |

$^+$Obtained from equation (2); $^+$all austenitized at 860°C.

for 1 h) specimen follows from the tempered martensitic structure. The carbides are expected to be mostly spherical in shape and they arrest the crack propagation through their fine distribution. On the other hand, the normalized treatment results in pearlitic structure. In this case the cementite platelets and/or cementite–ferrite interfaces provide easy path for crack propagation (Curry and Knott 1978; Porter *et al* 1978; Rama Rao 1978). Thus the tempered martensitic structure provides strengthening through the presence of ultrafine particles of cementite in ferrite and better toughness because the finely-dispersed carbides arrest crack propagation.

Fractographic observations of normalized and furnace cooled specimens indicate the presence of quasi-cleavage facets and dimples (figure 4a). A change in plane of fracture from one grain to the other can also be noted in the cleavage dominated regions. The path of the main crack might have been the cementite platelets or the interface between cementite and ferrite lamellae of the pearlitic microstructure. These easy paths of cleavage fracture lead to low value of fracture toughness.

In the tempered steels, fracture occurred predominantly by nucleation, growth and coalescence of voids. Microvoids are usually initiated at oxide and sulphide inclusions, carbides and other imperfections. The carbide particles assist the void formation by providing weak interfaces which separate in tensile loading. The particles may also fracture and the fractured parts move apart by plastic flow of the matrix. The individual voids thus formed join together by local necking of ligaments between the voids and there is some plastic flow before fracture occurs. This process is associated with more energy absorption and, thus, a higher toughness.

### 3.2 *Correlation between fracture toughness and other mechanical properties*

The estimates of $K_{IC}$ from the tensile and impact test data are shown in tables 2 and 4, respectively. Considering the toughness estimates from tensile tests, one to one correlation is not seen between them and the apparent toughness ($K_Q$) measured directly. However, the trends of change in toughness with heat treatment are similar. On comparing the $K_Q$ data obtained from fracture toughness tests with those estimated from the impact energy values, good quantitative agreement can be noted between them.

## 4. Conclusions

(I) From a comparison between yield strength and fracture toughness of specimens with similar microstructures, the toughness is seen to decrease with the increase in strength. (II) The hardened and tempered (500°C for 1 h) treatment results in two-fold increase in strength with a significant increase in fracture toughness relative to the normalized one. The fine particles of cementite in ferrite cause strengthening and also arrest the crack propagation and thereby enhance the fracture toughness. On the other hand, the pearlitic microstructure is of lower strength and it provides easy paths for crack propagation along the cementite platelets and/or cementite/ferrite interfaces. (III) The variation in fracture toughness values deduced indirectly from tensile tests follow the same qualitative trend as those directly measured for different heat treatments, but the two sets of values differ from each other. On the other hand, the fracture toughness data obtained from charpy tests is in closer agreement with that measured directly for different heat treatments.

## References

Curry D A and Knott J F 1978 *Metal Sci.* **8** 511
Hahn G T and Rosenfield A R 1968 *ASTM STP* **432** 5
Porter D A, Easterling K E and Smith G D W 1978 *Acta Metall.* **26** 1405
Provan J W 1988 *J. Mater. Edu.* **10** 325
Rama Rao P 1978 *Trans. Indian Inst. Metals* **31** 239
Rolfe S T and Novak S R 1970 *ASTM STP* **463** 124

Bull. Mater. Sci., Vol. 21, No. 3, June 1998, pp. 247–249. © Indian Academy of Sciences.

# Surface hardening of oil-hardened nonshrinking steel using ruby laser

A RAMALINGAM*, B J KALAISELVI[†], S SRIDHARAN[‡], P K PALANISAMY and V MASILAMANI

Department of Physics, Anna University, Chennai 600 025, India
[†] Department of Physics, Pondicherry Engineering College, Pondicherry 605 014, India
[‡] Engine Valves Limited, Chennai 600 016, India

MS received 26 August 1997; revised 24 March 1998

**Abstract.** Surface modification of metals and alloys using lasers has acquired considerable importance because the changes achieved are highly localized and superficial. In this process the mechanical and structural properties of the bulk are retained as such because of the high temperature gradient and high rate of change of temperature that are unattainable by conventional methods. The present report is on surface hardening of oil-hardened nonshrinking (OHNS) steel using Ruby laser in normal mode. It is found that surface hardening increases thrice the size of base material and the microstructure of the laser-heated zone changes from pearlite phase to martensite phase.

**Keywords.** OHNS steel; ruby laser; surface hardening; material processing; Pearlite phase; Martensite phase.

## 1. Introduction

Heat treatment of materials by lasers gains popularity because specific region with pre-determined phase changes could be achieved. Various authors have studied surface hardening of steels of different compositions and grades, employing continuously working (CW) and pulsed lasers (Avner 1974; Gnanamuthu 1979; Hugel 1988; Lampman 1981). Markarov *et al* (1989) studied the influence of laser and electron beam treatments on the structure transformations and abrasive wear resistance of hardened steel 20KHN3A which is widely used in the manufacturing of drilling bits and other components operating under conditions of high contact loads using CW $CO_2$ laser. Bradley (1988) theoretically studied the hardened depth obtained by scanning steel surfaces with a laser beam. The calculated depth of hardening was found to be in agreement with experimental results for three steels processed with a $CO_2$ laser. Laser surface hardening of ferrous materials is a process used to improve the mechanical properties of highly stressed machine and tool parts. In this process only a thin layer of the surface is heated to austenization temperature prior to quenching leaving the interior of the work piece unaffected. If the power density of the laser beam is high, heat is generated at the surface at a rate higher than the heat conducted to the interior parts of the material and within a short duration the thin surface layer will reach austenizing temperature whereas the interior of the workpiece will be at its initial temperature. Laser transformation hardening of steel is currently employed in many automobile and tool industries because of its technical advantages over the flame and induction hardening. It gives minimum distortion, ability to harden localized and inaccessible areas, high-speed processing and improved mechanical properties such as hardness, fatigue and wear resistance. Oil-hardened nonshrinking (OHNS) steel which comes under tool steel is widely used in manufacturing tools for machining and gauging such as machine screw taps, threading dies, chasers and milling cutters. Studying the surface hardening of this steel using ruby laser will be useful for manufacturing industries. The present report is on surface hardening of OHNS steel using a Ruby laser in normal mode.

## 2. Experimental

The material chosen for the study was OHNS steel, which covers under dimensionally stable steels. The percentage of carbon and its alloys in OHNS steel are: carbon, 0·95%; chromium, 0·5%; V, 0·15%; W, 0·6% and the rest is iron. The properties of OHNS steels are given in table 1. The microstructure of the specimen (parent material) is pearlitic and its microhardness 280 VHN. This material is useful for threading tools of all types, such as machine screw taps, threading dies, milling cutters, wood working tools and gauges.

---

*Author for correspondence

The specimen were cut into blocks of 5 × 3 × 1 cm and the roughly cut surfaces of the specimen are ground in the grinding wheel. The surface was polished by using polishing papers and alumina. The papers used for polishing are given in the increasing order. Rough polishing, 120, 220, 400, 600; fine polishing, 1/0, 2/0, 3/0, 4/0, and alumina polishing is done on the specimen using rotary wheel. The sample is etched using ferric chloride to obtain the clear grain boundaries.

The hardness of the base material is measured using Shimadzu micro hardness tester (load 200 g) and found to be 280 VHN. The sample was heat treated by using Ruby laser (Laser applications, Inc., Model No. 933R 3L-2) of wavelength 694·3 nm, pulse width 300 $\mu$s, output energy 1·5 J, beam divergence 1 mrad and one pulse per min. The specimen is fixed in an optical upright which has vertical, horizontal as well as front and back movements. The laser beam was focussed by a glass lens of focal length 30 cm and the depth of focus was so adjusted that there was intense heating, but below melting or vapourization. If the laser beam is focussed it causes pitting of the sample. To avoid this the distance between the specimen and the lens are adjusted by trial and error method. The specimen is coated with carbon soot to avoid reflection of the incident radiation. The optimum range of the coating thickness is found to be 0·05 mm to 0·1 mm. 2 mW He–Ne laser is used for alignment. The sample is irradiated by Ruby laser with one pulse per min, and the hardness was measured. The diameter of the irradiated beam on the specimen is 0·5 mm. Experiments were repeated seven times. The microhardness for different laser shots are measured. The hardness at the edges (0·2 mm from the centre) and at the centres for different shots are measured and these values are given in table 2. The values show that the hardness is maximum at the centre and decreases at the edges. It may be due to the gaussian distribution of the beam profile. The maximum value of microhardness is found to be 946 VHN which shows that the hardness is about three times more than the hardness of the base material. Different laser shots are superimposed on the same spot and the microhardness was measured and the values are shown in table 3. The hardness is increased by three times for the first shot and after that the hardness slowly increases.

**Table 1.** Properties of OHNS steel.

| | |
|---|---|
| Thermal conductivity (K) | 24·27 Wm$^{-1}$ k$^{-1}$ |
| Thermal diffusivity (k : K/pC) | 6·687 × 10$^{-6}$ m$^2$/s |
| Emissivity | 0·8 |
| Microhardness | 280 VHN |
| Density ($\rho$) | 8670 kg/m$^3$ |
| Specific heat capacity (C) | 418·6 J/kg/k |
| Microstructure present | Pearlite structure |

**Table 2.** Microhardness at different distances.

| | Microhardness (VHN) | | |
|---|---|---|---|
| Sl. No. | Edge | Centre | Edge |
| 1 | 560 | 840 | 665 |
| 2 | 569 | 927 | 680 |
| 3 | 532 | 946 | 610 |
| 4 | 520 | 908 | 670 |
| 5 | 543 | 892 | 603 |

**Table 3.** Microhardness for number of superimposed laser shots.

| No. of shots (superimposed) | Microhardness (VHN) |
|---|---|
| Base metal | 280 |
| 1 | 790 |
| 2 | 820 |
| 3 | 840 |
| 4 | 850 |
| 5 | 857 |

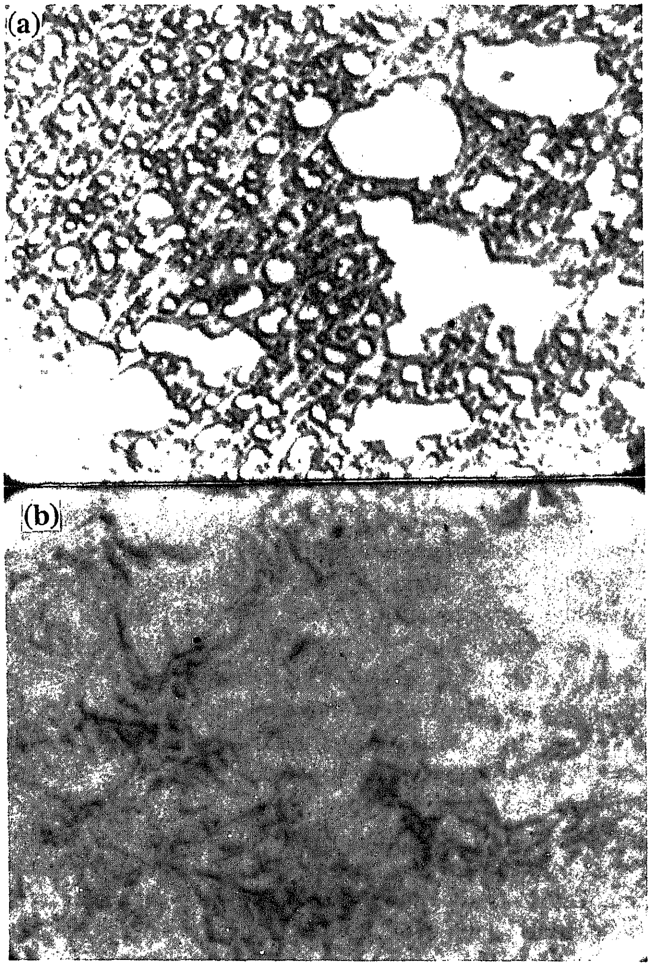

**Figure 1.** Microstructure of **a.** unhardened and **b.** hardened zones.

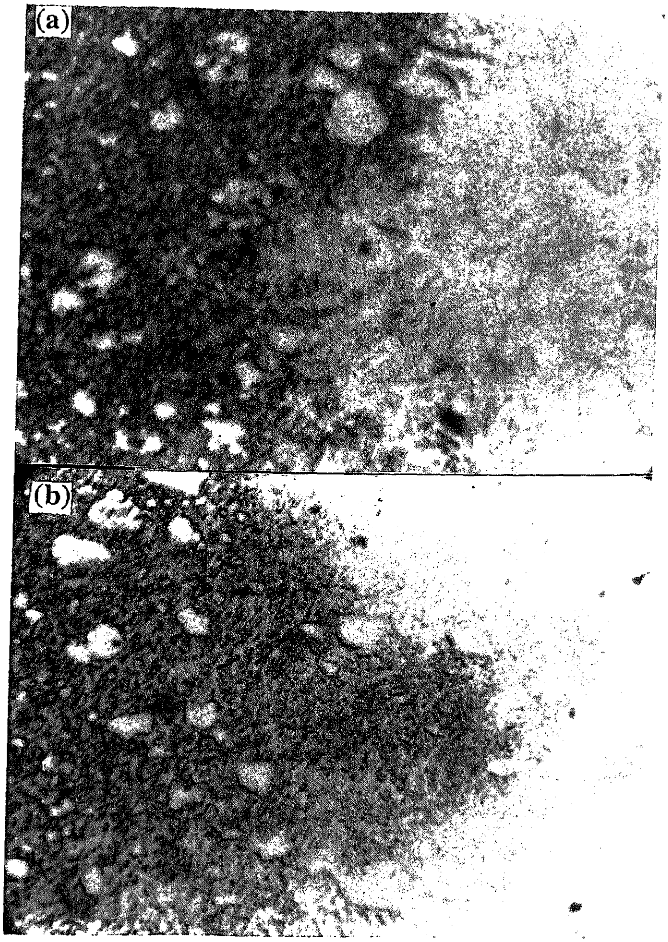

**Figure 2.** **a–b**. Microstructure of hardened–unhardened zones.

The laser-treated surface is observed through optical microscope with magnification 200× and it was found that the hardened surface has martensite phase whereas the microstructure of the parent material is pearlite phase which are shown in figures 1a and b respectively. The interface between the hardened and unhardened zones are shown in figures 2a and b.

The surface temperature, $T$ of the specimen is calculated using the formula (Rykalin *et al* 1988):

$$T = 2EPkt/AK,$$

where, $E$ is the emissivity, $P$ the power, $k$ the thermal diffusivity, $t$ the interaction time of laser, $A$ the area and $K$ the thermal conductivity.

The hardened depth is found by using the expression (Rykalin *et al* 1988):

$$Z = (4at/\pi)^{1/2}\ (T_m - T_n)/T_m\,,$$

$a$ is the beam diameter, $T_m$ and $T_n$ are the melting and hardening temperatures, respectively.

The surface temperature and hardened depth are calculated and the values are 872°C and 40 $\mu$m, respectively.

## 3. Conclusion

The microhardness of the base material is 280 VHN. The hardness obtained by furnace hardening is 680 VHN. By using ruby laser the maximum hardness achieved is 946 VHN. The laser heat treatment increased the hardness of the specimen to a larger extent. The comparison of microstructure of the laser-heated and unheated region showed a clear difference of pearlite and martensite matrices and the transition between the hardened and unhardened region was also observed. This study has showed the technical feasibility of laser surface hardening treatment to improve the wear resistance of parts of ring gear and engine valves without affecting the interior parts.

## References

Avner S H 1974 *Physical metallurgy* (New Delhi: Tata McGraw-Hill)

Bradley J R 1988 *J. Phys. D: Appl. Phys.* **21** 834

Gnanamuthu D S 1979 *Laser surface treatment in application of lasers in material processing, Proc. Conf. Washington DC* (Ohio: ASM)

Hugel H 1988 *Lasers in manufacturing* (New York: Springer-Verlag)

Lampman 1981 *Introduction of surface hardening of steels* (Ohio: ASM International) **5** p. 259

Markarov A V, Korshunov L G, Chernenko N L, Koval N N, Kreyndel Yu Ye, Osipov I V and Chuprakova I Yu 1989 *Phys. Met. Metall.* **68** 123

Rykalin N, Uglov A, Zuev I and Kokora A 1988 *Laser and electron beam material processing* (Moscow: Mir Publications)

# An experimental setup for dynamic measurement of magnetoelectric effect

M MAHESH KUMAR, A SRINIVAS, S V SURYANARAYANA*, G S KUMAR and T BHIMASANKARAM
Department of Physics, Osmania University, Hyderabad 500 007, India

MS received 13 October 1997; revised 17 February 1998

**Abstract.** An experimental setup is developed for the measurement of dynamic magnetoelectric effect (ME) in polycrystalline materials, using a time varying DC magnetic field on which an AC magnetic field is superimposed. The experimental data on ME on $Bi_5FeTi_3O_{15}$ and a solid solution of (90%)$BiFeO_3$–(10%)$BaTiO_3$ are obtained using this setup. The linear and higher order ME coefficients can be evaluated from the output voltage. The temperature variation of ME data gives additional information corroborating with the data on magnetization.

**Keywords.** Dynamic magnetoelectric effect; ferroelectricity; bismuth layer structured ferroelectrics.

## 1. Introduction

The magnetoelectric effect (ME) in an insulator is the electrical polarization on applying DC or AC magnetic field $(ME)_H$ or the magnetic polarization on the application of DC or AC electric field $(ME)_E$. It occurs due to the interaction between the magnetic and electric dipoles. The condition for the realization of ME output is that there should exist electrical and magnetic ordering in the material at a given temperature and also that the electrical resistivity is reasonably high (Rado and Folen 1961, 1962; Freeman and Schmid 1975; Siratori *et al* 1992).

There are basically two kinds of materials which exhibit magnetoelectric output, namely single phase materials and composite materials. The single phase materials have an ordered lattice having two transitions corresponding to the ferroelectric to paraelectric, the other ferro/ferri/antiferro to paramagnetic state. While in the two-phase composites, one phase is piezomagnetic and the other piezoelectric. In the single phase material, ME output arises due to the interaction between the magnetic and ferroelectric sublattices (Suryanarayana 1994) while in the composite, ME output, a product property, is essentially due to the interaction between two participating phases (Van Suchtelen 1992; Suryanarayana *et al* 1992). Further, it is to be noted that in neither of the individual phases ME signal is observed. The synthesis of the materials is itself a challenging task since the impurity phases and interphases that may be formed in the composite and other defects, if any, may also affect the signal. In the case of single phase materials, most of the known ME compounds have complicated crystal structures and show output at low temperatures. However, the best known ME materials like $Cr_2O_3$ and boracites were studied in the single crystal form (Astrov 1960; Folen *et al* 1961; Ascher *et al* 1966). In most other cases, the data on polycrystalline materials can still yield useful information to understand the structure–property correlations.

An important aspect of magnetoelectric phenomenon is the necessity to pole the samples both electrically and magnetically. A proper poling methodology would ensure dipole reorientations so that the sub-lattices (in the case of single phase material) or different constituent phases (in the case of composites) would effectively participate to yield reasonable polarization, to be detected as a voltage or charge output.

Both linear and higher order ME coefficients are possible, which have their origin in the expansion of density of stored free enthalpy $g(E, H, T)$ written in terms of a power series. The order of ME coefficient also depends on the symmetry to which the crystal belongs (Rivera 1994). The magnitude of ME output is very small but still well measurable by any of the following methods.

## 2. Measurement techniques

There are three methods of measuring ME output. (i) In the static method, ME output (charge or voltage) is measured as a function of increasing magnetic field using an electrometer having high input impedance. While poling, there is a possibility of charges to get accumulated at the grain boundaries which move towards the electrodes during the measurement. The discharge of the charges needs quite a lot of time, before actually the final output is stabilized (Hanumaiah *et al* 1994; Singh *et al* 1994; Suryanarayana 1994; James *et al* 1997). The accumulated charges in some materials may lead to erroneous conclusions as we inferred earlier in the case of $Bi_5FeTi_3O_{15}$ (Singh *et al* 1994), (ii) for more precise data, quasi-static method is employed, which involves a time varying DC magnetic field and a high impedance electrometer. The output is measured as a function of time. This technique was used by Rivera (1994) in single crystal boracites and Ye *et al* (1994) in $Cr_3B_7O_{13}Cl$. But this method cannot be employed for a polycrystalline material as the charge build up at the grain boundaries still affects the ME output and (iii) dynamic method.

---

*Author for correspondence

## 2.1 *Dynamic method*

In the dynamic method, the output ME voltage is measured with a bias AC magnetic field while keeping the quasi-static measurement in act i.e. the measurement is carried out with a time varying DC magnetic field in the presence of an AC field. The bias AC magnetic field employed will not allow the charges to move towards the electrodes since a suitable signal with an appropriate frequency is used where the polarity of the signal changes with time. In what follows, the authors describe the details of dynamic method of measuring ME output that has been set up. The basic equations necessary to evaluate ME coefficients from the voltage are given below (Rivera 1994).

When a DC magnetic field is applied, ME output voltage ($V$), in a polycrystalline material showing second-order effect can be given by the following equation,

$$V \propto (\alpha H + \beta \cdot H \cdot H),$$

where $\alpha$ and $\beta$ are the coefficients of linear and quadratic components of ME. Suppose that if an AC field $h_0$ is superimposed over the DC field $H_0$, then the effective field is

$$H = H_0 + h_0 \sin(\omega t).$$

A lock-in-amplifier tuned to the frequency $\omega$ ($\omega = 2\pi f$) would measure the output ME signal. Then we can write,

$$V \propto (\alpha + \beta H_0) h_0 = \alpha^*(H_0) h_0 .$$

When $H_0$ is zero, it is possible to find out the linear term $\alpha$ and hence the second-order term $\beta$ is evaluated in the presence of DC magnetic field. When $H_0$ is not zero, the above equation shows that $\alpha$ varies with $\beta$, giving rise to a pseudo-linear coefficient $\alpha^*(H_0)$.

## 2.2 *Experimental*

For the above measurement, a Helmholtz coil is mounted on the pole pieces of a DC electromagnet, whose magnetic field can be made time varying by interfacing it to a computer. The time varying DC magnetic field can be achieved by a programmable stepper motor attached to the potentiometer of the DC magnetic power supply. The block diagram is given in figure 1.

A stepper motor with 0·7 kg-cm torque and having

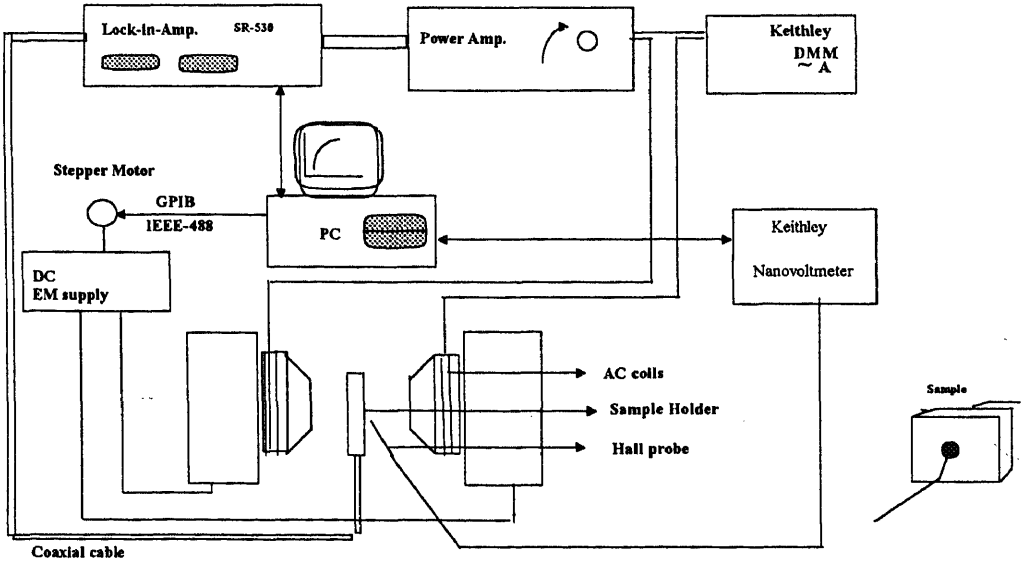

**AC Magnetoelectric effect (Block Diagram)**

**Figure 1.** Block diagram of dynamic magnetoelectric experimental setup.

1·2° angle per rotation is used for the present purpose. A closed loop control system was achieved by measuring the output of the Hall probe in the Keithley 181 Nanovoltmeter and calibrating the Hall voltage with the field. Using the GPIB, it is possible to control the input power supply of the magnet using the combination of stepper motor and potentiometer. The AC Helmholtz coils each of 130 turns were mounted on the DC pole pieces. The ratio of the magnetic induction and the current through the coils is independent of the frequency. The coils are excited with a low-amplitude high-frequency (1·006 kHz) signal, using the internal oscillator of the lock-in-amplifier (SR-530). Since the signal current was very small to drive the coils, a power amplifier was used to amplify the current. The AC magnetic field thus generated was calculated knowing the current carried by the coils using a Keithley 196 DMM. The whole setup was properly shielded to avoid stray pickups.

Keeping the DC magnetic field zero, with increasing AC field, the ME signal was recorded which gives the linear coefficient ($\alpha$). Then by properly selecting a fixed value of AC magnetic field, the DC field was swept using the stepper motor through the computer. The induced ME signal in the sample was measured with the lock-in-amplifier (SR530). With known values of $\alpha$, $h_0$, $H_0$ and $V$, the value of second-order coefficient ($\beta$) can be calculated. Since, the total measuring time to complete the experiment is only few minutes, no time is available for the charges to accumulate in the sample, as in the case of pure DC $(\mathrm{ME})_H$ measurements. The signal output in voltage represents the true value. The same experimental setup, was used to take a temperature scan of the ME signal at fixed AC and DC bias fields by inserting the sample in a dewar in between the pole pieces. The data on $(\mathrm{ME})_H$ at different temperatures would be useful to identify whether there are any magnetic anomalies in the material (Ikeda *et al* 1994).

Using the above experimental setup, AC (ME) measurements were carried out on the following materials, which have been studied earlier for their synthesis, characterization and DC$(\mathrm{ME})_H$ output in our laboratory (Singh *et al* 1994; Singh 1996; Mahesh Kumar *et al* 1998): (i) $Bi_5FeTi_3O_{15}$ and (ii) (90%)$BiFeO_3$–(10%)$BaTiO_3$.

In addition to the data at room temperature (RT), measurements were also made at 77 K. The temperature was measured using a Lakeshore silicon diode sensor DT-470. The samples were electroded with silver paint on both the sides and properly annealed. Two copper leads were attached on both the sides of the sample using epoxy resin. Prior to the measurement, the samples were poled electrically (15 kV/cm at 110°C) and magnetically (3 kOe at RT).

The AC field ($h_0$) employed was 18 Oe at 1·006 kHz. A floating crystal was used to measure ME output and the differential inputs of the lock-in-amplifier were used to measure the output signal with coaxial cables. Along with the signal, the phase shift was also recorded. To minimize the noise due to cabling, a pre-amplifier SR-550 was included in the circuit.

As pointed out by Rivera (1994b), this experimental setup needs no calibration, contrary to $(\mathrm{ME})_E$ method. Nevertheless, we have reexamined the data on $Bi_5FeTi_3O_{15}$, which was investigated by Singh (1996).

## 3. Results

### 3.1 $Bi_5FeTi_3O_{15}$

Figure 2 shows ME output of $Bi_5FeTi_3O_{15}$. At room temperature, value of the output voltage decreased with increasing DC magnetic field (with AC field superimposed) up to 6 kOe. The shape of the curve is identical with that obtained by Singh (1996). It appears that the saturation fields are still higher. At 77 K, while the nature of the output was similar to that at RT, with

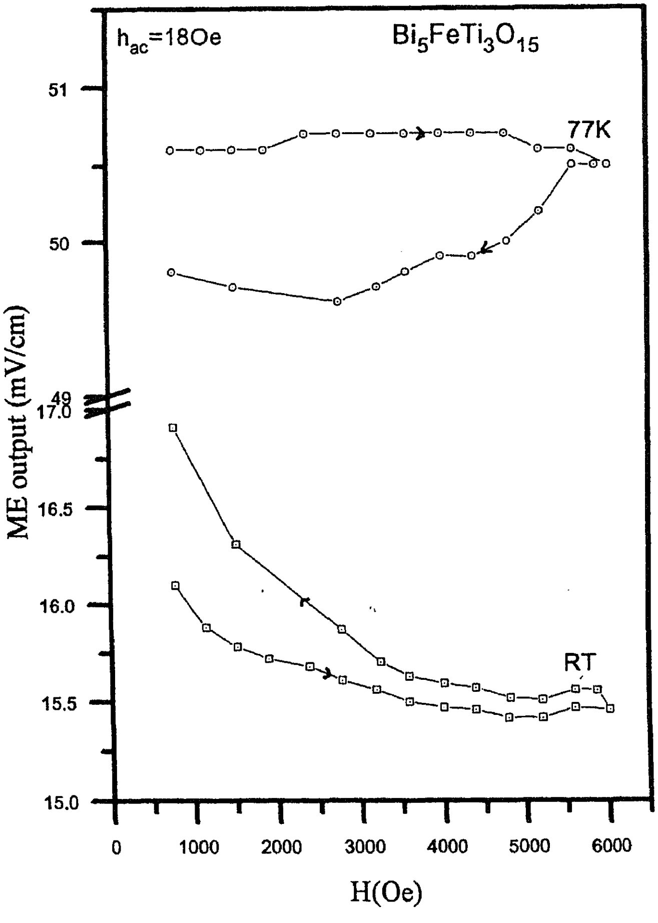

**Figure 2.** Variation of magnetoelectric output with DC bias magnetic field for $Bi_5FeTi_3O_{15}$ at room temperature and 77 K.

increasing field, the difference between the low field and high field value is small. On reversal of the applied magnetic field, both the curves do not retrace the same path. The remanance at RT is 16·9 mV/cm, while at 77 K the value is 49·8 mV/cm. The calculated values of $\alpha$ at RT and 77 K are 0·1 mV/cm-Oe and 2·8 mV/cm-Oe, respectively. The value of linear coefficient increases with decreasing temperature. At RT the second order coefficient ($\beta$) is $1{\cdot}37 \times 10^{-8}$ mV/cm-Oe$^2$ and that at 77 K is $5{\cdot}62 \times 10^{-9}$ mV/cm-Oe$^2$.

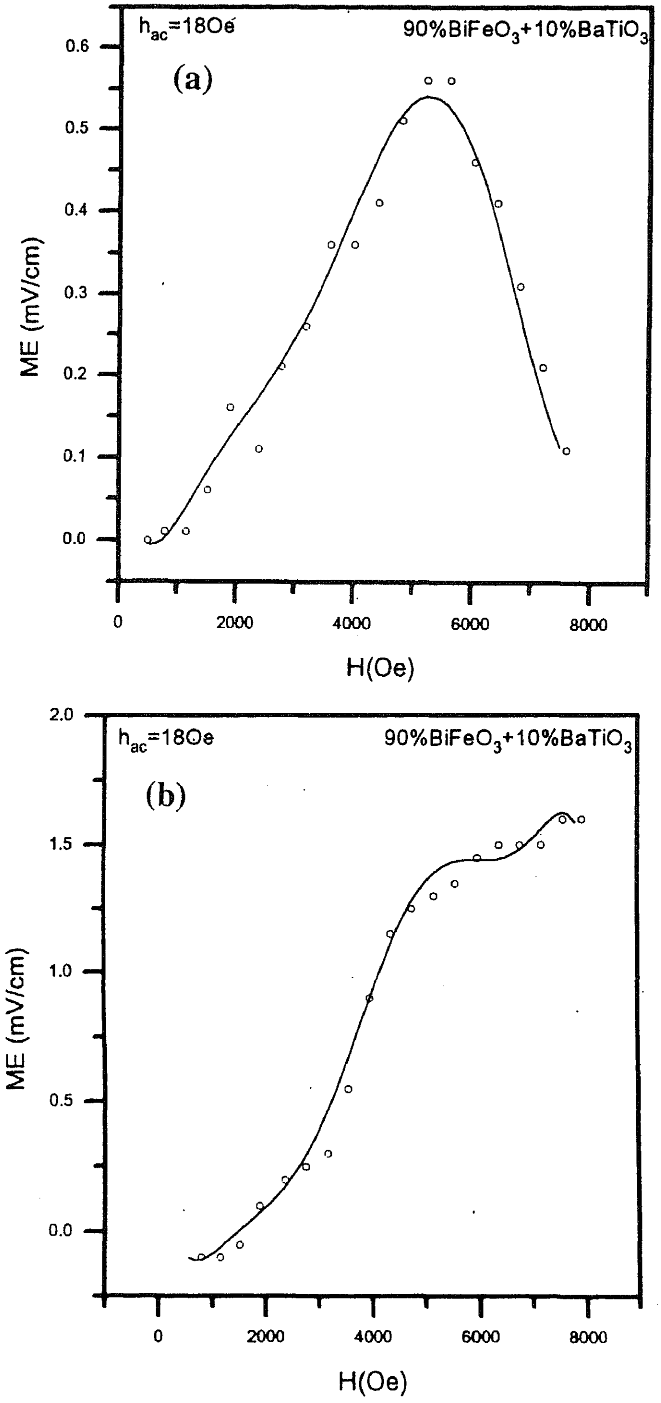

**Figure 3.** **a.** Variation of magnetoelectric output with DC bias magnetic field for (90%)BiFeO$_3$–(10%)BaTiO$_3$ at room tempe-

### 3.2 *(90%)BiFeO$_3$–(10%)BaTiO$_3$*

Ismailzade *et al* (1981) have reported that BiFeO$_3$–BaTiO$_3$ forms a series of solid solutions with different structural modifications. It is rhombohedral between 100–67% of BiFeO$_3$, 67% to 7% cubic and from 7% tetragonal. They also reported magnetoelectric measurements at room temperature for the composition 95%BiFeO$_3$–5%BaTiO$_3$. From the polarization vs magnetic field plot, they observed that the polarization increased with increasing field and at about 7 kOe, the output suddenly decreased. Recently, we have synthesized this system and reported its dielectric and electrical properties (Mahesh Kumar *et al* 1998).

Figure 3a shows ME output of (90%)BiFeO$_3$–(10%) BaTiO$_3$ at RT. The value of the output increases with increasing DC field, reaches a maximum at ~ 5·5 kOe and later decreases. This field is lower than what Ismailzade *et al* (1981) have observed for (95%)BiFeO$_3$–(5%)BaTiO$_3$. Thus the mole% of BaTiO$_3$ in BiFeO$_3$ has an effect on ME output and also on the magnetic field required to observe the peak in ME vs field measurement.

Figure 3b shows ME output of the sample at 77 K. ME output in this case peaks at ~ 6 kOe. However, this peak is less pronounced than that observed at room

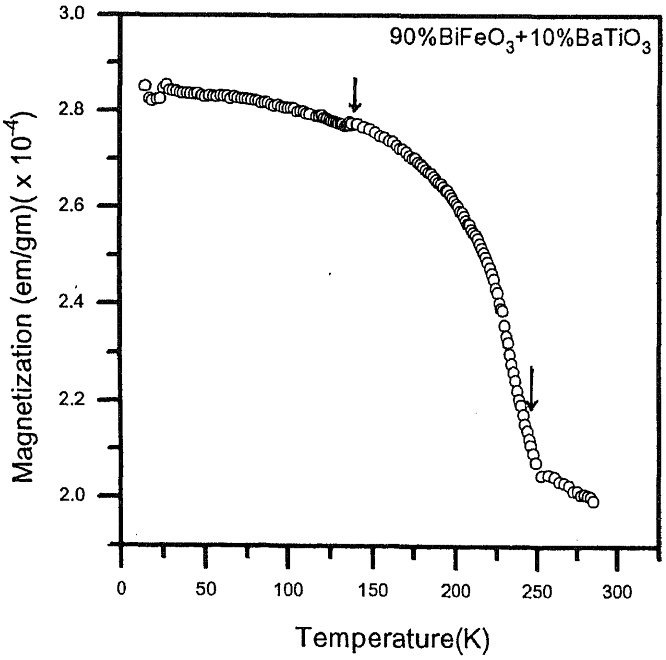

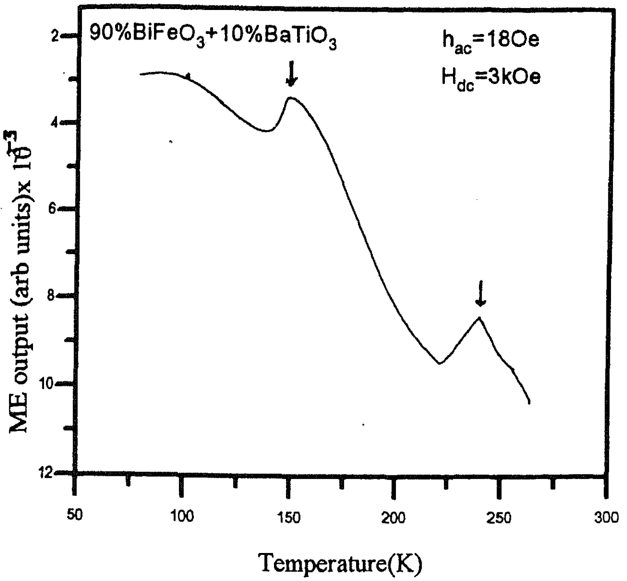

**Figure 5.** Variation of magnetoelectric output with temperature for (90%)$BiFeO_3$–(10%)$BaTiO_3$.

temperature. The maximum value of ME output obtained is ~ 1·6 mV/cm. The value of ME output has increased with decreasing temperature.

Figure 4 shows the magnetization vs temperature of the compound (90%)$BiFeO_3$–(10%)$BaTiO_3$. It is seen that the sample shows ferromagnetic nature, but as the temperature approaches RT, the magnetization does not approach zero. It indicates that there may be yet another magnetic anomaly after the cross over from ferromagnetic state with a $T_c$ around 255 K. Whereas there is a slope change around 140 K, which may be attributed to the magnetic disorder in the system which appears at low temperatures.

Figure 5 shows the magnetoelectric output vs temperature for the sample measured at $h_{ac} = 18$ Oe and $H_{dc} =$ 3 kOe in the temperature range 77–300 K. Anomalies were observed at ~ 149 K and at 238 K corroborating with the slope changes in the magnetization data (figure 4), which indicates that the present experimental setup is useful not only to measure the ME output but also to corroborate small variations/fluctuations in the magnetization data.

## 4. Conclusions

A versatile dynamic technique to measure ME output has been setup. The technique can be used to perform a few additional experiments to yield the following data: (i) magnetoelectric output at room temperature and at different temperatures, (ii) from the data one can evaluate the linear and quadratic ME coefficients ($\alpha$ and $\beta$), remanance and saturation fields, (iii) if the DC field is swept, both to positive and negative polarities, a butterfly loop can be traced between the applied field and output voltage, (iv) the phase angle of the output signal can be detected, which can be exploited for the possible device applications, (v) temperature scan of ME output can indicate possible magnetic transitions, and (vi) frequency scan at a particular temperature can also be made. A flat frequency response would be ideal for the material to be used as a transducer (Bracke and Van Vliet 1981).

## Acknowledgements

The authors thank DRDO, Govt. of India for the financial assistance. MMK thanks CSIR for the award of a Senior Research Fellowship, Dr R S Singh (now at IISc, Bangalore) for many useful discussions in setting up the experiment and also thanks Prof. S N Kaul, University of Hyderabad, for providing facilities for magnetization measurements.

## References

Ascher E, Rieder H, Schmid H and Stossel H 1966 *J. Appl. Phys.* **37** 1404

Astrov D N 1960 *J. Exp. Theor. Phys. (USSR)* **38** 984

Bracke L P M and Van Vliet R G 1981 *Int. J. Electron.* **51** 255

Folen V T, Rado C T and Stalder E W 1961 *Phys. Rev. Lett.* **6** 607

Freeman A J and Schmid H (eds) 1975 *Magnetoelectric interaction phenomena in crystals* (London: Gordon and Breach)

Hanumaiah A, Bhimasankaram T, Suryanarayana S V and Kumar G S 1994 *Bull. Mater. Sci.* **17** 405

Ikeda N, Saito K, Kohn K, Kita H, Akimiku J and Siratori K 1994 *Ferroelectrics* **161** 111

Ismailzade I H, Ismailov R M, Alekberov A I and Salaev F M 1981 *Phys. Status Solidi (a)* **68** K81

James A R, Kumar G S, Mahendra Kumar, Suryanarayana S V and Bhimasankaram T 1997 *Mod. Phys. Lett.* **B11** 633

Mahesh Kumar M, Srinivas A, Suryanarayana S V and Bhimasankaram T 1998 *Phys. Status Solidi (a)* **165** 317

Rado G T and Folen V J 1961 *Phys. Rev. Lett.* **7** 310

Rado G T and Folen V J 1962 *J. Appl. Phys.* **33** 1126

Rivera J P 1994 *Ferroelectrics* **161** 147, 165

Singh R S 1996 *Structure–property correlations in some magnetically ordered Aurivillius phases*, Ph D thesis, Osmania University, Hyderabad

Singh R S, Bhimasankaram T, Kumar G S and Suryanarayana S V 1994 *Solid State Commun.* **91** 567

Siratori K, Kohn K and Kita E 1992 *Acta Phys. Polonica* **A81** 4

Suryanarayana S V 1994 *Bull. Mater. Sci.* **17** 1259

Suryanarayana S V, Sarah P, Singh R S, Bhimasankaram T and Mulay V N 1992 *Proc. 5th Asia-Pacific physics conference, Kaula Lampur* (Singapore: World Scientific) **2** 738

Van Suchtelen J 1992 *Phillips. Res. Rep.* **27** 28

Ye Z-G, Rivera J P, Schmid H, Heida M and Kohn K 1994 *Ferroelectrics* **161** 99

# Density of micro-quantity liquids by the method of rise of drops in immiscible liquids

**G J SRINIVASAN***, **G THIRUNAVUKKARASU**[†] **and P SATYANARAYANA**[†]
Department of Electronics and Instrumentation, St. Peter's Engineering College, Avadi, Chennai 600 054, India
[†] Physics Division, Forensic Sciences Department, Chennai 600 004, India

MS received 12 January 1998; revised 18 April 1998

**Abstract.** **The conventional methods such as specific gravity bottle method, pyknometer method, and the Westphal-balance method or the capillary tube method where accurate weighing is a problem cannot be employed when liquids are available in micro-quantities. The method described may be employed to determine the density of micro-quantity liquids (even up to 0·5 $\mu$l) and it is found to be simple and rapid. The method also allows the analyst to retrieve the sample for further analysis.**

**Keywords.** **Density; micro-quantity liquids; rise of liquid drops; immiscible liquid column.**

## 1. Introduction

Studies on the rise of liquid drops through an immiscible liquid column have been carried out by several authors (Klee and Treybal 1956; Saffman 1956; Bhattacharya and Venkateswarlu 1957; Houghton *et al* 1957; Harmathy 1960; Goldsmith and Mason 1962; Griffith 1962; Davis and Acrivos 1966; Zieminski and Raymond 1968; Grace *et al* 1976; Clift *et al* 1978). Srinivasan *et al* (1996) have previously dealt with the problem of rise of liquid drops with six variables, $F, D, u, \sigma, \eta$ and $\rho$ alone ($F$, drag force; $D$, diameter of the liquid drop, $u$, terminal velocity acquired by the liquid drop; $\eta$, viscosity of the liquid in the column, $\rho$, density of the liquid drop; $\sigma$, density of the liquid in the column), to arrive at an expression for the drag force, $F$ acting on the drop in rise through the method of dimensions. It has been suggested that the simple expression for the constant quantity, $S$ occurring in the process of simplification of the drag force expression, $F$ may be used to determine the density, $\rho$ of the liquid drop.

The expression for the density, $\rho$ obtained (Srinivasan *et al* 1996) is

$$\rho = \{(2\sigma + \lambda) - [\lambda(\lambda + 4\sigma)]^{1/2}\}/2, \quad (1)$$

where

$$\lambda = S^2 \eta/(r/u)^3, \quad (2)$$

$$S = [(r/u)^{3/2}(\sigma - \rho)]/[\eta^{1/2}\rho^{1/2}], \quad (3)$$

$r$ being radius of the drop.

The physical property, density assumes a position of great importance in the identification of pure liquids. When liquids are available in bulk quantities, conventional methods like specific gravity bottle method, pyknometer method, Westphal-balance method etc may be employed to determine this physical constant. When liquids are available in small quantities and when neither the conventional methods nor the capillary tube method (where weighing is a problem) is adoptable, a new method has to be developed to determine the density of the micro-quantity liquids.

In the present paper, therefore, the method and the expression for $\rho$ suggested earlier (Srinivasan *et al* 1996) have been employed to determine the density, $\rho$ of liquid drops and the results obtained have been presented.

## 2. Experimental

### 2.1 *Equipment and liquids used*

A long graduated glass cylinder (of internal diam. 0·05 m and height 1·5 m) with a small side tube attached to it at the bottom and sealed with a rubber septum (figure 1); stop watch (Racer), accurate to 0·05 sec; Hamilton precision syringe, accurate to 0·01 μl; Ethylene glycol and soap oil (Ranbaxy purified grade); Hexane, Heptane, MIBK, Xylene, Cyclohexane, Benzene, Toluene, Iso-amyl acetate (Fisher purified grade); Turpentine (Chemlab purified grade); Water, Petrol, Kerosene, Naphtha and Diesel (distilled); Palm oil, Groundnut oil and Gingely oil (KKR refined grade); Coconut oil (VVD refined grade); Castor oil (Richardson refined grade); Sandalwood oil (Vibhav purified grade), were used (table 2).

---

*Author for correspondence

The liquids viz. ethylene glycol, water, chlorobenzene and bromobenzene, which were immiscible with the corresponding drop liquids (table 2) were selected as column liquids and used for filling the cylindrical column. Liquid drops of known volume were gently injected at the bottom of the liquid column using a graduated Hamilton Precision micro-syringe. When the drop rised freely and vertically without oscillation, the terminal velocity, $u$ was determined by observing the time, $t$ required by the liquid drop of radius, $r$ to cover the

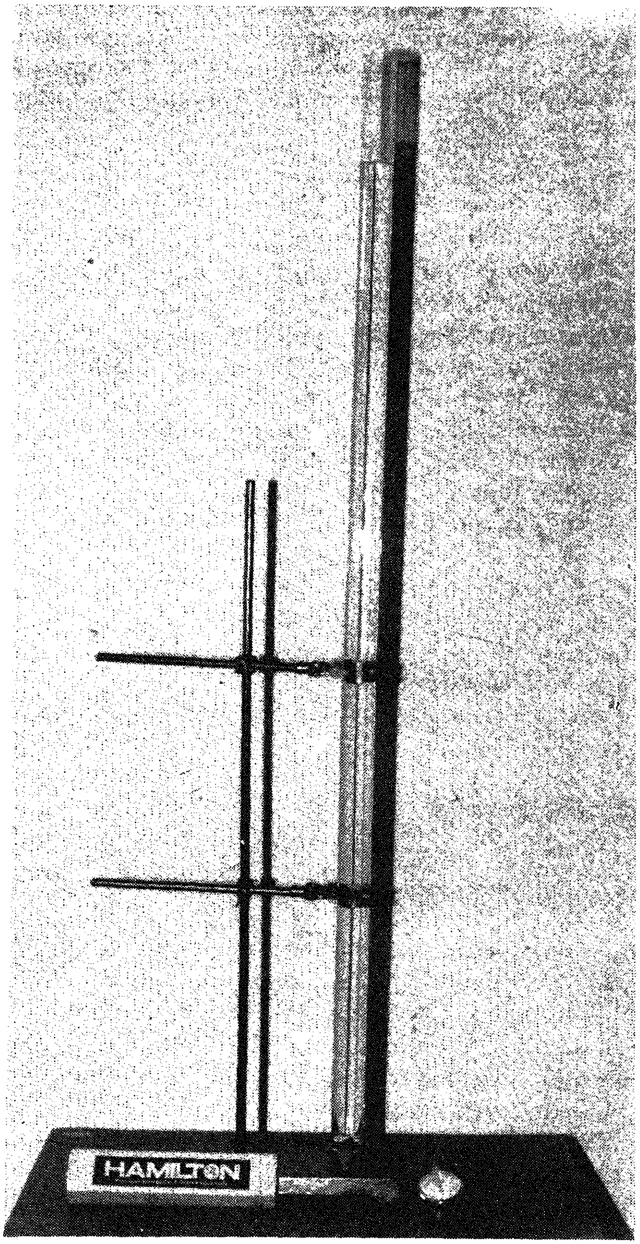

**Figure 1.** The set up used for conducting rising drop experiments.

of diameter, $D$ then the drop radius was obtained from $r = (3V/4\pi)^{1/3}$, where $r = D/2$. All the experiments were conducted at room temperature (25°C).

## 3. Results and discussion

The data presented in table 1 for ten liquid drop–liquid pair systems having three data points each shows that $r/u$ is approximately constant. The other seventeen liquid drop–liquid pair systems (table 2) for which the experimental results have been obtained satisfy the same. The density of the column liquids and the drop liquids, viscosity of the column liquids, interfacial tension between the liquid drop and liquid column given in table 2 were determined by the specific gravity bottle method, Ostwald Viscometer and the method of drops, respectively. The values of $(r/u)^{3/2}/\eta^{1/2}$, $\rho^{1/2}/(\sigma - \rho)$, and $S$ are given in table 3. Table 4 furnishes the observed density of the liquids (refer table 2) and the density of liquids determined from (1) and the estimated error in percentage. It may be seen from table 1 that for liquid drops of different radii of a given liquid pair system, $r/u$ is a constant. The value of $S$ calculated from (3) has been found to be approximately constant for all the liquid drop–liquid pair systems (table 3) and its mean value is $0{\cdot}313366\ \mathrm{m}^{-1}\,\mathrm{s}^2$ (table 3). This mean value of $S$ is also found to be approximately equal and agree to the experimental mean value of $S$ ($0{\cdot}3176\,\mathrm{m}^{-1}\,\mathrm{s}^2$) predicted previously for the thirteen liquid drop–liquid pair systems (Srinivasan *et al* 1996). The density values of the liquid drop estimated from (1) (column 4, table 4) using the experimental mean value of $S$ ($0{\cdot}313366\,\mathrm{m}^{-1}\,\mathrm{s}^2$; table 3), $r/u$ (table 2) and $\eta$ (table 2) show that they are comparable with the observed density value of the liquids determined by the specific gravity bottle method (column 3, table 4). The estimated error in percentage (column 5, table 4) is found to be less than 0·5% between the observed and the calculated density values (table 4).

Since by knowing the radius, $r$ of the liquid drop and the terminal velocity, $u$ attained by it in the liquid column, one may determine the density of the liquid drop from (1) with the experimentally predicted mean value of $S$ ($0{\cdot}313366\,\mathrm{m}^{-1}\,\mathrm{s}^2$, table 3) and the viscosity of the liquid in the column (table 2), the only unknown quantity to be determined being $r/u$. This may be accomplished in one or two min.

The minimum amount of liquid sample required for this method is less than 1 $\mu$l, and therefore this method may be adopted to determine the density of a liquid sample available in small or micro-quantities for which the density cannot be determined by any other conventional method. It also provides a solution to the analyst who prefers, as far as possible to preserve the original

**Table 1.** Experimental data for liquid drop–liquid pair systems.

| Liquid drop–liquid pair systems | $V$ (μl) | $r$ ($\times 10^{-4}$ m) | $d$ ($\times 10^{-2}$ m) | $t$ (sec) | $u$ ($\times 10^{-2}$) (m s$^{-1}$) | $r/u$ (s) | Reynolds number ($R_e$) | Eotvos number $E_t$ ($\times 10^{-2}$) | Morton number ($M_0$) |
|---|---|---|---|---|---|---|---|---|---|
| Hexane in EG* | 0·5 | 4·9237 | 0·4 | 14·0 | 2·8571 | 0·01723 | 2·05 | 19·50 | $1{\cdot}8 \times 10^{-5}$ |
| | 1·0 | 6·2035 | 0·4 | 11·0 | 3·6363 | 0·01705 | 3·28 | 30·96 | |
| | 2·0 | 7·8159 | 0·4 | 8·8 | 4·5454 | 0·01719 | 5·17 | 49·15 | |
| Petrol in EG* | 0·5 | 4·9237 | 0·4 | 15·4 | 2·5974 | 0·01895 | 1·86 | 22·38 | $3{\cdot}6 \times 10^{-5}$ |
| | 1·0 | 6·2035 | 0·4 | 12·2 | 3·2786 | 0·01892 | 2·96 | 35·53 | |
| | 2·0 | 7·8159 | 0·4 | 9·7 | 4·1237 | 0·01895 | 4·69 | 56·41 | |
| Heptane in EG* | 0·5 | 4·9237 | 0·4 | 15·6 | 2·5641 | 0·01920 | 1·84 | 17·73 | $1{\cdot}8 \times 10^{-5}$ |
| | 1·0 | 6·2035 | 0·4 | 12·4 | 3·2258 | 0·01923 | 2·91 | 28·15 | |
| | 2·0 | 7·8159 | 0·4 | 9·9 | 4·0404 | 0·01934 | 4·60 | 44·69 | |
| Naphtha in EG* | 0·5 | 4·9237 | 0·4 | 16·0 | 2·5000 | 0·01969 | 1·79 | 23·24 | $4{\cdot}4 \times 10^{-5}$ |
| | 1·0 | 6·2035 | 0·4 | 12·7 | 3·1496 | 0·01969 | 2·84 | 36·89 | |
| | 2·0 | 7·8159 | 0·4 | 10·1 | 3·9603 | 0·01973 | 4·51 | 58·56 | |
| MIBK in EG* | 0·5 | 4·9237 | 0·4 | 18·5 | 2·1621 | 0·02277 | 1·55 | 97·55 | $4{\cdot}6 \times 10^{-3}$ |
| | 1·0 | 6·2035 | 0·4 | 14·7 | 2·7210 | 0·02279 | 2·46 | 154·86 | |
| | 2·0 | 7·8159 | 0·4 | 11·6 | 3·4482 | 0·02266 | 3·92 | 245·82 | |
| Kerosene in EG* | 0·5 | 4·9237 | 0·4 | 18·7 | 2·1390 | 0·02301 | 1·53 | 24·83 | $7{\cdot}8 \times 10^{-5}$ |
| | 1·0 | 6·2035 | 0·4 | 14·8 | 2·7027 | 0·02295 | 2·44 | 39·41 | |
| | 2·0 | 7·8159 | 0·4 | 11·7 | 3·4188 | 0·02286 | 3·89 | 62·57 | |
| Diesel in EG* | 0·5 | 4·9237 | 0·4 | 20·4 | 1·9607 | 0·02511 | 1·40 | 16·86 | $3{\cdot}0 \times 10^{-5}$ |
| | 1·0 | 6·2035 | 0·4 | 16·2 | 2·4691 | 0·02512 | 2·23 | 26·76 | |
| | 2·0 | 7·8159 | 0·4 | 12·8 | 3·1250 | 0·02501 | 3·56 | 42·48 | |
| Soap oil in EG* | 0·5 | 4·9237 | 0·4 | 22·1 | 1·8099 | 0·02720 | 1·29 | 30·25 | $1{\cdot}8 \times 10^{-5}$ |
| | 1·0 | 6·2035 | 0·4 | 17·6 | 2·2727 | 0·02729 | 2·05 | 21·03 | |
| | 2·0 | 7·8159 | 0·4 | 13·9 | 2·8776 | 0·02716 | 3·27 | 33·39 | |
| Xylene in EG* | 0·5 | 4·9237 | 0·4 | 22·25 | 1·7976 | 0·02739 | 1·29 | 17·07 | $3{\cdot}9 \times 10^{-5}$ |
| | 1·0 | 6·2035 | 0·4 | 17·50 | 2·2857 | 0·02714 | 2·07 | 27·10 | |
| | 2·0 | 7·8159 | 0·4 | 13·95 | 2·8674 | 0·02726 | 3·27 | 43·01 | |
| Benzene in EG* | 0·5 | 4·9237 | 0·4 | 23·1 | 1·7316 | 0·02843 | 1·24 | 24·82 | $1{\cdot}3 \times 10^{-4}$ |
| | 1·0 | 6·2035 | 0·4 | 18·3 | 2·1857 | 0·02838 | 1·97 | 39·41 | |
| | 2·0 | 7·8159 | 0·4 | 14·5 | 2·7586 | 0·02833 | 3·14 | 62·56 | |

*Ethylene glycol.

$R_e = \sigma u D/\eta$; $E_t = g\,(\sigma - \rho)\,D^2/\gamma$; $M_0 = g\eta^4\,(\sigma - \rho)/\sigma^2\gamma^3$.

$\rho, \sigma, \eta$ and $\gamma$ from table 2; $g = 9{\cdot}8$ m s$^{-2}$; $D = 2r$.

**Table 2.** Liquid drop–column liquid pair systems and their physical constants.

| Sl. no. | Liquid drop | Liquid column | $\rho$ (kg$^{-3}$) | $\sigma$ (kg$^{-3}$) | $(\sigma-\rho)$ (kg$^{-3}$) | $\eta$ (Nsm$^{-2}$) | $\gamma$ (nm$^{-1}$) ($\times 10^{-3}$) | $r/u$ (s) |
|---|---|---|---|---|---|---|---|---|
| 1. | Hexane | EG* | 665·12 | 1108·00 | 442·88 | 0·01520 | 21·6 | 0·017192 |
| 2. | Petrol | EG* | 715·38 | 1108·00 | 392·62 | 0·01520 | 16·7 | 0·018964 |
| 3. | Heptane | EG* | 720·24 | 1108·00 | 387·76 | 0·01520 | 20·8 | 0·019244 |
| 4. | Naphtha | EG* | 733·29 | 1108.00 | 374·71 | 0·01520 | 15·3 | 0·019708 |
| 5. | MIBK | EG* | 792·85 | 1108·00 | 315·15 | 0·01520 | 3·1 | 0·022752 |
| 6. | Kerosene | EG* | 797·22 | 1108·00 | 310·78 | 0·01520 | 11·9 | 0·022998 |
| 7. | Diesel | EG* | 830·65 | 1108·00 | 277·35 | 0·01520 | 15·6 | 0·025111 |
| 8. | Soap oil | EG* | 857·01 | 1108·00 | 250·99 | 0·01520 | 18·0 | 0·027218 |
| 9. | Xylene | EG* | 857·50 | 1108·00 | 250·50 | 0·01520 | 13·9 | 0·027318 |
| 10. | Benzene | EG* | 870·60 | 1108·00 | 237·40 | 0·01520 | 9·1 | 0·028376 |
| 11. | Palm oil | EG* | 876·66 | 1108·00 | 231·34 | 0·01520 | 9·6 | 0·028816 |
| 12. | Groundnut oil | EG* | 910·91 | 1108·00 | 197·09 | 0·01520 | 12·0 | 0·032461 |
| 13. | Gingely oil | EG* | 915·85 | 1108·00 | 192·15 | 0·01520 | 12·3 | 0·033150 |
| 14. | Coconut oil | EG* | 917·27 | 1108·00 | 190·73 | 0·01520 | 13·3 | 0·033273 |
| 15. | Castor oil | EG* | 925·72 | 1108·00 | 182·28 | 0·01520 | 7.2 | 0·034431 |
| 16. | Sandalwood oil | EG* | 960·20 | 1108·00 | 147·80 | 0·01520 | 14·1 | 0·040103 |
| 17. | Heptane | Water | 720·37 | 1000·00 | 279·63 | 0·00100 | 38·7 | 0·009765 |
| 18. | Cyclohexane | Water | 775·04 | 1000·00 | 224·96 | 0·00100 | 20·4 | 0·011578 |
| 19. | Kerosene | Water | 797·34 | 1000·00 | 202·66 | 0·00100 | 43.8 | 0·012480 |
| 20. | Soap oil | Water | 857·15 | 1000·00 | 142·85 | 0·00100 | 34·2 | 0·015956 |
| 21. | Xylene | Water | 857·95 | 1000·00 | 142·05 | 0·00100 | 29·0 | 0·016010 |
| 22. | Turpentine | Water | 860·03 | 1000·00 | 139·97 | 0·00100 | 41·5 | 0·016448 |
| 23. | Toluene | Water | 860·89 | 1000·00 | 139·11 | 0·00100 | 39·7 | 0·016543 |
| 24. | Benzene | Water | 870·78 | 1000·00 | 129·22 | 0·00100 | 35·0 | 0·017382 |
| 25. | Iso-amylacetate | Water | 882·15 | 1000·00 | 117·85 | 0·00100 | 29·2 | 0·018537 |
| 26. | Water | Chlorobenzene | 1000·00 | 1097·99 | 97·99 | 0·00071 | 46·1 | 0·019610 |
| 27. | Ethylene glycol | Bromobenzene | 1108·00 | 1492·21 | 384·21 | 0·00085 | 11·2 | 0·008580 |

$\rho$, Density of the liquid drop; $\sigma$, density of the column liquid; $\eta$, viscosity of the column liquid; $\gamma$, interfacial tension between the liquid drop and the liquid in the column; $r$, radius of the liquid drop; $u$, terminal velocity of the drop.
$(r/u)$: Mean experimental values. *Ethylene glycol.

**Table 3.** The values of $(r/u)^{3/2}/\eta^{1/2}$ and $\rho^{1/2}/(\sigma-\rho)$ and $S$.

| Sl. no. | Liquid drop | Liquid column | $(r/u)^{3/2}/\eta^{1/2}$ | $\rho^{1/2}/(\sigma-\rho)$ | $S$ |
|---|---|---|---|---|---|
| 1. | Hexane | EG* | 0·018284 | 0·058232 | 0·313985 |
| 2. | Petrol | EG* | 0·021182 | 0·068123 | 0·310938 |
| 3. | Heptane | EG* | 0·021653 | 0·069211 | 0·312855 |
| 4. | Naphtha | EG* | 0·022441 | 0·072267 | 0·310529 |
| 5. | MIBK | EG* | 0·027836 | 0·089346 | 0·311553 |
| 6. | Kerosene | EG* | 0·028289 | 0·090852 | 0·311375 |
| 7. | Diesel | EG* | 0·032276 | 0·103915 | 0·310600 |
| 8. | Soap oil | EG* | 0·036422 | 0·116637 | 0·312268 |
| 9. | Xylene | EG* | 0·036623 | 0·116898 | 0·313290 |
| 10. | Benzene | EG* | 0·038771 | 0·124287 | 0·311947 |
| 11. | Palm oil | EG* | 0·039676 | 0·127986 | 0·310003 |
| 12. | Groundnut oil | EG* | 0·047437 | 0·153134 | 0·309774 |
| 13. | Gingely oil | EG* | 0·048956 | 0·157492 | 0·310848 |
| 14. | Coconut oil | EG* | 0·049228 | 0·158792 | 0·310016 |
| 15. | Castor oil | EG* | 0·051821 | 0·166917 | 0·310460 |
| 16. | Sandalwood oil | EG* | 0·065139 | 0·209655 | 0·310696 |
| 17. | Heptane | Water | 0·030515 | 0·095982 | 0·317924 |
| 18. | Cyclohexane | Water | 0·039396 | 0·123753 | 0·318344 |
| 19. | Kerosene | Water | 0·044088 | 0·139332 | 0·316424 |
| 20. | Soap oil | Water | 0·063736 | 0·204950 | 0·310983 |
| 21. | Xylene | Water | 0·064060 | 0·206200 | 0·310669 |
| 22. | Turpentine | Water | 0·066707 | 0·209518 | 0·318383 |
| 23. | Toluene | Water | 0·067285 | 0·210918 | 0·319010 |
| 24. | Benzene | Water | 0·072469 | 0·228362 | 0·317343 |
| 25. | Iso-amylacetate | Water | 0·079810 | 0·252024 | 0·316676 |
| 26. | Water | Chlorobenzene | 0·103059 | 0·322714 | 0·319351 |
| 27. | Ethylene glycol | Bromobenzene | 0·027260 | 0·086636 | 0·314650 |
| | | | | Mean | 0·313366 |

*Ethylene glycol; $(r/u)$, $\eta, \rho$ and $(\sigma-\rho)$ from table 2.
$S = [(r/u)^{3/2}/\eta^{1/2}]/[\rho^{1/2}/(\sigma-\rho)]$

**Table 4.** Comparison of density values and estimated error in percentage.

| Sl. no. | Liquid drop | Density $\rho$ (kg$^{-3}$) Observed* | Density $\rho$ (kg$^{-3}$) Estimated from (1) | Estimated error (%) |
|---|---|---|---|---|
| 1. | Hexane | 665·12 | 665·77 | – 0·098 |
| 2. | Petrol | 715·38 | 712·98 | 0·335 |
| 3. | Heptane | 720·24 | 719·74 | 0·069 |
| 4. | Naphtha | 733·29 | 730·61 | 0·365 |
| 5. | MIBK | 792·85 | 791·32 | 0·193 |
| 6. | Kerosene | 797·22 | 795·56 | 0·208 |
| 7. | Diesel | 830·65 | 828·53 | 0·255 |
| 8. | Soap oil | 857·01 | 856·24 | 0·090 |
| 9. | Xylene | 857·50 | 857·44 | 0·007 |
| 10. | Benzene | 870·60 | 869·65 | 0·109 |
| 11. | Palm oil | 876·66 | 874·45 | 0·254 |
| 12. | Groundnut oil | 910·91 | 908·85 | 0·226 |
| 13. | Gingely oil | 915·85 | 914·44 | 0·154 |
| 14. | Coconut oil | 917·27 | 915·41 | 0·203 |
| 15. | Castor oil | 925·72 | 924·17 | 0·167 |
| 16. | Sandalwood oil | 960·20 | 959·02 | 0·123 |
| 17. | Heptane | 720·37 | 723·73 | – 0·466 |
| 18. | Cyclohexane | 775·04 | 778·12 | – 0·397 |
| 19. | Kerosene | 797·34 | 799·08 | – 0·218 |
| 20. | Soap oil | 857·15 | 856·14 | 0·118 |
| 21. | Xylene | 857·95 | 856·14 | 0·133 |
| 22. | Turpentine | 860·03 | 862·07 | – 0·237 |
| 23. | Toluene | 860·89 | 863·17 | – 0·265 |
| 24. | Benzene | 870·78 | 872·29 | – 0·173 |
| 25. | Iso-amylacetate | 882·15 | 883·31 | – 0·131 |
| 26. | Water | 1000·00 | 1001·75 | – 0·175 |
| 27. | Ethylene glycol | 1108·00 | 1109·33 | – 0·120 |

*From table 2.

liquid samples in small quantities for identification and confirmation through other analytical means apart from density determination.

Since the measurement of weight of the liquid drop is not involved in this method, the availability of a high precision balance is not an essential requirement as in the case of other conventional methods viz. specific gravity bottle method, pyknometer method, Westphal-balance method (Serence *et al* 1970; O'Hara and Osterburg 1974; Giancoli 1984) etc for getting the accurate density value, and hence this method may be employed in any operational laboratory where high precision and expensive equipment is not available for accurate weighing.

The added advantage of this method is that the liquid drop injected at the bottom can be retrieved from the top of the liquid column using a micro-syringe or filter paper for further analysis as the drop liquid and the column liquid are immiscible.

## 4. Conclusion

This method may be employed to determine the density of liquids available in small or micro-quantities and also provides a practical alternative to other conventional methods. The authors do not suggest that this approach is an acceptable substitute for those liquids which do not have any suitable column liquid. Therefore, the column liquid should be selected in such a way that it is immiscible with as well as denser than the liquid to be tested.

## References

Bhattacharya S P and Venkateswarlu D 1957 *Trans. Indian Inst. Chem. Engrs.* **10** 25
Clift R, Grace J R and Weber M E 1978 *Bubbles, drops and particles* (New York: Academic Press)
Davis R E and Acrivos A 1966 *Chem. Eng. Sci.* **26** 681
Giancoli D C 1984 *General physics* (New Jersey: Prentice Hall Inc)
Goldsmith H L and Mason S G 1962 *J. Fluid. Mech.* **14** 42
Grace J R, Wairegi T and Nguyen T H 1976 *Trans. Inst. Chem. Eng.* **54** 167
Griffith R M 1962 *Chem. Eng. Sci.* **17** 1057
Harmathy T Z 1960 *Aiche. J.* **6** 281
Houghton G, Ritchie P D and Thomson J A 1957 *Chem. Eng. Sci.* **7** 111
Klee A J and Treybal R E 1956 *Aiche. J.* **2** 444
O'Hara C E and Osterburg I W 1974 *An introduction to criminalistics* (London: Indiana University Press)
Saffman P G 1956 *J. Fluid Mech.* **1** 249
Serence Jr M, Lemon H B and Stephenson R J 1970 *Analytical experimental physics* (London: The University of Chicago Press)
Srinivasan G J, Satyanarayana P and Thirunavukkarasu G 1996 *Curr. Sci.* **71** 989
Zieminski S A and Raymond D R 1968 *Chem. Eng. Sci.* **23** 17

# Bulletin of Materials Science

## Notes on the preparation of papers

Authors may communicate their research work as papers and rapid communications to the Bulletin of Materials Science. They may also submit topical reviews. The papers may be sent to the Editor or to one of the International Advisory Board members.

All communications should be submitted in triplicate (original + two copies).

**Authors are encouraged to send electronic files prepared using plain latex or MS Word (RTF), of final accepted version of their articles. This will help hasten the process of typesetting. Line drawings also may be submitted in electronic format in some standard graphic format—TIFF, for example, and saved in EPS format. However, a hard copy with figures must also be submitted along with floppy (3.5") of electronic files.**

Submission of a script will be held to imply that it has not been previously published and is not under consideration for publication elsewhere; and further that, if accepted, it will not be published elsewhere.

### Typescript

Papers must be typed double spaced with ample margin on all sides on one side of white bond paper of quarto size (280 × 215 mm). This also applies to the abstract, tables, figure captions and the list of references which are to be typed on separate sheets.

### Title page

1. The title of the paper must be brief but informative. Serial titles are to be avoided.
2. The names with initials of authors and the name and address of the institution where the work was done must be given.
3. An abbreviated running title of not more than 50 letters and spaces must also be given.
4. Authors are requested to provide e-mail and fax addresses while submitting the script.

### Abstract

Papers must have a brief abstract of the significant results reported in the paper.

### Keywords

Between 3 and 6 keywords must be provided for indexing and information retrieval.

### The Text

The paper must be divided into sections starting preferably with 'Introduction' and ending with 'Conclusions'. The main sections should be numbered 1,2 etc., the sub-sections 1.1, 1.2, etc., and further sub-sections (if necessary) 1.1a, 1.1b, etc.

### Tables

All tables must be numbered consecutively in arabic numerals in the order of occurrence in the text; they should be self-contained and have a descriptive title.

### Figures

All figures including photographs should be numbered consecutively in arabic numerals in the order of appearance in the text. Line drawings must be in Indian ink on good quality tracing paper or Bristol board of the same size as the text paper. Lines should be sufficiently thick (axes about 0.3 mm, curves about 0.6 mm).

### Units

Units and associated symbols must invariably follow SI practice.

### References

References should be cited in the text by author and year, not by number. If there are more than two authors, reference should be to the first author followed by et al in the text. References at the end of the paper should be listed alphabetically by author's names, followed by initials, year of publication, name of the journal (abbreviated according to the World List of Scientific Periodicals, Butterworths, London), volume number, and number of the first page. Reference to books should include: name(s) of author(s), initials, year of publication, title of the book, edition if not the first, initials and name(s) of editor(s) if any, preceded by ed(s), place of publication, publisher and chapter or pages referred to. References to thesis must include the year, the title of the thesis, the degree for which submitted and the University.

### Footnotes

Footnotes must be avoided if possible but when necessary should be numbered consecutively, and typed on a separate sheet.

### Proofs

Authors are requested to prepare the manuscript carefully before submitting it for publication to minimize corrections and alterations in the proof which increase publication costs. Page-proofs sent to author together with the reprint order form must be returned to the editorial office within two days of their receipt by SPEED POST/COURIER.

### Reprints

50 reprints of each article will be supplied free of charge.

# Bulletin of Materials Science

Volume 21 Number 4 August 1998

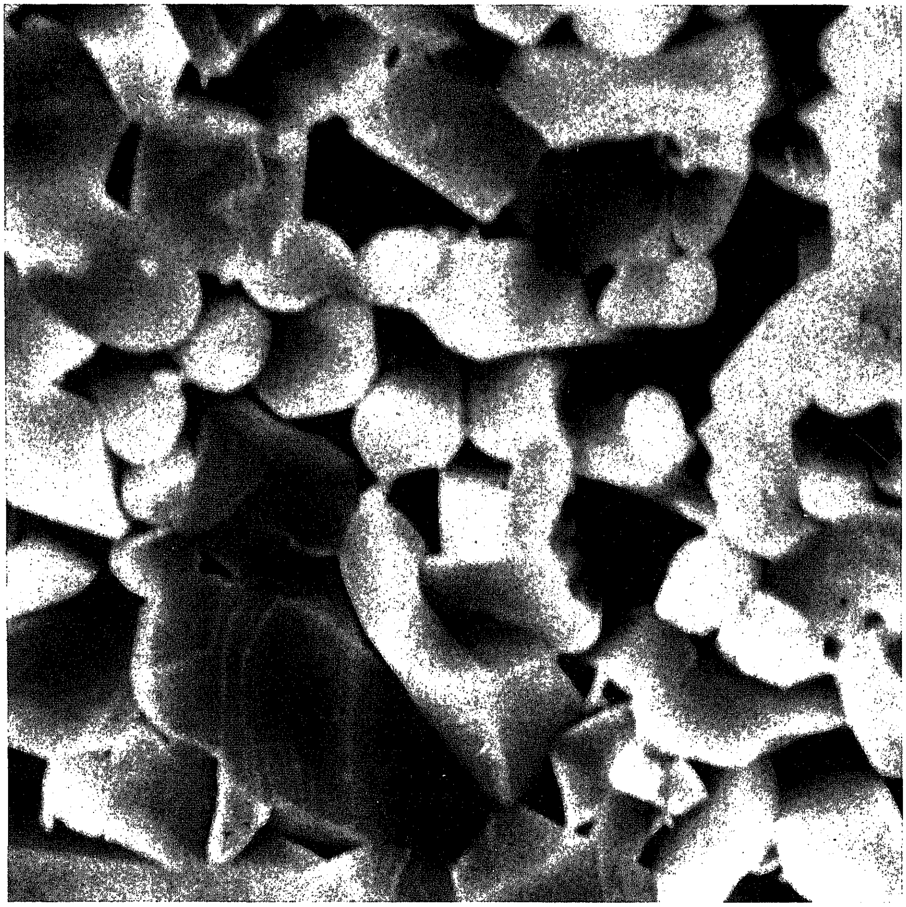

*Published by*
**INDIAN ACADEMY OF SCIENCES**
*in collaboration with*
MATERIALS RESEARCH SOCIETY OF INDIA and
INDIAN NATIONAL SCIENCE ACADEMY

# International Advisory Editorial Board

**M A Alario-Franco**
Departamento de Química
Inorgánica
Universidad Complutense
28040-Madrid, SPAIN

**B Cantor**
Department of Materials
University of Oxford
Oxford OX1 3PH, UK

**A K Cheetham**
Materials Department
University of California
CA 93106-5130, USA

**L E Cross**
Materials Research Laboratory
The Pennsylvania State University
PA 16802-4800, USA

**P Day**
The Royal Institution of
Great Britain
London W1X 4BS, UK

**J Etourneau**
Institut de chimie de la
matière condensée
de Bordeaux
33608 Pessac cedex, FRANCE

**A H Heuer**
Materials Science and Engineering
Case Western Reserve University
Cleveland, Ohio 44106, USA

**T Inoue**
Dept. of Energy Conversion Science
Kyoto University
Sakyo-ku 606-01, Kyoto
JAPAN

**F A Kuznetsov**
Institute of Inorganic Chemistry
Academy of Sciences
630090 Novosibirsk 90, RUSSIA

**J Livage**
Chimie de la matière condensée
Université Pierre et Marie Curie
Paris 75252, FRANCE

**S Nagakura**
Kanagawa Academy of Science
and Technology
Kawasaki, Kanagawa 213
JAPAN

**A E Owen**
Department of Electrical Engineering
The University of Edinburgh
Edinburgh EH9 3JL
Scotland, UK

**P Rama Rao**
Atomic Energy Regulatory Board
MUMBAI 400 094
INDIA

**A K Ramdas**
Department of Physics
Purdue University
Indiana 47907, USA

**C N R Rao**
J N Centre for Advanced
Scientific Research
Bangalore 560 012, INDIA

**B B Rath**
Naval Research Laboratory
Washington DC 20375-5320
USA

**M Rühle**
Max Planck Institut für Metallforschung
D-70174, Stuttgart
GERMANY

**E C Subbarao**
Tata Research Development
and Design Centre
Pune 411 001, INDIA